This is to certify that the
dissertation entitled

DESIGN AND OPERATION OF PERMANENT
MAGNET MACHINE FOR INTEGRATED STARTER-
GENERATOR APPLICATION IN SERIES HYBRID
BUS

presented by

SINISA JURKOVIC

has been accepted towards fulfillment
of the requirements for the

Doctoral degree in Electrical Engineering

Elias G Strangas
Major Professor's Signature

22 May 2009
Date

DESIGN AND OPERATION OF PERMANENT MAGNET MACHINE FOR INTEGRATED STARTER-GENERATOR APPLICATION IN SERIES HYBRID BUS

By

Sinisa Jurkovic

A DISSERTATION

Submitted to
Michigan State University
in partial fulfillment of the requirements
for the degree of

DOCTOR OF PHILOSOPHY

Electrical Engineering

2009

ABSTRACT

DESIGN AND OPERATION OF PERMANENT MAGNET MACHINE FOR INTEGRATED STARTER GENERATOR APPLICATION IN SERIES HYBRID BUS

By

Sinisa Jurkovic

This work focuses on urban mass transportation vehicle, a hybrid electric bus with series powertrain configuration. With respect to hybrid vehicles, integrated starter/alternator configuration has only been seriously explored in so-called mild hybrid topology, while very little has been published on full hybrids and in particular series hybrid configuration. This work is divided into two parts: The first presents an evaluation and design of PMAC machine candidates suitable for starter-generator application in hybrid bus with series powertrain configuration. PMAC machines with interior and surface mount permanent magnets are considered and compared. Different design aspects such as concentrated versus distributed windings, interior and exterior rotor structures and different permanent magnet materials are evaluated. Different slot per pole per phase configurations for concentrated winding PMAC machines are also examined. Comparison and evaluation of the machines is based on their performance which included evaluation of winding and iron losses, magnet losses and maximum torque capability as well as the size and weight of the machines. A 6kW scaled prototype of the designed machine is built and tested. The second part of this work focuses on the operation and control of PMAC machine for the specified application. Various sensorless control algorithms are considered, as well as control with rotor position feedback with the underlining issue of saturation and

its effects. Finally, in-depth design and analysis of a new control algorithm, which accounts for the entire operating range of PMAC machine, is presented. Analytical, simulation and experimental results of the designed machine and the controller are presented.

To Mirko, Ljubica and Igor Jurkovic with my affection and gratitude

ACKNOWLEDGMENTS

I am deeply indebted, to my advisor Professor Elias Strangas for his guidance, support, and immense patience throughout these years. I am thankful for the privilege to work with him as well as professional and personal example he has set.

I would also like to thank Professors Hassan Khalil, Feng Peng and Ranjan Mukherjee for their time and effort in being members of the Ph.D. committee.

I would like to extend special thanks to those at General Motors Corporation for their support and patience while finishing this dissertation.

Special words of thanks go to my lab colleagues Wes Zanardelli, Carlos Nino, John Kelly, Steve Bohan, Sajjad Zaidi and Tariq Abdul for all of their support.

I would also like to thank the members of the department whose help was much appreciated, including Brian Wright, Roxanne Peacock, Vanessa Mitchner, Meagan Kroll and Pauline Van Dyke.

I owe very special thanks to my friends, Karen, Igor, Pam, Jadranko, Nancy, Marko, Duje and Hrvoje, whose support and encouragement helped make my graduate studies possible and enjoyable.

Finally, I owe special thanks to my parents, Mirko and Ljubica, and my brother, Igor without whose support and encouragement none of this would have been possible.

TABLE OF CONTENTS

LIST OF TABLES

LIST OF FIGURES

CHAPTER 1

Introduction

This chapter will outline the objectives, contributions and organization of this dissertation, provide an introduction into Hybrid Electric Vehicles (HEV) and a literature survey on PMAC Machines for Integrated Starter-Generator (ISG) Application as well as the literature survey on the operation of Surface Permanent Magnet Machines (SPM) under saturation.

1.1 Objectives and Contributions

The goal of this work is to solve a two-fold problem related to Integrated Starter-Generator (ISG) in Series Hybrid-Electric (SHE) Bus, design and analysis and operation and control.

1.1.1 Design and Analysis

The first part deals with analysis, selection and design of the best PMAC machine candidate for this application. The literature survey shows the following shortcomings in the PMAC machine analysis for the given application: Little work has been done on comprehensive comparison of various PMAC machines for ISG applications in Series HE Vehicles. Size and weight comparison is often neglected in the performance assessment even though it is a crucial factor in automotive applications. While ample of literature exists on analysis of PMAC machines, these tools presented are inadequate for concentrated winding topologies. Moreover, SPM Machines are usually not considered for ISG applications, because of their poor performance in constant power region i.e. less speed range than IPMs. In [13]. El-Refaie compared various Slot/Pole/Phase combinations of SPM machines, but not the 1/2 SPP topology. In that work 2/7 SPP machine was selected as the most suitable one because of its extended speed range. In the work presented in this dissertation, the 2/7 SPP machine designed by El-Refaie, is used as a starting benchmark point in designing and selecting the best suited PMAC machine for ISG application in Series HEV. The contributions of this work are:

1. Comprehensive analysis and comparison of Interior Permanent Magnet Machines vs. Surface Permanent Magnet Machines for ISG Application C-4.

2. Analysis and comparison of distributed vs. concentrated windings, as well as the analysis of various Slot/Pole/Phase combinations (including 1/2 SPP topology) with respect to machine size, minimal losses and highest torque capability C-4.

3. Tools for analytical design and performance assessment of SPM Machines with concentrated windings are derived and discussed. In particular, improved models for core and magnet losses of fractional slot SPM machines are derived C-3.

1.1.2 Operation and Control under Saturation

The second part of this work focuses on the operation and control of a PMAC machine for the given application. In particular the issue of control of SPM Machines under saturation is explored. The major contributions are:

1. Nonlinear model and characterization of SPM Machine under saturation C-6.
2. Design, analysis and verification of a general algorithm for the control of SPM machines under saturation C-7.

First a model of a saturated SPM Machine is presented and the detrimental effects of saturation on machine performance are discussed. The High-Gain Nonlinear Observer of the rotor flux is designed for the entire operating range of the machine, including saturation. To verify the performance and effectiveness of the designed observer, two existing control strategies, one utilizing high-freaquency injection method (for startup and low speeds) and the other utilizing back EMF measurement method (for high speed operation) are implemented in combination with the designed observer. Finally simulation and experimental results of the machine performance with the proposed observer are presented.

1.2 Organization of the Dissertation

The balance of this dissertation is divided into the following parts:

- Chapter 1, introduces the concept of Hybrid-Electric Vehicles, various power train configurations and advantages and challenges associated with each. The concept of Integrated Starter-Generator and its advantages and applications as well as the sizing of the generator unit for SHE vehicle are also discussed. Finally an analytical approach for assessment of the required generator size for the SHE vehicle is derived, based on the vehicle size, driving cycle and engine efficiency map.

- Chapter 2 presents an overview of the current PMAC machine technology, from various types of the machines used today, to vector control of the machines to, electromagnetic modeling of PMAC. Various rotor topologies with respect to magnet placement are presented, as well as different stator winding configurations i.e. distributed and concentrated windings.

- Chapter 3 focuses on the development of analytical tools for the design and performance evaluation of Fractional Slot SPM Machines. Analytical calculations of winding resistance and inductance, winding function, magnetic field in the air-gap, permeance function, back EMF waveform, electromagnetic torque and copper, iron and magnet losses are presented.

- Chapter 4 presents Finite Element Analysis of the machines under consideration and comparison with analytical results. Summary of losses, efficiencies and torque-speed curves for these are also presented. Finally maximum torque performance is evaluated of various Slot/Pole/Phase configurations for SPM machines. Experimental testing of 6kW prototype is also included.

- Chapter 5 discusses the state of the art in control of PMAC machines. Both high-frequency injection and back EMF methods are analyzed as well as the issues and challenges associated with them. Specifically, the issue of saturation and its effect on both of the control strategies is addressed.

- Chapter 6 presents an in-depth analysis and a non-linear model of SPM machine under saturation. With the new model in place position-sensorless control of SPM machines is revisited and necessary improvements are discussed to account for saturation induced errors. Finally Finite Element and experimental characterizations of the saturated SPM machine are presented.

- Chapter 7 presents a controller of SPM machines under saturation without rotor position sensors. The analysis presented in Chapter 6 is used to design a new High-Gain Non-linear Observer for the operation of the SPM machine in saturated region. In-depth design and analysis of the observer performance and stability is presented followed by the experimental verification of the results.

- Chapter 8 summarizes the work done in this dissertation along with conclusions and future work suggestions.

1.3 Hybrid Electric Vehicles

Although it has only been seriously discussed in the last decade, the idea of electric vehicles goes back to nineteenth century. With improvements in internal combustion engines performance and efficiency throughout the last century, and more recent improvements in electric motors, battery technology, power electronics and increasing

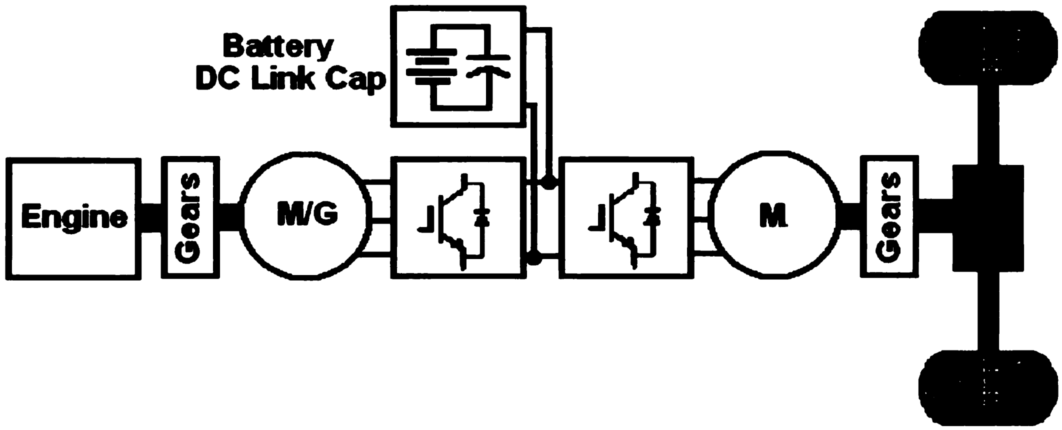

Figure 1.1: Series HE Bus

awareness in ecology and fuel consumption, the idea of combining the two propulsion means appears to be the most reasonable solution. Several variations of the hybrid combinations are available which can all be classified into four categories series, parallel, series-parallel or mild hybrid powertrain, with each configuration having its advantages and disadvantages and best suited applications as described in [1]. In a Series Hybrid System, the engine is not directly linked to the transmission for mechanical driving power. All of the energy produced by the engine is converted to electric power by the generator, which recharges the energy storage device in order to provide power to the electric motor as shown in Figure 1.1

The electric motor system provides torque to run the wheels of the vehicles. Because the combustion engine is not directly connected to the wheels, it can be operated at the optimum rate, and can be automatically turned off for temporary all-electric, zero emission operation. Series hybrids are most suitable for commuting vehicles such a transit bus, which frequently stop and go. In a Series Hybrid Electric Vehicle

(SHEV) system, by adding an electric motor to provide the power during accelerations, the engine can be smaller than that of a conventional vehicles [1]. This work focuses on urban mass transportation vehicles, hybrid electric buses with series powertrain configuration. Heavy duty busses present excellent candidates for hybrid vehicles because of their size, which translates into a capability to store larger batteries and electrical machines required. Compared to passenger cars, busses operate at lower speeds, limited acceleration, and usually less road grades; which all contribute to lower demand on the electrical system. Because of frequent stops a significant amount of energy can be recovered through regenerative breaking.

1.3.1 Integrated Starter/Generator

In the last several years there has been an increasing interest in integrated starter-generator (ISG). Starting rotating machines from a battery source has been increasingly used in a wide range of automotive, household and military applications. Moreover it is particularly attractive in automotive, aircraft and portable generator industries, where volume and weight reduction are major requirements. In mild hybrids the integrated starter/generator machine must be designed to have a wide speed range operation, which is why traditionally this role was reserved for induction or interior PMAC machines, because of their excellent field weakening capabilities. In series hybrid vehicles the generator is designed to operate at one fixed speed and variable torque to optimize the engine efficiency according to the fuel map shown in Figure 1.2.

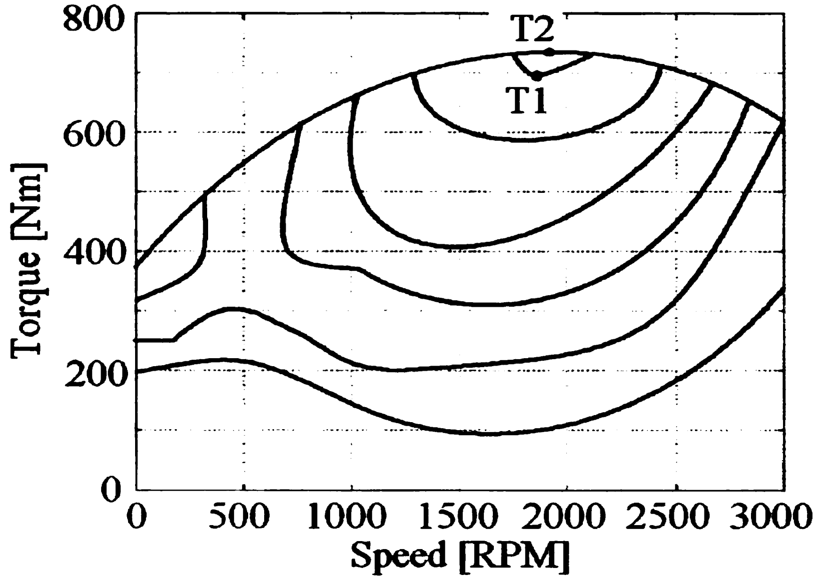

Figure 1.2: 6L Diesel Engine Fuel Map

In addition, to be used as a starter, this machine should be capable of producing high torque at zero and low speeds. It is now apparent that with these new redefined requirements a range of different machines can be considered for this purpose.

1.3.2 Sizing the Generator

Given the series configuration of the HE bus, the sizing of a generator must take into consideration the most efficient conditions of the IC engine, in terms of fuel consumption and emissions, which in practice can be accomplished by keeping the operating speed constant and allowing small torque variations as shown in Figure 1.2.We define two operating modes of the HE bus;

Mode I - Summer Mode i.e. with air conditioning and

Mode II - Winter Mode i.e. without air conditioning.

Instead of having continuous torque variation we will simply assume that the engine will operate at two discrete operating points, T_1 and T_2, shown in Figure 1.2, corresponding to two operating modes I and II respectively. It is obvious that we must size the generator to satisfy the maximum power requirement, which means operation with air conditioning or Mode I. From this point on we can assume that the generated power will be kept constant, independently of the load demand. The most obvious choice of the generator output power in such case would be given by:

$$P_{GEN} = P_{DC} \tag{1.1}$$

where P_{DC} is the instantaneous required power from the DC bus including both power for propulsion motors and auxiliary electrical loads. In this case the average power required for traction and electrical loads will be supplied by the generator, while the transients will be covered by the battery unit. On board battery recharge from the generator is not possible, but rather only energy used for battery charging will come from the regenerative breaking. This approach may cause the battery SOC to fall very low at times, reducing its lifetime dramatically. In order to avoid this problem initial and final SOC during a drive cycle must be taken into account when designing the electric generator of the series HEV. At the very minimum we must ensure that:

$$SOC_{END} \geq SOC_{MIN} \tag{1.2}$$

or for the upper limit of the generator size

$$SOC_{END} = SOC_{START} \tag{1.3}$$

Satisfying this condition will ensure the bus availability for the next trip without necessary stop for "plug in" battery recharge. We can now rewrite the generator power equation (1.1) as:

$$P_{GEN} = P_{DC} + P_{BAT} \tag{1.4}$$

Where the P_{BAT} will ensure recharge of the battery. In the interval when the vehicle operates in fully electric mode, the battery will be the only source of power delivering energy E_{BAT}. During the time when the generator is on, it should deliver energy supplied by the battery and fulfill the requirements of P_{DC}.So we can write the following:

$$E_{GEN}=\begin{cases} E_{BAT} + \int_{t}^{t_1} P_{DC} - P_{GEN}dt \text{ }, P_{DC} > P_{GEN} \\ \\ E_{BAT} \text{ }, P_{DC} < P_{GEN} \end{cases} \tag{1.5}$$

where $t - t_1$ is the time interval the generator is on. So P_{BAT} can be calculated as

$$P_{BAT}=\frac{E_{BAT}}{t - t_1} \tag{1.6}$$

1.4 Survey of PMAC Machines for ISG

With respect to hybrid vehicles, integrated starter-generator configuration has only been seriously explored in so called mild hybrid topology, while little has been published on full hybrids and in particular on series hybrid configuration. Cai in [2] presents a comparison of electrical machines for integrated starter-generator applications in mild hybrids, but quickly excludes the SPM machine because of the wide speed range requirement. Friedrich *et al.* in [3] provided an optimization procedure for the design of PMAC ISA, but only IPM machines are considered, due to excellent field weakening range. Nagorny *et al.* in [4] compared several different rotor structures for a similar application to conclude that the SPM machine was best suited, based on torque and THD analysis, but no results on distributed and concentrated windings comparison are available. Similar studies were carried out by both Salminen in [5] and Cross in [6], with conclusions that less magnetic material is required for the same size SPM machine compared to the IPM but only for distributed winding machines. No results are given for the concentrated windings machine. Moreover these authors have focused on assessing output torque and power capabilities of the machine while ignoring the analysis of losses, size and weight. Cros and Viarouge in [7] presented a study about the use of concentrated windings in a high-performance PM machines. They identified the various slot/pole combinations that can support three-phase concentrated windings. They also presented a systematic method to determine the optimum concentrated winding layout in both cases of regular and irregular slot distribution. They provided guidelines for identifying the slot/pole combinations that can provide high machine performance and analysis results for sample designs using concentrated windings, showing that the performance of these machines is better than that of traditional machines with one slot/pole/phase. There is minimization of both copper volume and Joule losses, reduction in the manufacturing cost and improvement in the output characteristics.

The effect of the winding factor on the Joule losses has been discussed by the same group. A comparison of the Joule losses, cogging torque and axial length of conventional distributed 1 slot/pole/phase winding, single-layer concentrated winding, and double layer concentrated winding has been presented. It was shown that by choosing the appropriate slot/pole combination, concentrated windings have lower Joule losses and cogging torque compared to distributed windings. Also it was shown that the double-layer concentrated windings has the shortest axial length and hence has the greatest potential to be the most compact unit among the three winding configurations under consideration. Ishak, Zhu and Howen in [8], [9] compared the eddy current losses in the magnets for both winding configurations. It was shown that the single-layer winding induces higher eddy current losses in the magnets due to the higher special harmonic content. Libert and Soulard [11] investigated various slot/pole combinations for surface PM machines equipped with concentrated windings. Among the considered factors were the winding factors, MMF harmonic content, torque ripple, and radial magnetic forces that cause vibration and noise. Reichert [12] discussed the advantages and disadvantages of using concentrated windings in large synchronous machines for low speed high torque applications. He indicated that the eddy current losses in the magnets might be a limiting factor for using concentrated windings in high speed applications. In [13] El–Refaie proposed a fractional slot PMAC machine with 2/7 slot/pole/phase (SPP) configuration as the best candidate for this application, however the comparison has not been carried out with respect to 1/2 SPP configuration.

In this work (Chapter 2-4) a 2/7 SPP SPM Machine designed by El–Refaie in [13] is be used as a starting point and the comparison is carried out with a 1/2 SPP machine.

1.5 Operation of SPM Machines Under Saturation

In the last decade, as the efficiency of electric drives has become a more important and desirable characteristic, Permanent Magnet Synchronous Machines (PMSM) are rapidly replacing induction machines. Rotor position information is necessary for Field Oriented Control (FOC) of Permanent Magnet Synchronous Machines (PMSM). It is particularly attractive to obtain the rotor position information without shaft sensors, since they increase the cost of the overall system and degrade the reliability. It is well documented in the literature that the error in the estimate of rotor position increases with the load current [14]. Guglielmi *et al.* showed in [15] that an error exists in rotor position estimation due to cross-magnetic saturation between d- and q-axes. Stumberger *et al.* in [16] evaluated the effect of saturation and cross-magnetization for IPM, but offered no compensation for the error. Li *et al.* in [17] studied modeling of the cross-coupling magnetic saturation in a specific position-sensorless control scheme based on high-frequency signal injection. Zhu *et al.* in [18] proposed a practical approach for mitigating the rotor position error due to saturation in high-frequency injection method. However, operation and flux position detection in SPM machines is affected by magnetic saturation regardless of the control strategy and requires correction at the model level. Harnefors *et al.* in [19] studied a general algorithm for control of AC motors and noted the existence of the error in rotor position estimation due to saturation, but the analysis focused only on the unsaturated case. Moreover the error signal was linearized making their conclusions local only. It will be shown here that although this error may be relatively small, it has a significant detrimental effect on the machine performance.

In this work we will focus on operation of SPM machines under magnetic saturation.

The major contributions of this part are nonlinear model and characterization of SPM machine, and design, analysis and verification of a general algorithm for control of SPMAC machines under saturation.

It will be presented in three sections: the non-linear model and characterization of the SPM machine under saturation, in-depth analysis of the non-linear observer structure adjusted for the presence of saturation without linearizing the error signal and experimental results validating the derived non-linear model of the machine, impact of saturation induced error on machine performance and validation of performance of the proposed observer combined with high frequency injection position-sensorless controller presented by Jang *et al.* in [22]. It is important to note that although the work presented here is focusing on the observer implementation in conjunction with high frequency injection method, it can be used in combination with any control strategy including back EMF methods or methods utilizing position encoder feedback.

CHAPTER 2

Permanent Magnet AC Machines

This chapter presents an overview and introduction into PMAC machines, rotor topologies with respect to magnet placement and configuration and concentrated and distributed winding configurations. The concept of vector modeling and control as well as the electromagnetic model of the PMAC machine are also presented.

2.1 Overview

In the last decade as the efficiency of electric drives has become a more important and desirable characteristic, Permanent Magnet Synchronous Machines (PMSM) are rapidly replacing induction machines. Moreover PMSM offer high power density, so they are more suitable in the applications requiring volume reduction i.e. automotive, aircraft and portable generator industries. A permanent magnet synchronous machine is basically an ordinary AC machine with windings distributed in the stator slots so that the flux created by stator current is approximately sinusoidal. Quite

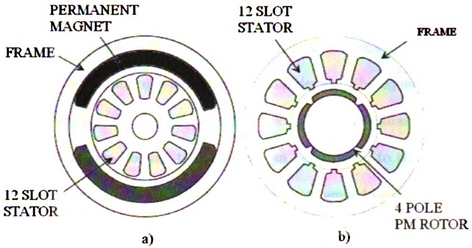

Figure 2.1: PMAC with Exterior and Interior Rotor T.J. Miller [46].

often also machines with windings and magnets creating trapezoidal flux distribution are incorrectly called permanent magnet synchronous machines. A better term is Brushless DC (BLDC) machine, since the operation of such a machine is similar to that of a traditional DC machine with a mechanical commutator, with the exception that the commutation in a BLDC machine is done electronically. The work presented here concentrates on permanent magnet synchronous machines (PMSMs) with a sinusoidal flux distribution. Rotating permanent magnet synchronous machines used today come in two different configuration; interior and exterior rotor as shown in Figure 2.1.

2.2 Permanent Magnet Rotor Topologies

The most commonly used construction for the PM motors has the permanent magnets located on the rotor surface. Herein, this motor type will be called surface magnet motor for simplicity. In a surface magnet motor the magnets are usually magnetized radially. Due to the use of low permeability rare-earth magnets the synchronous inductances in the $d-$ and $q - axes$ may be considered to be equal which can be helpful while designing the surface magnet motor. The construction of the motor is quite cheap and simple, because the magnets can be attached to the rotor surface. The embedded magnet motor has permanent magnets embedded in the deep slots. There are several possible ways to build a surface or an embedded magnet motor as shown in Figure 2.2 from [7], a) surface mounted magnets, b) inset rotor with surface magnets, c) surface magnets with pole shoes producing a cosine flux density, d) buried tangential magnets, e) buried radial magnets, f) buried inclined magnets with cosine shaped pole shoe, and g) permanent magnet assisted synchronous reluctance motor with axially laminated construction. In the case of an embedded magnet motor, the stator synchronous inductance in the $q - axis$ is often greater than the synchronous inductance in the $d - axis$. If the motor has a ferromagnetic shaft a large portion of the permanent magnet produced flux goes through the shaft. In order to increase the linkage flux crossing the air-gap, embedded-magnet motor mat have a non-ferromagnetic shaft.

Another method to increase the flux crossing the air gap is to fit a non-ferromagnetic sleeve between the ferromagnetic shaft and the rotor core [7]. Compared to the embedded magnets, one important advantage of the surface mounted magnets is the smaller amount of magnet material needed in the design (in integer-slot machines).

If the same power is required from the same machine size, the surface mounted magnet machine needs less magnet material than the corresponding machine with

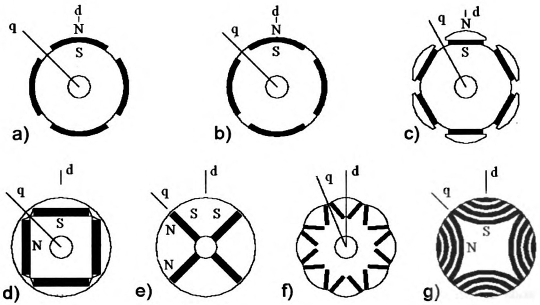

Figure 2.2: Location of the permanent magnets in PMAC, Gieras [7].

embedded magnets. This is due to the two facts: in the embedded-magnets-case there is always a considerable amount of leakage flux in the end regions of the permanent magnets and the armature reaction is also worse than in the surface magnet case. Zhu *et al.* in [26] reported that the embedded magnet structure facilitates extended flux-weakening operation when compared to a surface magnet motor with the same stator design (both machines are equipped with an integer slot winding). They also stated that the iron losses of the embedded magnet machine were higher than that of the machine with surface magnet rotor. However, there are several advantages that favor the use of embedded magnets. Because of the high air-gap flux density, these machine may produce more torque per rotor volume compared to the motor which has surface mounted magnets. This, however, requires usually a larger amount of PM-material. The risk of permanent magnet material demagnetization remains smaller.

The magnets can be rectangular and there are less fixing and bonding problems with the magnets: the magnets are easy to mount into the holes of the rotor and the risk of damaging the magnets is small [46]. Because of the high air-gap flux density an embedded magnet low speed machine may produce a higher efficiency than the similar surface magnet machine.

2.3 Windings

A permanent magnet machine can have a variety of winding structures as shown in Figure 2.3, a) distributed windings, b) single-layer concentrated windings and c) double-layer concentrated windings [13]. Early and large PMAC machines have used sinusoidally distributed windings, while in the last several years, for smaller machines the concentrated winding structure has been increasingly explored due to their short end windings and simple structure suitable for high volume automated manufacturing. They are not yet frequently used in larger electrical machines, where efficiency and smooth torque production are more important. This can change if the traditional drawbacks of the winding type, i.e. high torque ripple and low fundamental winding factor, can be mitigated.

Cros and Viarouge in [7] discovered that this motor type has a higher performance than the motor type with regular distribution of the slots. The copper volume and copper losses in the end windings are reduced. The end windings of a traditionally wound machine need more space (which, again, requires more copper volume and mass), because different phase coils cross each other. In the concentrated fractional

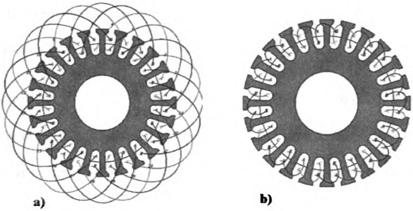

Figure 2.3: Winding layouts: a) Distributed, b) Concentrated

slot wound machine the space needed, in the end turnsregion, for the conductors to travel from one slot to the next one is as small as possible, as the example illustrates in Figure ?? b) where the coil is wound around one tooth. However, the two-layer winding type produces the smallest end windings as it is shown in Figure ?? c. There are several attractive advantages that result from the use of concentrated windings around the teeth:

1. Significant reduction of the copper volume used in the end region, especially in the case of short axial-length machines. This is clear comparing Figures ??, a,b and c [46].

2. Significant reduction in the Joule losses in the end region due to shorter end turns. Murakami *et al.* [27].

3. Improved efficiency compared to the classical distributed winding configuration with one slot per pole per phase [13].

4. Reduction in cost made possible by simplified manufacturing [13].

5. Easier to fabricate compared to the distributed lap winding, particularly when the stator can be segmented into separate stator poles.

6. Significantly higher slot fill factor (up to 78 %) can be achieved, where slot fill factor is defined as the ratio of the copper area to the total area of each slot compared to typical 60% in distributed windings. Murakami *et al.* [27]

7. Concentrated windings can be used in the design of modular PM brushless machines with higher numbers of phases to improve fault tolerance. They also can be used in high-phase-number machines to increase the specific torque [28].

Challenges involved in using concentrated windings are:

1. The spatial MMF distributions in the machine air gap that result from concentrated windings deviate significantly from sinusoidal waveforms, so that d–q transformation loses accuracy.

2. Assumptions needed for classical phasor analysis are not correct.

3. Risks of elevated torque ripple and low winding factors [13].

4. Potential for higher acoustic noise and vibration [13].

2.4 Control of PMAC Machines

In order to be utilized to their highest potential, PMACs have to be controlled by employing field oriented vector control techniques. Since all the control is done in the rotor frame of reference, knowledge of the accurate rotor position is necessary.

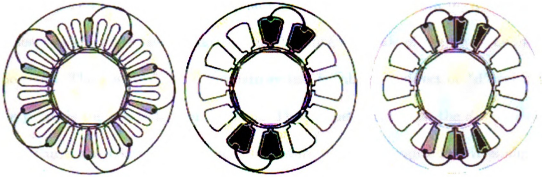

Figure 2.4: End Windings Comparison

Shaft position and speed sensors have been used for decades for this purpose; however their employment drives up the cost of the overall system and significantly degrades the reliability. Considering these disadvantages of position sensors, it is obvious why researchers and application engineers have been focusing their efforts on developing robust position-sensorless drives for PMSM.

2.4.1 Current Vector Control Principle

The earliest vector control principles for AC permanent magnet synchronous machines resembled the control of a fully compensated DC machine. The idea was to control the current of the machine in space quadrature with the magnetic flux created by the permanent magnets. The torque is then directly proportional to the product of the flux linkage created by the magnets and the current. In an AC machine the rotation of the rotor demands that the flux must rotate at a certain frequency. If the current is then controlled in space quadrature with the flux, the current must be an AC current in contrast with the DC current of a DC machine. The mathematical modelling of an AC synchronous machine is most conveniently done using a coordinate system, which rotates synchronously with the magnetic axis of the rotor, i.e. with the rotor. The x-axis of this coordinate system is called the direct or "d" axis and the y-axis is the quadrature or "q" axis. The magnet flux lies on the $d-axis$ and if the current is controlled in space quadrature with the magnet flux it is aligned with the $q-axis$. This gives a commonly used name for this type of the control, "$i_d = 0$" -control. Unfortunately this type of control is not appropriate for all permanent magnet machines. The problem is that the air-gap flux is affected by the flux created by the current and the inductance of the machine. This is called the armature reaction. Moreover, if the magnetic circuit of the machine is not symmetric in the directions of $d-$ and $q-$axes, the difference in reluctances can be utilized in the torque production. If the direct axis current is zero, this reluctance torque is also zero.

Different $d-$ and $q-axis$ inductances are a result of different $d-$ and $q-axis$ flux reluctance. If the magnets are mounted on the rotor surface, both the $d-axis$ and the $q-axis$ fluxes must go through the magnet. The relative permeability of the rare earth permanent magnets is near unity, which means that permanent magnets behave like air in the magnetic circuit. The so called effective air-gap is therefore very large and the inductances due to the large air-gap are quite low and nearly equal in $d-$ and $q-axis$. If the magnets are mounted in slots inside the rotor, the magnet flux paths are quite different. Not all the flux has to go through the magnet and a considerable difference between the $d-axis$ and the $q-axis$ inductances is possible. Since the $q-axis$ flux does not always necessarily go through the magnet, usually the $q-axis$

inductance is bigger than the $d-axis$ inductance. This is different from the separately excited synchronous machine where the $d-axis$ inductance is bigger. The reluctance torque resulting in the inductance difference can and should be utilized in the control. Analytical expressions for current references which maximize the ratio of the torque and the current were first formulated by Jahns *et al.* in [3]. This kind of control is generally called the maximum torque per ampere control or minimum current control. In this work the term current vector control is used for all control methods, which control the torque via controlling the currents. Figure 2.5 presents a principle block diagram of the current vector control of PMSMs. The control system consists of separate controllers for the torque and the current. Measurement or estimation of the rotor angle is needed in the transformation of the $d-$ and $q-axis$ current components into fixed coordinate system.

2.5 PMSM Modeling

2.5.1 Vector Control Model

As described earlier the polyphase PMSM control is rendered equivalent to that of the dc machine, by de-coupling control known as vector control. It is also explained that the performance of the machine can best be understood in *dq* axis frame. It is therefore sensible to control the machine in this reference frame. In this section the model of the PMSM machine for vector control is derived. Since the interest is in

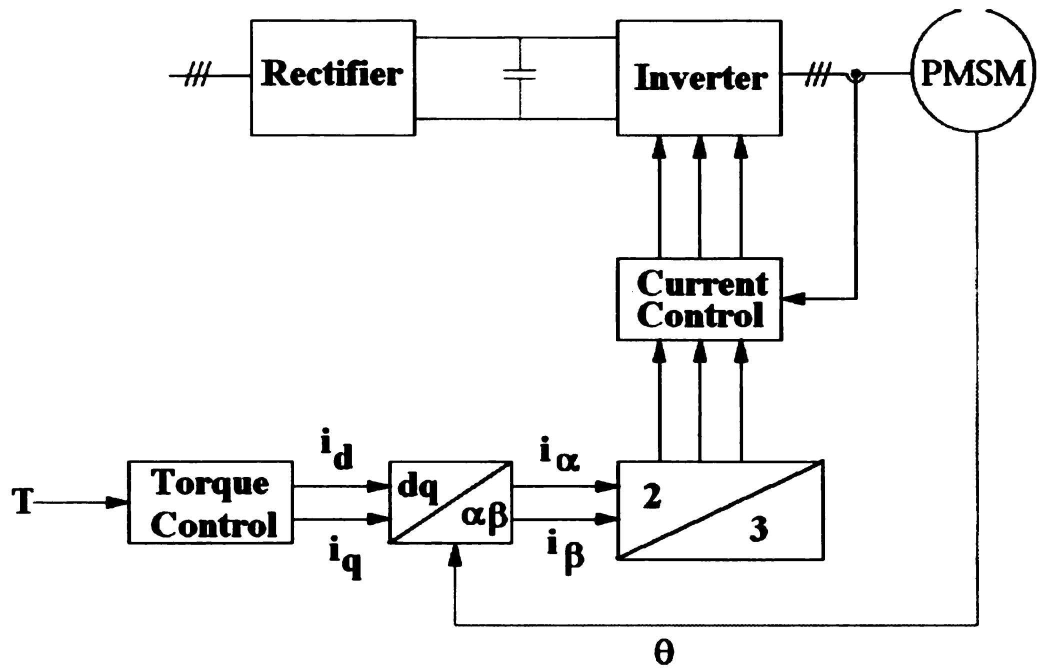

Figure 2.5: A principle block diagram of the current vector control of PMSMs [47]

current control, we consider the three phase current inputs as follows:

$$i_{as} = \hat{i}_s * \sin(\omega_r t + \delta) \tag{2.1}$$

$$i_{bs} = \hat{i}_s * \sin(\omega_r t + \delta - \frac{2\pi}{3}) \tag{2.2}$$

$$i_{cs} = \hat{i}_s * \sin(\omega_r t + \delta + \frac{2\pi}{3}) \tag{2.3}$$

where ω_r is electrical rotor speed and δ is the angle between rotor field and the stator current phasor Figure 2.6, known as the torque angle. The rotor field is traveling at a speed of ω_r ; hence the q and d axes stator currents in the rotor frame of reference

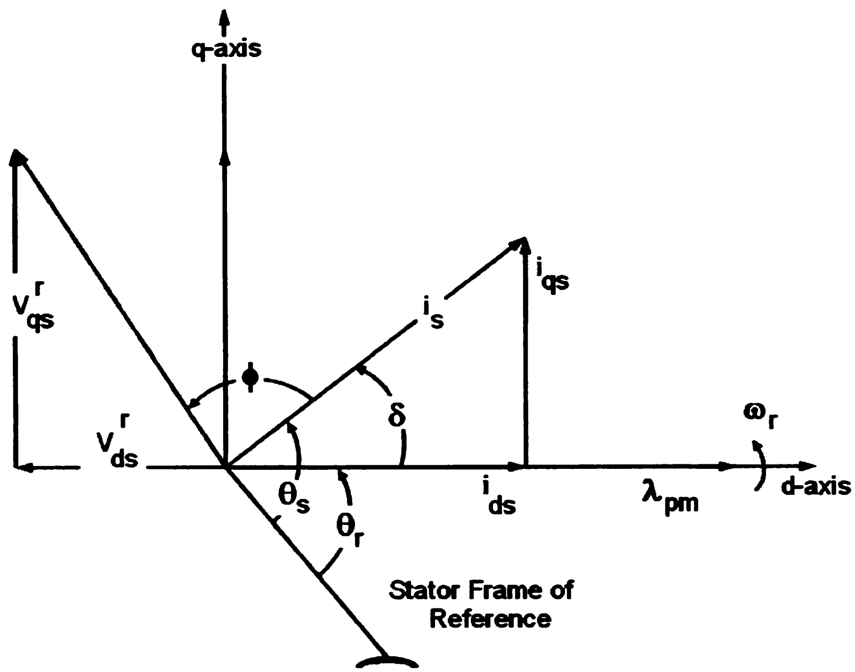

Figure 2.6: Phasor Diagram of PMSM [28]

for a balanced three-phase system are given by:

$$\begin{bmatrix} i_{qs}^{r} \\ i_{ds}^{r} \end{bmatrix} = \begin{bmatrix} \cos\omega_r t & \cos(\omega_r t - \frac{2\pi}{3}) & \cos(\omega_r t + \frac{2\pi}{3}) \\ \sin\omega_r t & \sin(\omega_r t - \frac{2\pi}{3}) & \sin(\omega_r t + \frac{2\pi}{3}) \end{bmatrix} \begin{bmatrix} i_{as} \\ i_{bs} \\ i_{cs} \end{bmatrix} \tag{2.4}$$

by simplifying this equation we get:

$$\begin{bmatrix} i_{qs}^{r} \\ i_{ds}^{r} \end{bmatrix} = i_s \begin{bmatrix} \sin\delta \\ \cos\delta \end{bmatrix} \tag{2.5}$$

In addition one phase voltage of the machine can be written as:

$$v_s = R_s i_s + L\frac{di_s}{dt} \tag{2.6}$$

and by following the same transformations as above we can write the complete PMSM model in the rotor frame of references with following equations:

$$\begin{bmatrix} v_{ds}^r \\ v_{qs}^r \end{bmatrix} = \begin{bmatrix} R_S + L_d p & -\omega_r L_q \\ \omega_r L_d & R_S + L_q p \end{bmatrix} \begin{bmatrix} i_{ds}^r \\ i_{qs}^r \end{bmatrix} + \begin{bmatrix} 0 \\ \omega_r \lambda_{PM} \end{bmatrix} \tag{2.7}$$

Additionally the torque of the PMSM is:

$$Te = \frac{3}{2}\frac{p}{2}\left[\lambda_{PM} * i_{qs}^r + (L_d - L_q) * i_{qs}^r * i_{ds}^r\right]. \tag{2.8}$$

2.5.2 Magnetic Circuit

The analytical calculation of the operation of SPM motor is based on the reluctance circuit analysis shown in Figure ??. The equivalent reluctance circuit of SPM is represented in Figure 2.7.

The stator iron reluctance R_{Fe} consists of the stator teeth R_z and yoke R_s reluctances. Φ_{PM} is the total magnetic flux of the permanent magnets and Φ_σ are additional leakage fluxes in the end regions of the permanent magnets. The air-gap reluctance $R_{\delta 2}$ consists of the air between two magnets and the air-gap reluctance R_δ lies in the minimum air-gap between magnet and stator. The reluctances of the air-gap and permanent magnets are calculated from their region and material char-

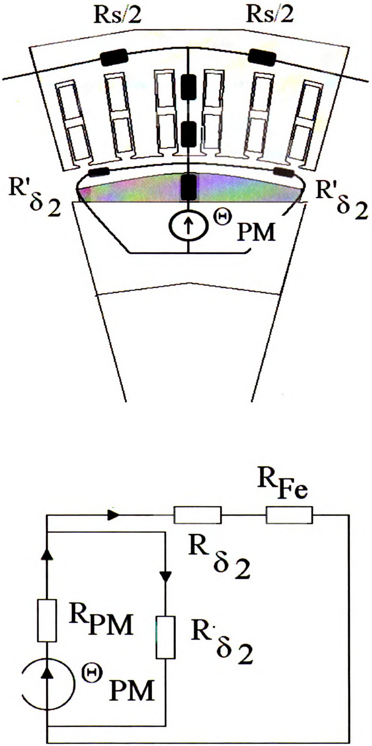

Figure 2.7: Equivalent Circuit of Reluctances in SPM

acteristics.

$$R_\delta = \frac{\delta_o}{\mu_o \tau_p L_i} \tag{2.9}$$

The reluctance of the air-gap between two magnets is:

$$R_{\delta 2} = \frac{l_m}{\mu_o(\tau_p - l_p)L_i} \tag{2.10}$$

Reluctance of the permanent magnets is:

$$R_{PM} = \frac{l_m}{\mu_o \mu_{PM} l_p L} + \frac{l_t}{\mu_o l_p L} \tag{2.11}$$

The iron reluctances in the stator teeth and yoke can then iteratively be calculated. The first evaluation of the air-gap flux can be derived from the equivalent reluctance circuit (Figure 2.7).

$$\Phi_{\delta,PM} = \frac{\Theta_{PM}}{R_{PM} + R_\delta + R_{Fe}(n) + \frac{R_{PM}}{R_{\delta 2}}(R_\delta + R_{Fe}(n))} \tag{2.12}$$

Because of the rectangular air-gap flux density, the flux densities in the stator teeth are constants above the permanent magnets:

$$B_{z1} = \frac{L_i \tau_u}{f_f L_z} \hat{B}_\delta \tag{2.13}$$

and become zero elsewhere. The air-gap flux density B_δ is derived from the air-gap flux and width of permanent magnets l_p as well as from the length L_i.

$$B_\delta = \frac{\Phi_{\delta,PM}}{l_p L_i} \tag{2.14}$$

The peak value of the first harmonic of the air gap flux density can be calculated as coefficients of Fourier series as shown by Gieras [42].

$$\hat{B}_\delta = \frac{4}{\pi} B_\delta \sin\left(\frac{l_p \pi}{2\tau_p}\right) \tag{2.15}$$

so the EMF per phase induced by rotor excitation flux is calculated as

$$\hat{B}_\delta = \frac{4}{\pi} B_\delta \sin\left(\frac{l_p \pi}{2\tau_p}\right) \tag{2.16}$$

$$E_{PM} = 2\pi \frac{f_s \zeta N_{ph} \Phi_{\delta,PM}}{\sqrt{2}} \tag{2.17}$$

where ζ is the winding factor. We can now calculate the direct and quadrature inductances as:

$$L_{q,d} = \frac{m}{2} \frac{8}{\pi^2} \mu_0 \frac{1}{2p} \frac{\tau_p}{\delta_{d,q-eff}} L_i (\zeta N_{ph})^2 \tag{2.18}$$

It is important to note that $\delta_{q-eff} = \delta_{d-eff}$ for SPM and they include the effective air-gap and magnet thickness.

CHAPTER 3

Analysis of Concentrated Winding SPMSM

In this chapter analytical tools for the design and performance assessment of Fractional-Slot PMAC machines are derived. Relevant tools presented in the literature are improved and adapted for use on Fractional Slot/Pole/Phase configurations of SPM machines with outer rotor.

Isahk *et al.* in [9], [10] and [43] worked on analytical prediction of eddy current core rotor and stator losses in PMAC machines. Atallah *et al.* in [29] developed a model for core losses directly related to the machine dimensions and material properties, which makes it suitable for preliminary machine design and efficiency estimation.

The loss model presented in this work is an improved version of that presented in [29], adapted for outer rotor machine configuration that will in addition account for hysteresis losses separately in teeth and back iron for different flux harmonics by taking into the account high-frequency core loss properties of the materials. An adjustment factor for material specific core losses due to PWM switching is also derived.

Losses in the permanent magnets can be significant in SPM machines and need to be accounted for in the machine efficiency estimation. Atallah *et al.* in [29] and later El-Refaie in [13] presented methods for calculating magnet losses in PMAC machines.

However the models described above were developed to include losses caused by the time harmonics of the stator currents and space harmonics of the stator windings. In the case of surface PM with concentrated windings, the stator windings space subharmonics are the dominant factor in inducing eddy-current losses while the losses caused by stator current time harmonics are comparably lower. Hence, the model presented here is adapted for an outer rotor machine and simplified to include only the dominant losses.

Finally an analytical approach for back EMF waveform and electromagnetic torque calculations are presented by taking into account permeance function of the machine.

3.1 Resistance Calculation

El-Refaie in [13] presented methods for calculating the winding resistance and inductance of PMAC machines. The resistance calculation is straightforward except for estimating an average length of the concentrated winding turns. The lengths of the winding end turns vary as the turns move further away from the tooth wall. A model derived in [28] is used, for calculating the resistance of a concentrated winding including the end region. Figure 3.1 shows the layout of one coil in a single-layer

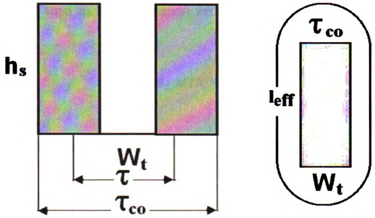

Figure 3.1: Single layer winding and Coil Boundries [13]

winding.The geometric assumptions used in the end-turn length calculation are illustrated in Figure 3.1. In particular, the innermost turn is assumed to have an end turn with straight wires and sharp corners hugging the tooth wall, while the outermost turn is assumed to have a semicircular end turn with width τ_{co}, , defined as follows [13]:

$$\tau_{co} = W_s + \tau_s \tag{3.1}$$

$$W_t = (1 + \lambda_s)\tau_s \tag{3.2}$$

$$\tau_s = \frac{2\pi}{S} R_s = W_s + W_t \tag{3.3}$$

where τ_s, is the slot pitch [m], W_s, is the slot width [m], W_t is the tooth width [m], R_s, is the inner stator radius [m], S is the number of slots and

$$\lambda_s = \frac{Ws}{\tau_s} \tag{3.4}$$

For the inner most turn in the end region we can write:

$$l_{end\_MIN} = Wt \tag{3.5}$$

and for the outermost turn end region:

$$l_{end\_MAX} = \frac{\pi\tau_{co}}{2} \tag{3.6}$$

so that the average end-turn length is:

$$l_{end\_AVG} = \frac{l_{end\_MIN} + l_{end\_MAX}}{2} \tag{3.7}$$

Now we can combine the average length of the end region and effective length to obtain the average length of the turn

$$l_{turn\_AVG} = 2l_{eff} + 2l_{end\_AVG} \tag{3.8}$$

The cross section area of one turn is [13]:

$$A_{turn} = W_s \frac{h_s}{n_{cond}} K_s \tag{3.9}$$

so that the end-turn resistance of one coil is

$$R_{coil} = \frac{\rho_{cu} \cdot l_{turn\_AVG} \cdot n_{cond}}{A_{turn}} \tag{3.10}$$

ρ_{cu} is resistivity of the copper, while R_{coil} is the resistance of one coil. Given the N_c number of turns for series connection of windings the phase resistance expression is:

$$R_{phase} = N_c R_{coil} \tag{3.11}$$

3.2 Inductance Calculation

In this section we will show a general procedure for calculating the mutual and self inductance of any concentrated winding machine by working on an example of the machine with full pitch winding as shown in [45]. The inductance calculation for any fractional slot concentrated winding machine will be identical, by simply substituting in an appropriate winding function. Winding function calculation will be also presented [45].

It will now be assumed that such an MMF distribution exists in the air gap resulting from current i_A flowing in a winding A having N_A turns and winding function $N_A(\phi)$. That is

$$\mathcal{F}_A(\phi) = N_A(\phi) i_A \tag{3.12}$$

This winding is idealized as the dashed concentrated winding in Figure 3.2, but can have any arbitrary distribution [45]. Consider now a second winding, B, having N_B turns arranged along the gap in an arbitrary fashion as shown in Figure 3.2.Again, the rotor is assumed to be stationary, so that it is not necessary at this point to associate winding B with either the stator or rotor. It should be noted that since the reference

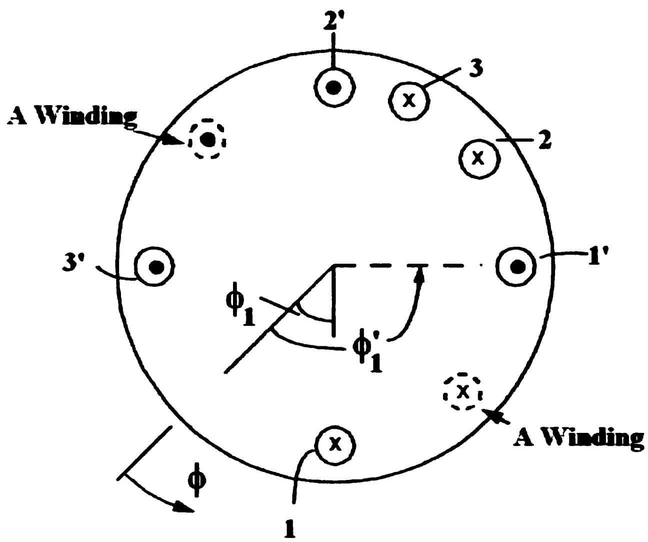

Figure 3.2: Winding placement for mutual inductance calculation [45].

position for the angle ϕ has been previously selected to define $N_A(\phi)$, and one is not free to choose this reference point relative to winding B [45]. It is useful to calculate the flux linking this second winding due to current flowing in the A winding. From elementary magnetic circuits [45], the flux in the gap is related to the MMF by

$$\Phi = \mathcal{F}P \tag{3.13}$$

where P is the permeance of the flux of cross-section A and length l and $\mathcal{F}$ is the MMF drop across the length l. Referring to Figure 3.3, the differential flux across the gap from rotor to stator through a differential volume of length g and cross section $(Rd\phi)$ is

$$d\Phi = \mathcal{F}_A(\phi)\mu_0 Rl\frac{d\phi}{g} \tag{3.14}$$

where $\mathcal{F}_A$ is the MMF due to winding A. The MMF drop (and hence flux) is

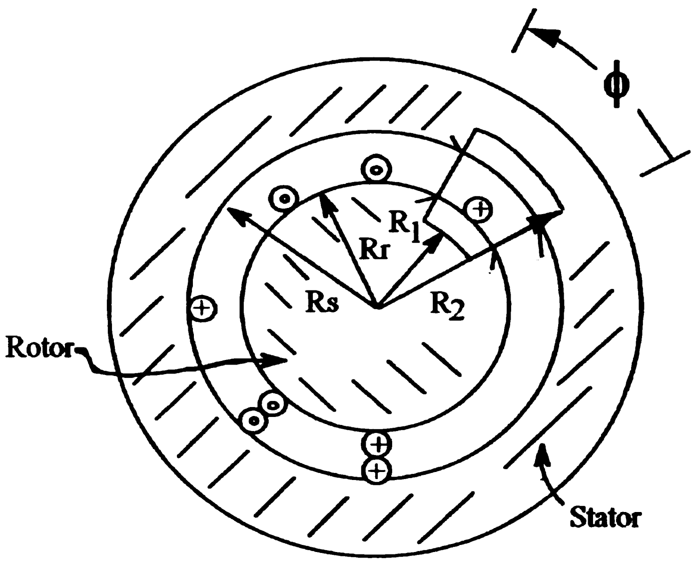

Figure 3.3: Doubly cylindrical device with arbitrary placement of windings [45]

considered positive from rotor to stator.

The total flux linkage of winding B from current in winding A is desired [45]. One can assign the number "1" to the first conductor carrying current into of the page and "$1'$" to the first conductor encountered defined as carrying current out of the page. Similarly, the second conductor encountered with current into the page is labeled as 2 and the second with current the opposite direction as 2'. One can continue with the procedure until all N_B conductors have been accounted for [45]. The last two conductors are "N_B" and "N'_B". In Figure 3.2 the labeling procedure has been carried out for a simple three turn winding, $N_B = 3$. Consider now the flux linking coil $1 - 1'$. If coil side 1 is encountered first around the gap before , then the positive flux linking the one turn coil is [45]:

$$\Phi_{1-1'} = \frac{\mu_0 r l}{g} \int_{\Phi_1}^{\Phi'_1} \mathcal{F}_A(\phi) d\phi \tag{3.15}$$

Alternatively, if coil $1'$ side is situated before 1 then the flux linking the coil is in the negative sense so that

$$\Phi_{1-1'} = -\frac{\mu_0 rl}{g} \int_{\Phi_1}^{\Phi'_1} \mathcal{F}_A(\phi) d\phi \tag{3.16}$$

Either situation can be accounted for if a turns function $n_{B1}(\phi)$ is defined which is zero from $\phi = 0$ until ϕ_1 or whichever comes first. When $\phi = \phi_1$ (or) the turns function then jumps from 0 to 1(or -1) and remains at 1(or -1) until ϕ reaches at which point $n_{B1}(\phi)$ abruptly returns to zero. With this definition of the turns function $n_{B1}(\phi)$, the flux linking turn #1 for either case is

$$\Phi_{1-1'} = \frac{\mu_0 rl}{g} \int_{\Phi_1}^{\Phi'_1} n_{B1}(\phi) \mathcal{F}_A(\phi) d\phi \tag{3.17}$$

Since $n_{B1}(\phi)$ is zero when ϕ takes on value outside the span of the integral, it can also be written:

$$\Phi_{1-1'} = \frac{\mu_0 rl}{g} \int_{0}^{2\pi} n_{B1}(\phi) \mathcal{F}_A(\phi) d\phi \tag{3.18}$$

This process can be continued for all turns. The flux linking the N_B th turn is [45]:

$$\Phi_{N_b-N'_b} = \frac{\mu_0 rl}{g} \int_{0}^{2\pi} n_{N_b}(\phi) \mathcal{F}_A(\phi) d\phi \tag{3.19}$$

The total flux linking the winding is found by summing all N_A fluxes defined as in

[45], or

$$\lambda_{BA} = \sum_{j=1}^{N_A} \Phi_{j-j'} = \frac{\mu_0 r l}{g} \left[\sum_{j=1}^{N_A} \int_0^{2\pi} n_{bj}(\phi) \mathcal{F}_A(\phi) d\phi \right]$$
$$= \frac{\mu_0 r l}{g} \int_0^{2\pi} \left[\sum_{j=1}^{N_A} n_{bj}(\phi) \right] \mathcal{F}_A(\phi) d\phi \quad (3.20)$$

The term in the parenthesis, however, is simply the turns function for the A winding [45]. Defining

$$n_B(\phi) = \sum_{j=1}^{N_A} n_{Bj}(\phi) \quad (3.21)$$

the flux linkage of winding B due to a current winding A becomes

$$\lambda_{BA} = \frac{\mu_0 r l}{g} \int_0^{2\pi} n_B(\phi) \mathcal{F}_A(\phi) d\phi \quad (3.22)$$

The mutual inductance L_{BA} is defined as the flux linkage of winding B divided by the current flowing in winding A so by substituting (3.12) we can write the following

$$L_{BA} = \frac{\lambda_{AB}}{i_B} = \frac{\mu_0 r l}{g} \int_0^{2\pi} n_B(\phi) N_A(\phi) d\phi \quad (3.23)$$

It will be shown in the next section that the turns function can be expressed as [45]:

$$n_B(\phi) = N_B(\phi) + \langle n_B \rangle \quad (3.24)$$

where $n_{B1}(\phi)$ is the winding function for the B winding and $< n_B >$ is the average value of the turns function, so we can rewrite (3.23) as [45]:

$$L_{BA} = \frac{\mu_0 r l}{g} \int_0^{2\pi} N_B(\phi) N_A(\phi) d\phi + \frac{\mu_0 r l}{g} \int_0^{2\pi} \langle n_B \rangle \, N_A(\phi) d\phi \tag{3.25}$$

Since $< n_B >$ is simply a constant, it can be removed from inside the second integral. More over, the winding function $\mathrm{N}_A(\phi)$ is periodic with zero average value, so that the second term is zero. Hence, finally [45]:

$$L_{BA} = \frac{\mu_0 r l}{g} \int_0^{2\pi} N_B(\phi) N_A(\phi) d\phi \tag{3.26}$$

From (3.23) it is clear that reciprocity holds, since the order of the two winding function may be interchanged [45]. Therefore, $L_{AB} = L_{BA}$. Alternatively, if one had started the problem assuming instead an MMF distribution for winding B and calculated the flux linking winding A, the result would have been the same [45]. Equations (3.23) and (3.26) are equivalent expressions for mutual inductance. Although use of (3.26) is generally preferred, (3.23) will be of use when considering the mutual inductance of concentrated windings. Through this analysis, no restrictions were made on winding placement. That is, either winding (or both) can be located on the rotor as well as the stator. Moreover, the results that have been derived are clearly valid for cases where windings A and B are one and the same. Hence, the inductance of winding A associated with flux crossing the air gap (magnetizing inductance) is given by the integral [45]:

$$L_{AA} = \frac{\mu_0 r l}{g} \int_0^{2\pi} N_A^2(\phi) d\phi \tag{3.27}$$

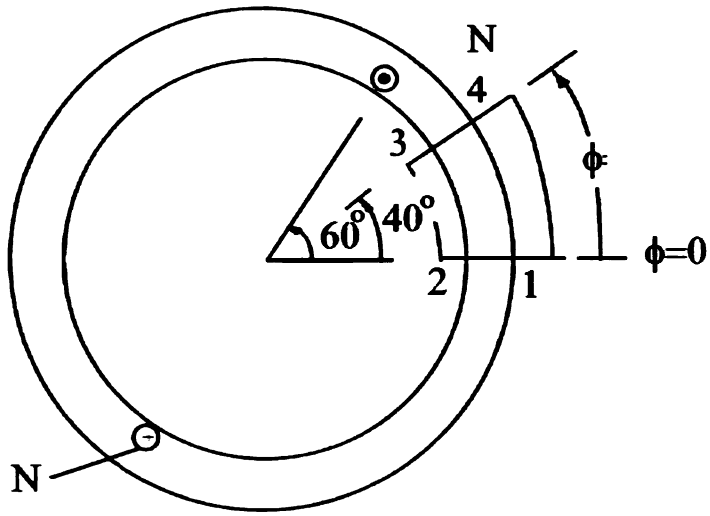

Figure 3.4: Full Pitch Concentrated Winding, Lipo [45]

As a simple introduction to the calculation of winding inductances reconsider the case of the n_t turn concentrated, full pitched winding shown in Figure 3.4 [45].The winding function which has been derived has been plotted in Figure 3.5 for a two pole winding. Since $N_A^2(\phi)$ is simply a constant equal to $N_t^2/4$ integration of (3.27) yields [45]:

$$L_{AA} = \frac{\mu_0 r l}{g} N_t^2 \frac{\pi}{2} \tag{3.28}$$

Following this example and changing the winding pitch and appropriate winding function we can calculate the self and mutual inductance of any concentrated winding machine.

3.3 Winding Function

Consider initially the cylindrical structure of Figure 3.4 [45]. Here, one continuous winding with n_t turns is assumed to be concentrated at two points within the machine as shown. It can be noted that the positive coil side is placed diametrically opposite to the negative coil side. Such a winding spanning π radians is called a full pitch winding [45]. The reference position for the angle ϕ is arbitrarily chosen in the horizontal direction. Visualize a line integral $1-2-3-4-1$ crossing the air gap from stator to rotor at the reference point then crossing back over from rotor to stator at an arbitrary angle measured counter-clockwise from the reference position [45]. A typical line integral is shown in Figure 3.4 where $\phi = 40°$. It should be noted that the line integral $1-2-3-4-1$ is taken in the clockwise direction [45]. The number of turns enclosed by the line integral for the case illustrated is clearly zero. When $\phi = 60°$ the line integral encloses n_t turns [45]. Since the line integral is taken in the clockwise direction, by the right hand rule, positive current enclosed by the path are directed into the page. However, since the winding current has been defined as out of the page, the number of turns enclosed is negative and the turns function $n(\phi)$ abruptly jumps from zero to $-n_t$ at $\phi = 60°$. The function remains at n_t until ϕ reaches 240° at which point n_t positive turns are enclosed so that the function jumps back to zero [45].The resulting function is plotted in Figure 3.5. Since $n(\phi)$ is non-zero only over the range $\pi/3 < \phi < 4\pi/3$, the average value of $n(\phi)$ is

$$\langle n \rangle = \frac{1}{2\pi} \int_{\pi/3}^{4\pi/3} (-N_t) d\phi = \frac{N_t}{2} \tag{3.29}$$

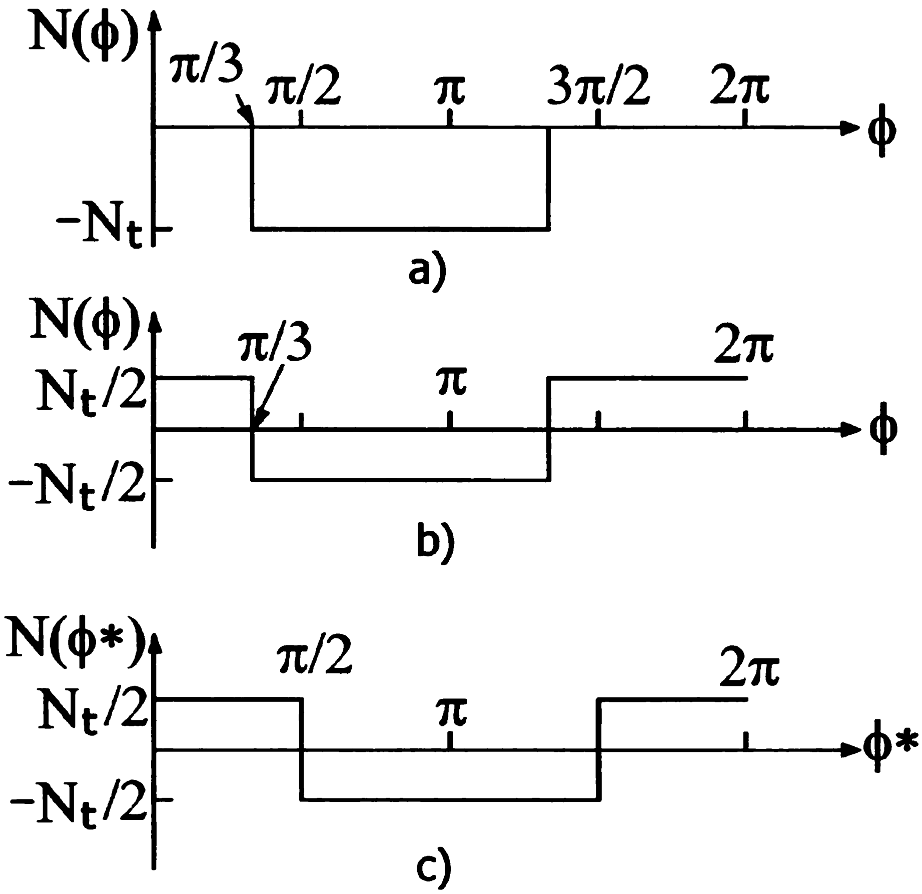

Figure 3.5: Turn and winding functions for an Nt-turn, full pitch coil. [45]

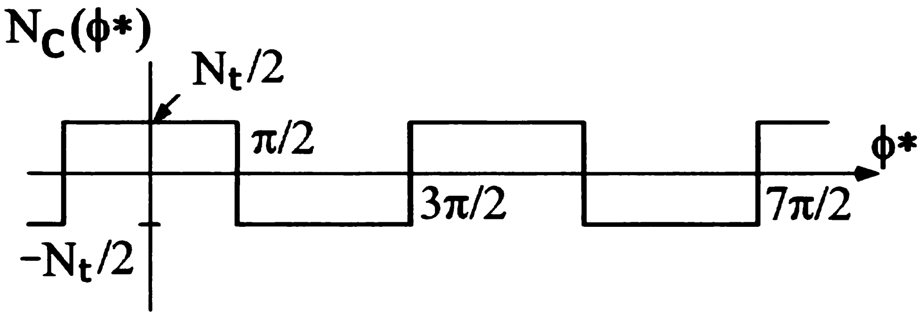

Figure 3.6: Cosine symmetric winding function $N_c(\phi^*)$. [45]

From (3.12) the winding function is simply the turns function $n(\phi)$ translated by $n_t/2$. The function has even symmetry if ϕ^* is chosen such that [45] $\phi^* = \phi + \pi/6$. The unsifted and shifted winding functions are plotted in Figures 3.5(b) and (c). In the case of the shifted winding function, the subscript "c" has been appended since this function for the case of n_t turns concentrated in a single slot has a special significance. In order to help facilitate analysis it is useful to express $N_c(\phi^*)$ in terms of its Fourier components [45]. It is clear that the winding function is completely defined over the entire stator periphery when ranges from 0 to 2π. However, it is possible to consider the function to be repeated when ϕ^* ranges over the value 2π to 4π, 4π to 6π, etc [45]. Specifically, it is useful to assume $N_c(\phi^*)$ as the periodic function shown in Figure 3.6. This function can then be described by a Fourier Series and the resulting series is commonly termed the winding series. It can be noted that since the function of Figure 3.6 has the desired even symmetry about $\phi^* = 0$, that is $N(\phi^*) = N(-\phi^*)$ and hence the winding series for this function will contain only cosine terms [45]. The winding series for an n_t turn, concentrated coil is [45]:

$$N_c = \frac{2N_t}{\pi}\left[\cos\phi^* - \frac{1}{3}\cos 3\phi^* + \frac{1}{5}\cos 5\phi^* ...\right] \tag{3.30}$$

Because the factor $n_t/2$ appears continuously as the amplitude for the winding function of a two-pole winding, the coefficient of (3.30) is sometimes written

$$\frac{2N_t}{\pi} = \frac{4N_p}{\pi} \tag{3.31}$$

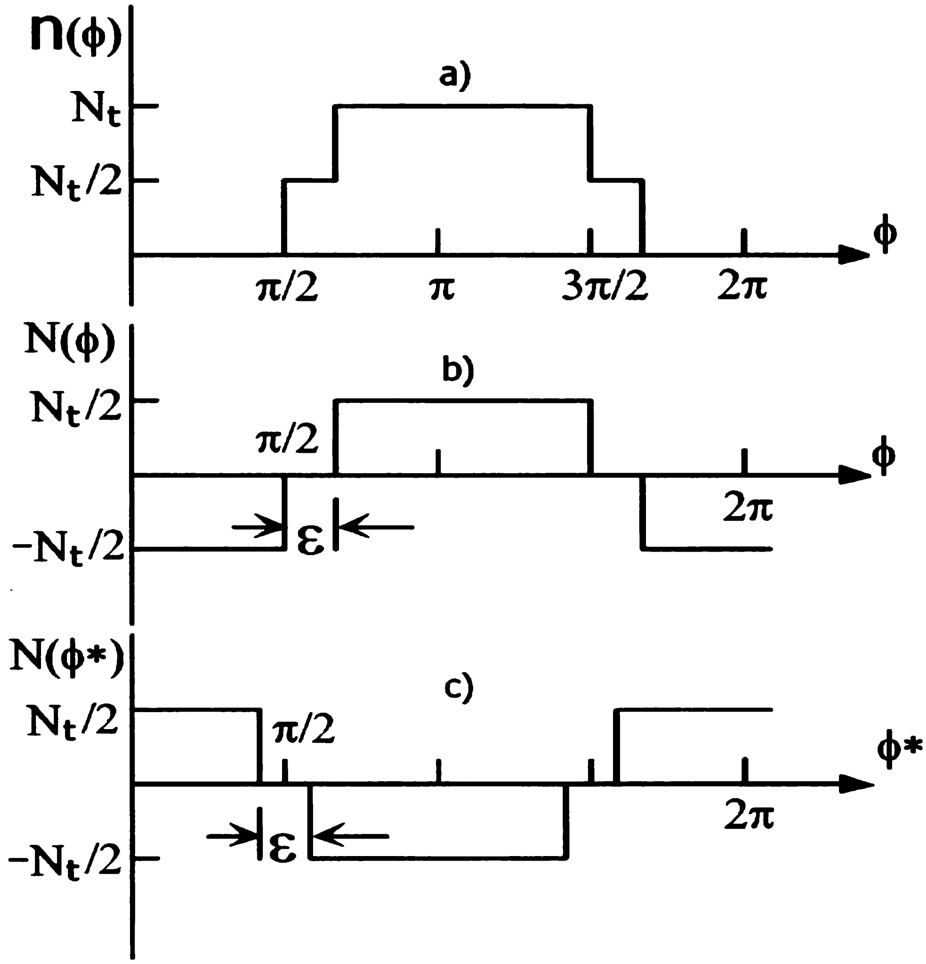

Figure 3.7: Turns and winding functions for a fractional winding, Lipo [45]

where $N_p = n_t/2$ is the number of series connected turns per pole. (For this example the winding only has two poles [45]).

We will now calculate the winding function of a fractional pitch concentrated winding machine by considering it to be a special case of the full pitch concentrated winding machine. The two winding sections are separated by an angle ε.Such a winding is fractional pitch winding [45]. If the reference position is located midway between windings, the resulting function $n(\phi)$ is shown in Figure 3.7(a) [45]. In this case the average value $< n >$ of $n(\phi)$ is $n_t/2$. The function $N(\phi^*)$ is obtained by shifting $N(\phi)$ by $\pi+\varepsilon/2$ radians, that is $\phi^* = (\phi - \pi) - \varepsilon/2$. Figure 3.7(b) and (c) show winding functions for $N(\phi)$ and $N(\phi^*)$ for this case [45]. The Fourier components for this winding distribution are of considerable interest [45]. Again:

$$N(\phi^*) = -N(\phi^* + \pi) \tag{3.32}$$

and since

$$N(\phi^*) = N(-\phi^*) \tag{3.33}$$

the Fourier expansion again contains only odd cosine terms. The h harmonic component can be expressed as the integral [45]:

$$N_h = \frac{2}{\pi}\frac{N_t}{2}\int_{-\pi/2-\varepsilon/2}^{\pi/2-\varepsilon/2} \cos h\phi d\phi \tag{3.34}$$

so that

$$N_c(\phi^*) = \frac{2N_t}{\pi}\left[\cos\frac{\varepsilon}{2}\cos\phi^* - \frac{1}{3}\cos\frac{3\varepsilon}{2}\cos 3\phi^* + \frac{1}{5}\cos\frac{5\varepsilon}{2}\cos 5\phi^* ...\right] \tag{3.35}$$

It is useful to express N_h in terms of the corresponding harmonic coefficients for a concentrated winding. That is

$$N_h = k_h N_{ch} \tag{3.36}$$

The factors k_h are termed the harmonic winding factors and are a means of relating the harmonic components of a winding of arbitrary distribution to a common reference. For the winding under consideration

$$k_h = \frac{(-1)^{\frac{h-1}{2}} \left(\frac{2N_t}{h\pi}\right) \cos\frac{h\varepsilon}{2}}{(-1)^{\frac{h-1}{2}} \left(\frac{2N_t}{h\pi}\right)} \tag{3.37}$$

or simply

$$k_h = \cos\frac{h\varepsilon}{2} \tag{3.38}$$

It is evident that by the symmetry of the winding placement, all even harmonics have been eliminated. Moreover, if ε is properly selected, then one additional odd harmonic can be eliminated. For example, for $\varepsilon = \pi/3$, then

$$k_3 = \cos\left(\frac{3\pi}{3 \cdot 2}\right) \Rightarrow k_3 = 0 \tag{3.39}$$

Similarly it can be shown that for $\varepsilon = \frac{\pi}{5}$, then $k_5 = 0$ etc [45].

It can be shown that two odd harmonics can be eliminated with three $n_t/3$ turn coils displaced by unequal values of $\varepsilon_1$and ε_2. However, since the spacing between windings is uniform, such an arrangement is generally impractical. Another possibility is to utilize unequal spaced slots but vary the number of turns per coil [45]. However, since the number of turns per coil is discrete and space in the slot is limited, specific harmonics can generally be minimized only, but not eliminated. In the case just considered the concentrated winding has been divided into two equal sections. In general, when the winding is separated into k sections (or coils) then $k-1$ odd harmonics can be limited [45].

3.4 Magnetic Field in the Air-Gap

The magnetic flux density in the air gap is obtained by calculating the magnetic potential distribution in the air gap governed by the Laplacian equation and subject by appropriate boundary conditions as shown in [9], [25] and it is given by

$$B_r(\theta, r) = \sum_{n=1,3,5...}^{\infty} K_B(n) f_{Br}(r) \cos(np\theta) \tag{3.40}$$

$$B_l(\theta, r) = \sum_{n=1,3,5...}^{\infty} K_B(n) f_{B\theta}(r) \sin(np\theta) \tag{3.41}$$

$B_r(\theta, r)$ is the radial component of the magnetic field.

$B_l(\theta, r)$ is the tangential component of the magnetic field.

r is the radius [m].

θ is the angular position with reference to the center of a magnet pole.

p is the number of pole pairs.

$$K_B = \frac{-\mu_0 M_n np}{\mu_r (np)^2 - 1} \left\{ \frac{(A_{3n} - 1)\left(\frac{R_m}{R_r}\right)^{2np} + 2\left(\frac{R_m}{R_r}\right)^{np-1} - (A_{3n} + 1)}{\frac{\mu_r + 1}{\mu_r}\left[1 - \left(\frac{R_s}{R_r}\right)^{2np}\right] - \frac{\mu_r - 1}{\mu_r}\left[\left(\frac{R_s}{R_m}\right)^{2np} - \left(\frac{R_m}{R_r}\right)^{2np}\right]} \right\} \tag{3.42}$$

$$f_{Br}(r) = \left(\frac{r}{R_m}\right)^{np-1} + \left(\frac{R_s}{R_m}\right)^{np-1}\left(\frac{R_s}{r}\right)^{np+1} \tag{3.43}$$

$$f_{B\theta}(r) = -\left(\frac{r}{R_m}\right)^{np-1} + \left(\frac{R_s}{R_m}\right)^{np-1}\left(\frac{R_s}{r}\right)^{np+1} \tag{3.44}$$

and

$$A_{3n} = \left(np - \frac{1}{np}\right)\frac{M_{rn}}{M_n} + \frac{1}{np} \tag{3.45}$$

This expression assumes the following:

- Slotless machine - However in order to account for slotting the expression will be multiplied by the relative permeance function, which will be derived in the next section
- External rotor machine $R_m < R_s < R_r$
- Magnets are with parallel magnetization

3.5 Permeance Function

Relative permeance function accounts for the slotting affects in electrical machines. Slotting affects the magnetic field in two ways: First, it reduces the total flux per pole, and this effect is accounted for by introducing the Carter coefficient K_c. Second, it affects the distribution of the magnetic flux in both the air gap and the magnets. Both effects are incorporated into the field calculations using conformal transformations as in [25]. The function is rewritten here for convenience, the details of calculating it are presented in the Appendix I as well as the MATLAB code.

$$\tilde{\lambda}(\alpha, r) = \sum_{\mu=0}^{\infty} \tilde{\lambda}_{\mu}(r) \cos \mu S(\alpha + \alpha_{sa}) \tag{3.46}$$

where α_{sa} is determined by the winding pitch and $\tilde{\lambda}_0$ is average value of permeance given by

$$\tilde{\lambda}_0(r) = \frac{1}{K_c}\left(1 - 1.6\beta\frac{b_o}{\tau_s}\right) \tag{3.47}$$

$$\tilde{\lambda}_\mu(r) = -\beta(r)\frac{4}{\pi\mu}\left[0.5 + \frac{\left(\frac{\mu b_o}{\tau_s}\right)^2}{0.78125 - 2\left(\frac{\mu b_o}{\tau_s}\right)^2}\right]\sin\left(1.6\pi\mu\frac{b_o}{\tau_s}\right) \tag{3.48}$$

b_o is slot width and β is given by

$$\beta(r) = \frac{1}{2}\left[1 - \frac{1}{\sqrt{1 + \left(\frac{b_o}{2(g + h_m)}\right)^2 (1+\nu)^2}}\right] \tag{3.49}$$

g is gap, $g' = g + h_m$

h_m is the magnet thickness and ν is dimensionless calculated using nonlinear solver from:

$$y\frac{\pi}{b_o} = \frac{1}{2}\ln\left[\frac{\sqrt{a^2+\nu^2}+\nu}{\sqrt{a^2+\nu^2}-\nu}\right] + \frac{2g'}{b_o}\tan^{-1}\left[\frac{2g'\nu}{b_o\sqrt{a^2+\nu^2}}\right] \tag{3.50}$$

$$a^2 = 1 + \left(\frac{2g'}{b_o}\right)^2 \tag{3.51}$$

and

$$y = R_s + g' - r \tag{3.52}$$

This permeance function is adjusted for external rotor configuration as well. For internal rotor the y function would need to be adjusted as shown in Appendix I.

3.6 Back EMF Waveform

The back-emf waveform can be calculated by first calculating the flux density distribution in the air gap produced by the magnets including the impact of the stator slots.

$$B_{oc}(\theta, r) = \tilde{\lambda}(\alpha, r) B_{magnet}(\theta, r) = \tilde{\lambda}(\alpha, r) \sum_{h} B_h \cos(hp\theta) \tag{3.53}$$

$$\theta = \alpha - \alpha_{ma} \tag{3.54}$$

where

θ is the angular position with respect to the axis of the magnet

α is the angular position measured from the axis of phase A

α_{ma} is the angle between the axis of phase A and the permanent magnet axis

B_{magnet} is the air-gap magnet field assuming a smooth stator bore calculated in previous section

$\tilde{\lambda}(\alpha, r)$ is permeance function accounting for the slots of the machine.

The special case of a slotless machine will be considered first. The permeance function $\tilde{\lambda}(\alpha, r)$ is simply unity, leading to:

$$B_{oc}(\theta, r) = B_{magnet}(\theta, r) = \sum_{h} B_n \cos(np\theta) \tag{3.55}$$

The flux density distribution at the stator bore is used to determine the back EMF, so that

$$B_{oc}(\theta) = B_{magnet}(\theta, r)\,\big|_{r=R_s} \tag{3.56}$$

$$\alpha_{ma} = \omega_r t + \theta_0 \tag{3.57}$$

where ω_r is the angular frequency and θ_0, is an initial angle. When the machine stator is slotted, the average value of the relative permeance function $\tilde{\lambda}_0$ can be used to account for the reduction of the effective flux density. This leads to an expression for the flux density along the stator bore:

$$B_{oc}(\alpha, t) = \tilde{\lambda}_0 \sum_h B_h \cos(hp(\alpha - \alpha_{ma})) \tag{3.58}$$

The flux linking a stator coil is next calculated as:

$$\psi = \int_{-\alpha_y/2}^{\alpha_y/2} B_{oc}(\alpha, t) R_s l_{eff} d\alpha \tag{3.59}$$

α_y is the winding pitch angle and leff is the length of the stator. Combining the expression in (3.58) and (3.59) leads to:

$$\begin{aligned}
\psi &= \tilde{\lambda}_0 \sum_h B_h R_s l_{eff} \int_{-\alpha_y/2}^{\alpha_y/2} \cos(hp(\alpha - \alpha_{ma})) d\alpha && (3.60) \\
&= \tilde{\lambda}_0 \sum_h 2 B_h R_s l_{eff} \int_0^{\alpha_y/2} \cos(hp\alpha) \cos(hp\alpha_{ma}) d\alpha && (3.61) \\
&= \tilde{\lambda}_0 \sum_h \frac{2 B_h R_s l_{eff}}{hp} \sin(hp\frac{\alpha_y}{2}) \cos(hp\alpha_{ma}) && (3.62)
\end{aligned}$$

The back EMF, e, induced in each turn of a coil is simply then calculated by taking the derivative of the flux linkage, which leads to:

$$e = -\frac{d\psi}{dt} = \tilde{\lambda}_0 \sum_h 2B_h R_s l_{eff} \sin(hp\frac{\alpha_y}{2})\omega_r \sin(hp\alpha_{ma}) \tag{3.63}$$

In the next sections, the various types of losses in the machine will be calculated in order to be able to calculate the machine saliency and output (shaft) power. The main types of losses are the copper losses in the windings, core losses (in the stator teeth and stator back iron), losses in the retaining sleeve (if one is used) and losses in the magnets.

3.7 Electromagnetic Torque Calculation

Torque of a PMAC machine can be calculated in various ways. In the Chapter 2, equation (4.1) was presented, based on the vector model of SPMSM in the rotor frame of reference, however this equation is not particularly useful in the early motor design stage. There are several more appropriate ways to calculate the torque in this case. The electromagnetic force exerted on a non-magnetic conducting region can be calculated using the Lorenz expression

$$\vec{T} = \int\int\int_V \vec{r} \times \left(\vec{J} \times \vec{B}\right) dV \tag{3.64}$$

While this expression is very suitable in finite element analysis, it is not convenient for analytical calculations. Another approach is to calculate the total field in the air gap and then integrate the Maxwell's stress tensor to calculate the tangential force exerted on the rotor. If saturation is neglected, the field in the air gap can be calculated by adding the field solutions due to currents flowing in each individual conducting region, while assuming that the currents in other regions are equal to zero. If permanent magnets are present, their contribution to the overall field is calculated with the currents in all conducting regions equal to zero. The permanent magnet field in the air gap of a surface PM motor has been calculated analytically in previous section of this Chapter. The field solution due to currents flowing in the armature winding needs to be found next. One approach to the calculation of the armature winding field found in literature [9] and [25] is to solve the Laplacian equation in the air gap for a distributed current sheet on the stator surface. The current sheet is distributed so that the current density is uniform along an arc whose length is equal to the size of the slot opening b_o. This field solution is then multiplied by the relative air gap permeance to take into account the presence of slots. The alternative is based on finding the field solution of current in a slot by means of conformal transformation. The field solutions for all the slots are then added to obtain the total armature winding field. Both of these methods are well documented and calculations are omitted here, however the solution of the Laplacian equation representing stator current sheet is provided in later section of this chapter.

The third method, used in this work, of calculating torque analytically is based on the back EMF waveform.

$$T_{em} = \frac{1}{\omega_r}\left[e_a i_a + e_b i_b + e_c i_c\right] \tag{3.65}$$

$e_a e_b e_c$ are back EMF waveforms while $i_a i_b i_c$ are phase current waveforms and ω_r is rotor mechanical speed. Back EMF for the machine was discussed in the previous section, so it becomes relatively simple to calculate the torque as a function of speed.

3.8 Winding Losses

Knowing both the phase current and the phase hot resistance, the machine copper losses can be calculated as:

$$P_{cu} = 3(I_{ph\_RMS})^2 R_{ph\_hot} \tag{3.66}$$

$$R_{ph\_hot} = R_{ph\_hot}(1 + \alpha_{cu}(T_{hot} - T_o)) \tag{3.67}$$

where α_{cu} is copper temperature coefficient, T_{hot} is machine winding hot operating temperature and T_o is the room temperature.

3.9 Iron Losses

The time variation of the flux density in the stator teeth and yoke of PM motors is generally not sinusoidal. Therefore, the approach to core loss calculations based on the assumption that only fundamental component of the flux density exists is not valid [13]. For good estimation of core losses the effects of the harmonics have to be taken into account. Some authors came up with analytical models while others relied on FEA for calculating the core losses. Isahk *et al.* in [9], [10] and [43] worked on analytical prediction of eddy current core rotor and stator losses in PMAC machines. Atallah *et al.* in [29] developed a model for core losses directly related to the machine dimensions and material properties, which makes it suitable for preliminary machine design and efficiency estimation.

The loss model presented here is an improved version of that presented in [29], adapted for outer rotor machine configuration that will in addition account for hysteresis losses separately in teeth and back iron for different flux harmonics by taking into the account high-frequency core loss properties of the materials. Adjustment factor for material specific core losses due to PWM switching is also derived. Total iron losses can be calculated as follow:

$$P_{iron} = (P_{et} + P_{ht})V_t + (P_{ey} + P_{hy})V_y \tag{3.68}$$

P_{et} is the stator tooth eddy-current power loss per unit volume,

P_{ey} is the stator yoke eddy-current power loss,

P_{ht} is the stator tooth hysteresis power loss per unit volume [w/m3]

P_{hy} is the stator yoke hysteresis power loss per unit volume [w/m3]

Eddy-Current Loss Model

Tooth Eddy-Current Loss Model The stator tooth eddy-current losses/unit volume can be calculated using the following equation:

$$P_{et} = \frac{4m}{\pi^2} q \cdot k_q \cdot k_l \cdot k_e \cdot (\omega_e B_{th})^2 \tag{3.69}$$

$$B_{th} = \frac{W_t + W_s}{W_t} \hat{B}_g \tag{3.70}$$

$$\hat{B}_g = \frac{V_{ag\_RMS} \cdot p}{\sqrt{2} \cdot R_s \cdot l_{eff} \cdot N_{phase} \cdot K_{w1} \cdot \omega_e} \hat{B}_g \tag{3.71}$$

m is the number of phases,

k_e is the eddy current constant (depends on the lamination material),

k_q is the motor geometry correction factor (depends on the motor geometry), Details of how to determine its value can be found in [9],

k_l is the correction factor to account for the contribution of the longitudinal (circumferential) component. Details of how to determine its value can be found in [9],

ω_e is the electrical angular velocity [rad/s],

q is the number of slots/pole/phase,

W_t is the tooth width [m],

W_s is the slot width [m],

N_{phase} is the number of series turns/phase,

K_{w1} is the synchronous winding factor,

B_{th} is the peak magnetic flux density in the tooth [T] and

$\hat{B}_g$ is the peak air gap magnetic flux density [T].

Yoke Eddy-Current Loss Model The stator yoke eddy-current losses/unit volume can be calculated using the following equation:

$$P_{ey} = \frac{8}{\alpha \pi^2} k_r \cdot k_e \cdot (\omega_e B_y)^2 \tag{3.72}$$

$$B_y = \frac{W_m}{2d_y}\hat{B}_g \tag{3.73}$$

$$\alpha = \frac{\frac{W_m}{2\pi R_s}\hat{B}_g}{2p} \tag{3.74}$$

$$kr = 1 + \frac{8k_q d_y}{27\alpha q \lambda_2^2} \tag{3.75}$$

where

B_y is the peak magnetic flux density in the stator yoke [T],

d_y is the stator yoke thickness [m],

W_m is the magnet width [m],

λ_2 is the projected slot pitch at the middle of the yoke [m].

Hysteresis Loss Model

The stator tooth and yoke hysteresis losses/unit volume can be calculated using the following equations:

$$P_{ht} = k_h \cdot \omega_e (B_{th})^{\beta} \tag{3.76}$$

$$P_{hy} = k_h \cdot \omega_e (B_y)^{\beta} \tag{3.77}$$

where

P_{ht} is the stator tooth hysteresis power loss per unit volume [w/m3]

P_{hy} is the stator yoke hysteresis power loss per unit volume [w/m3]

k_h is the hysteresis loss constant (depends on the lamination material)

β is the Steinmetz constant (depends on the lamination material)

The basic procedure for the extraction of the core loss coefficients given by Hen-

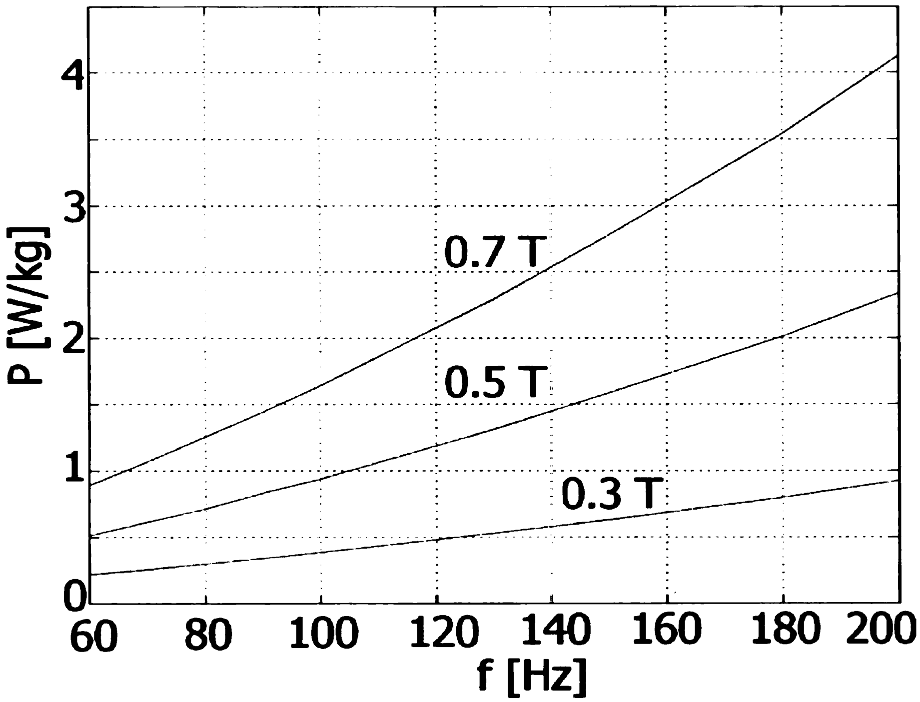

Figure 3.8: Core losses for U.S. Steel M36, 29 Gauge [48]

dershot and Miller [46] will be explained on an example of U.S. Steel M36, 29 Gauge steel lamination. The manufacturer provides information about core losses measured with sinusoidal fields at different frequencies and flux densities.Figure 3.8 shows the core losses for three values of the flux density, i.e. 0.3 T, 0.5 T and 0.7 T, with the frequency ranging from 60 Hz to 200 Hz. In the case of sinusoidal fields the flux density is given by [48]:

$$B = B_m \sin(2\pi f t) \tag{3.78}$$

The RMS of its derivative value is given by:

$$\left(\frac{dB}{dt}\right) = \frac{2\pi f}{\sqrt{2}} B_m \tag{3.79}$$

substituting (3.79) into the expression for core losses yields the following

$$P_c = k_h f B_m^{\alpha(B_m)} + k_e f^2 B_m^2 \tag{3.80}$$

If we rewrite $\alpha(B_m)$ as

$$\alpha(B_m) = a_h + b_h B_m \tag{3.81}$$

the expression for core losses becomes

$$P_c = k_h f B_m^{a_h + b_h B_m} + k_e f^2 B_m^2 \tag{3.82}$$

dividing equation (3.82) by f we obtain the following expression

$$\frac{P_c}{f} = k_h B_m^{a_h + b_h B_m} + k_e f B_m^2 \tag{3.83}$$

The data in Figure 3.9 is then used to plot $\frac{P_c}{f}$ for all values of B_m.Since the resulting graphs are linear they can be expressed as

$$\frac{P_c}{f} = D + Ef \tag{3.84}$$

The coefficients D and E can be determined for each line using linear regression. The equations (3.83) and (3.84) can now be combined to determine the unknown coefficients [48]. So that:

$$D = k_h B_m^{a_h + b_h B_m} \tag{3.85}$$

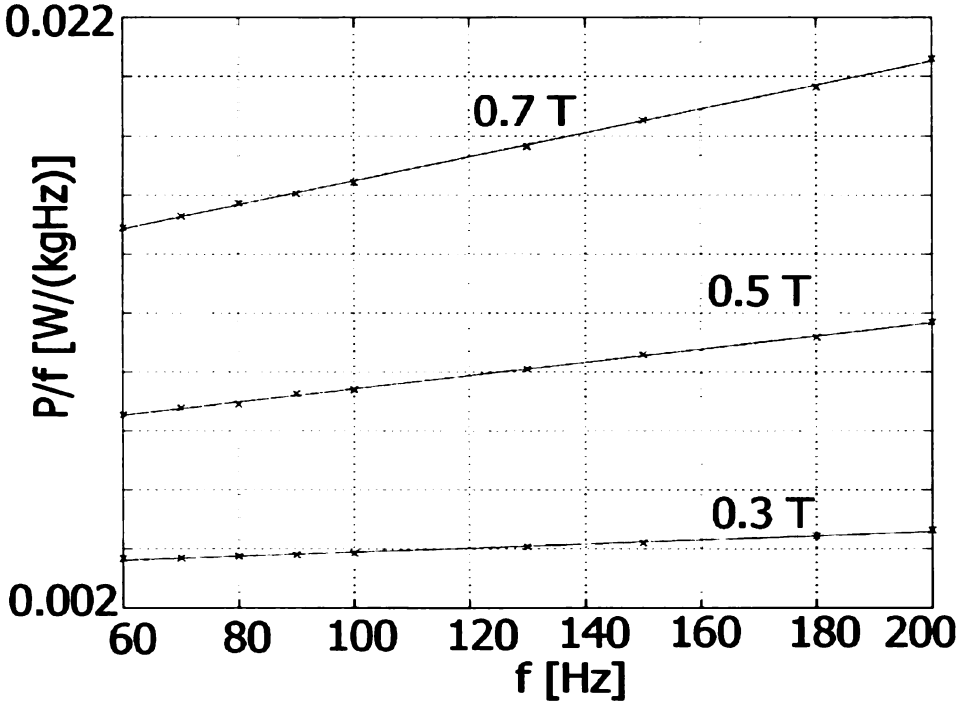

Figure 3.9: U.S. Steel M36 [48],

and

$$E = k_e B_m^2 \tag{3.86}$$

The three values of k_e can be determined from (3.86) and the value used in calculation is simply an average of the three values calculated here [48].

$$k_e = \frac{1}{3}\left(\frac{E_1}{B_{m1}^2} + \frac{E_2}{B_{m2}^2} + \frac{E_3}{B_{m3}^2}\right) \Rightarrow k_e = 8.3 \cdot 10^{-5} \frac{W}{kgHz^2T^2} \tag{3.87}$$

The calculations of k_h, α_h and b_h is also straightforward, although somewhat more tedious. A system of three linear equations, formed by substituting D_1, D_2 and D_3 obtained from the three values of B_m into logarithm of equation (3.85), is to be solved;

$$\begin{bmatrix} 1 & \ln B_{m1} & B_{bm1}\ln B_{m1} \\ 1 & \ln B_{m2} & B_{bm2}\ln B_{m2} \\ 1 & \ln B_{m3} & B_{bm2}\ln B_{m2} \end{bmatrix} \begin{bmatrix} \ln k_h \\ \alpha_h \\ b_h \end{bmatrix} = \begin{bmatrix} D_1 \\ D_2 \\ D_3 \end{bmatrix} \tag{3.88}$$

The system is solved for $\ln k_h, \alpha_h$ and b_h. The k_h is then obtained as:

$$k_h = e^{\ln k_h} \tag{3.89}$$

with the following values obtained for this particular example

$$k_h = 0.023$$

$$\alpha_h = 1.582$$

$$b_h = 0.147$$

3.10 Specific Iron Loss under PWM Supply

PMAC machines are considered in this work are supplied by the 3-phase PWM Inverter. It is well documented in the literature that the inverter switching increases the iron losses in the machine. In [49] an experimental study of the specific iron losses on lamination materials was carried out and it was determined that the losses in laminations are affected by PWM supply and modulation index as shown in Figure (3.10). From the same figure it can also e seen that the iron losses are not impacted by the switching frequency, so for the purpose of this analysis, switching frequency will not be considered. In this section, a method for correcting a specific iron loss

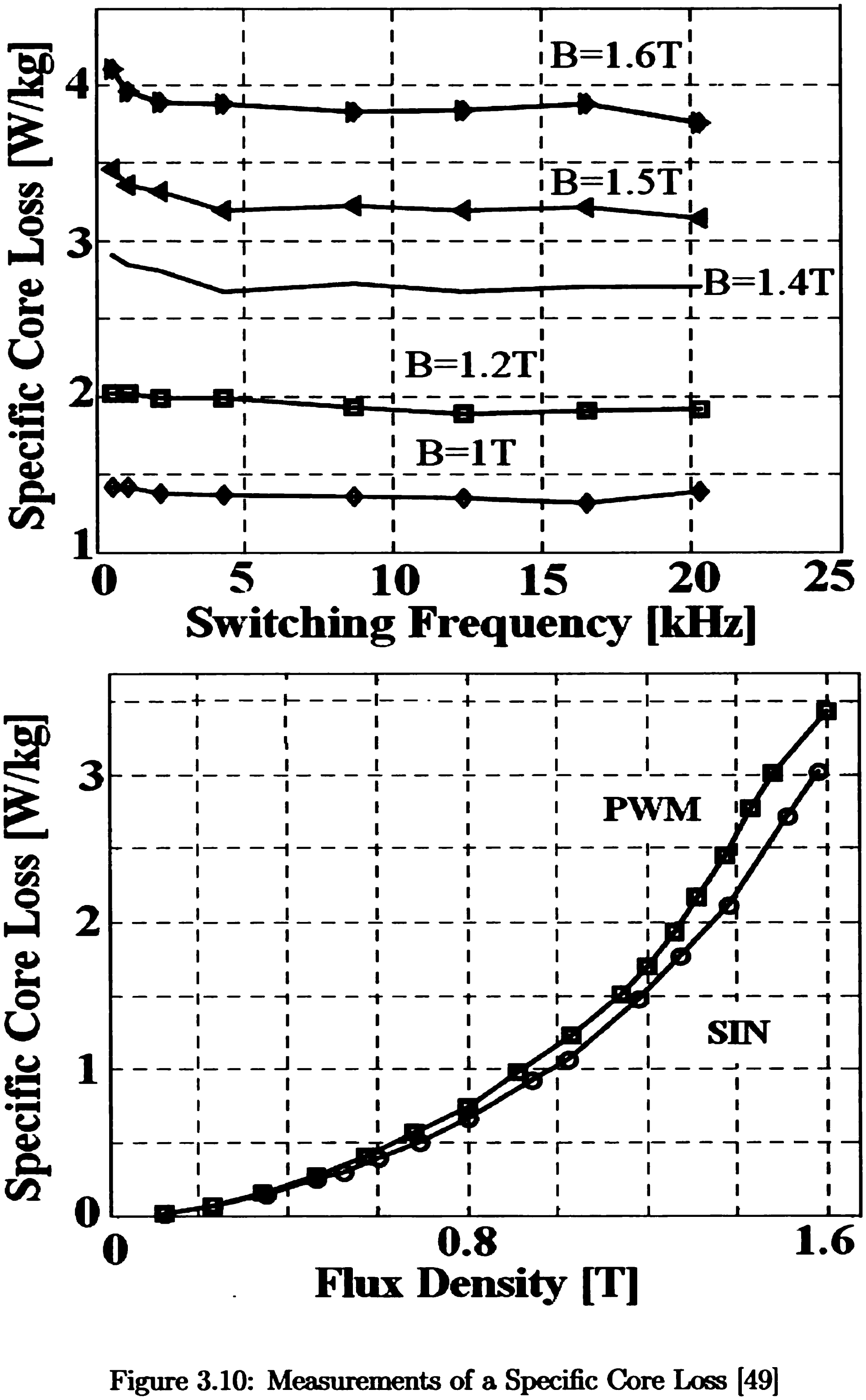

Figure 3.10: Measurements of a Specific Core Loss [49]

of a material under PWM excitation is presented and applied to SPM machines core loss calculation. An assumption is made that the PWM switching will only influence the eddy-current induced losses. Consider the equation for eddy current losses as described by Boglietti in [44]:

$$P_{eddy} = 2\pi K_e f \int_0^T \left(\frac{dB}{dt}\right)^2 dt \tag{3.90}$$

For non sinusoidal voltage, ignoring winding losses, voltage can be expressed as:

$$v(t) = NS\frac{dB}{dt} \tag{3.91}$$

where N is the turn number, S is the section of magnet core. The relationship between the B_m and the voltage can be expressed as in [44]:

$$\int_0^T v(t)dt = 4NSB_m \tag{3.92}$$

combining with the equation (3.91) we can rewrite the eddy loss equation (3.90) as:

$$P_{eddy\_PWM} = 2\pi\frac{K_e}{(NS)^2}v_{rms}^2 \tag{3.93}$$

When the supply voltage is PWM, for Sine-Triangle PWM, the ratio between harmonic voltage v_g and fundamental voltage $v$can be written as [44]:

$$\frac{v_g}{v} = \frac{4J_h(\frac{\alpha n\pi}{2})}{n\pi\alpha} \tag{3.94}$$

where:

$$g = nN \pm h \tag{3.95}$$

$$n = 1, 3, 5...\ h = 3(2m-1) \pm 1,\ m = 1, 2, 3... \tag{3.96}$$

$$n = 2, 4, 6...\ h = \begin{cases} 6m+1, & m = 0, 1, ... \\ 6m-1, & m = 1, 2, ... \end{cases} \tag{3.97}$$

where

$$J_h(x) = \sum_{m=0}^{\infty} (-1)^m \frac{1}{m!\Gamma(h+m+1)} \left(\frac{x}{2}\right)^{h+2m} \tag{3.98}$$

is Bessel function, α is the modulation index, N is the ratio between carrier frequency and modulation frequency. The ratio of voltage rms value between SPWM supply and the fundamental sinusoidal voltage is [44]:

$$\frac{v_{rms\_pwm}}{v_{\sin}} = J_h(x) = \sqrt{1 + \sum_{nM \pm h} \left[4J_h \frac{\frac{n\pi\alpha}{2}}{n\pi\alpha} \right]^2} \tag{3.99}$$

If N is high, the ratio of voltage means value between SPWM supply and sinusoidal supply can be considered equal to one. However at low modulation index values an adjustment is needed to account for the increase in the losses due to switching. Neglecting the increment of the excess loss under SPWM conditions, the eddy component of the magnetic losses of electric magnetic material with SPWM supply can be calculated as [44]:

$$P_{eddy\_PWM} = P_{eddy\_SIN} + \kappa P_{eddy\_SIN} \tag{3.100}$$

Modulation Index	Correction Factor
0.1	0.9756
0.2	0.9053
0.3	0.7975
0.4	0.6645
0.5	0.5209
0.6	0.3807
0.7	0.2562
0.8	0.1564
0.9	0.0878

Table 3.1: Modulation Index and Correction Factor

where κ is the adjustment factor defined as:

$$\kappa = \sum_{nM \pm h} \left[4J_h \frac{\frac{n\pi\alpha}{2}}{n\pi\alpha} \right]^2 \tag{3.101}$$

The numerical relationship of κ and the modulation index α is shown in the Table 3.1.

3.11 Magnet Losses

Several authors have addressed the issue of eddy-current losses in the magnets in case of surface and interior PM machines. There are three main sources of the eddy-current losses induced in the magnets. These are the stator winding space harmonics, the stator current time harmonics, and the space harmonics due to slotting effects. In surface PM machines, it can be assumed that the losses due to slotting effects can be neglected due to the large effective air gap. In general magnet losses in ferrates and bonded magnets are much lower compared to sintered magnets since they have

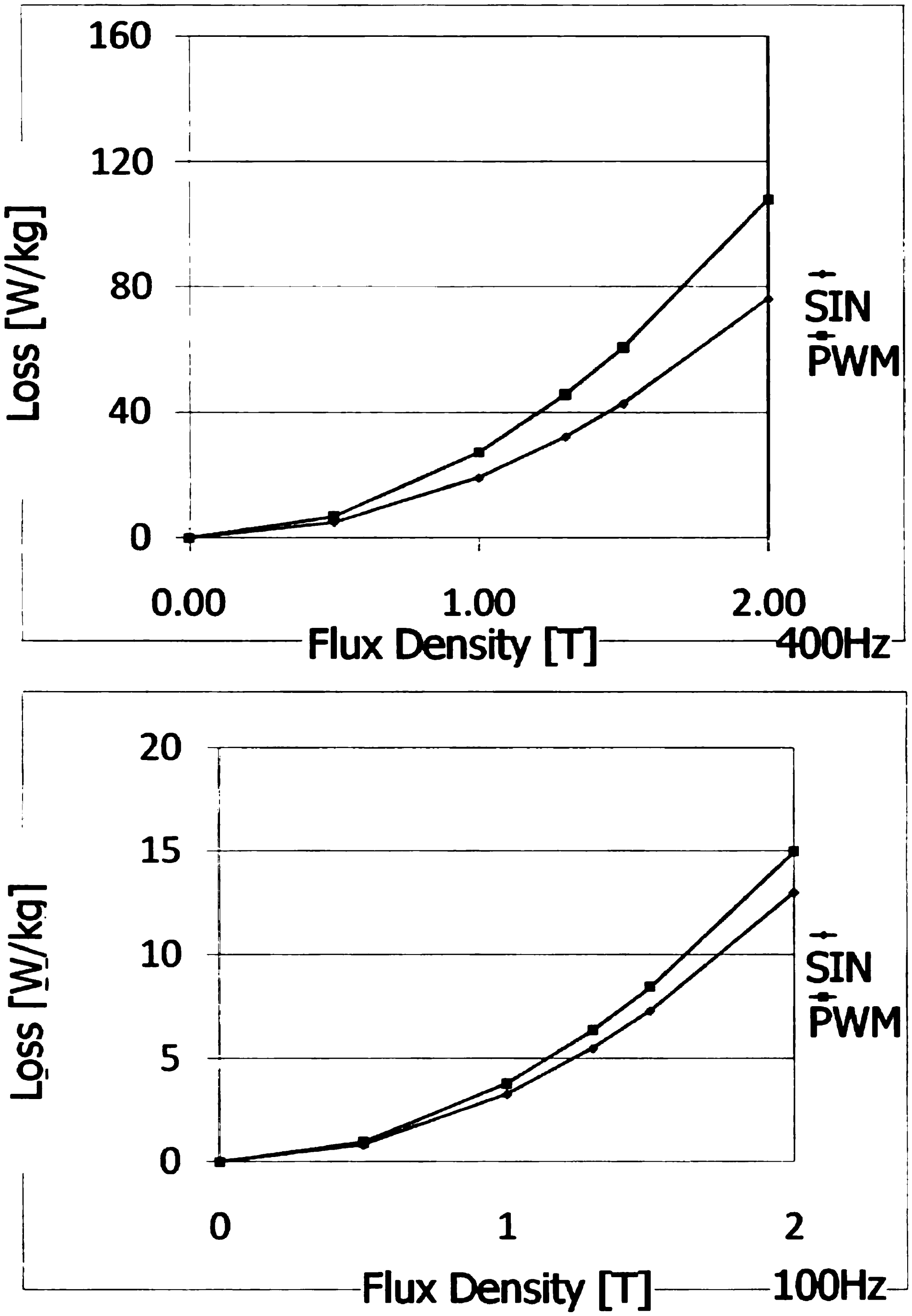

Figure 3.11: Specific Core Loss of M19 Steel Modulation Index = 0.3

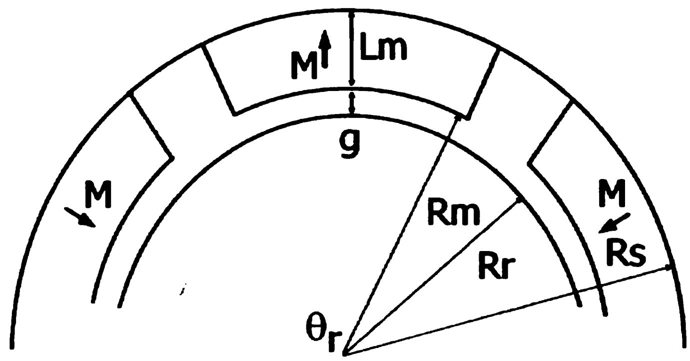

Figure 3.12: Outer Rotor SPM Machine

high resistivity.Atallah *et al.* in [29] and later El-Refaie in [13] presented methods for calculating magnet losses in PMAC machines. However the models described above were developed to include losses caused by the time harmonics of the stator currents and space harmonics of the stator windings. In Surface PM Machines with concentrated windings the stator windings space sub-harmonics are the dominant ones in inducing eddy-current losses. The basic assumptions in this model are:

- The current flow in the stator windings can be approximated by an equivalent current sheet.
- The stator and rotor iron cores have infinite permeability and zero conductivity.
- The eddy currents which induce losses in the magnets are flowing in the axial direction only.
- The magnet material is homogeneous and isotropic.
- The eddy currents are only resistance-limited.

The stator winding can be represented with the following equivalent current sheet

$$J_S(\theta_S, t) = \begin{cases} +\frac{m}{2}\sum J_n \cos(np_s\theta_S - p_r\omega_r t), n = mk + c \\ \\ -\frac{m}{2}\sum J_n \cos(np_s\theta_S + p_r\omega_r t), n = mk - c \\ \\ 0, n \neq mk \pm c \end{cases} \tag{3.102}$$

In the rotor frame of reference the current sheet can be rewritten as following:

$$J_S(\theta_S, t) = \begin{cases} +\frac{m}{2}\sum J_n \cos(np_s\theta_r - (np_s - p_r)\omega_r t), \\ n = mk + c \\ \\ -\frac{m}{2}\sum J_n \cos(np_s\theta_S + (np_s + p_r)\omega_r t), \\ n = mk + c \\ \\ 0, n \neq mk \pm c \end{cases} \tag{3.103}$$

where $c = \pm 1$, and J_n is defined as:

$$J_n = \left(2N_{phase}\left(\frac{I_m}{\pi R_s}\right)\right) K_{wn} \tag{3.104}$$

with the following definitions:

J_s is the equivalent current sheet

J_m is the induced eddy-current density in the PM

n is the spacial harmonic order

p_s is the fundamental stator winding pole pairs

p_r is the fundamental rotor winding pole pairs

ω_r is the rotor angular velocity

N is the number of phases

N_{phnse} is the number of series turns/phase

I_m is the peak phase current

θ_S, is the angle along the stator

$\theta_{r,}$. is the angle along the rotor

The induced eddy-current loss in one magnet segment can be derived as follows:

$$P_m = \frac{\omega_r}{2\pi} \int_{o}^{2\pi/\omega_r} \int_{R_n}^{R_r} \int_{-\alpha_m/2}^{\alpha_m/2} \rho_m J_m^2 r d_r d\theta_r dt \tag{3.105}$$

or

$$P_m = \sum_{n=1}^{\infty} (P_{cn} + P_{an}) \tag{3.106}$$

P_{cn} and P_{an} are defined in equations (3.107) (3.109).

$$P_{cn} = \frac{m^2 \mu_o^2 \alpha_m J_n^2}{8 \rho_m n^2 p_s^2} (np_s \pm p_r) 2\omega_r^2 * \frac{\left[\begin{array}{c} \left(\frac{R_s}{R_m}\right)^{2np_s} R_s^2 R_m^2 F_n + \\ \\ \left(\frac{R_s}{R_r}\right)^{2np_s} \frac{R_s^2 R_s^2}{(2np_s + 2)} * \left(1 - \left(\frac{R_m}{R_r}\right)^{2np_s+2}\right) \\ \\ + \left(\frac{R_s}{R_r}\right)^{2np_s} R_s^2 (R_r^2 - R_m^2) \end{array} \right]}{\left[1 - \left(\frac{R_s}{R_r}\right)^{2np_s}\right]^2} \tag{3.107}$$

Where

$$F_n = \begin{cases} \dfrac{\left(\dfrac{R_r}{R_m}\right)^{-2np_s+2} - 1}{(-2np_s + 2)}, np_s \neq 1 \\ \\ \ln\left(\dfrac{R_r}{R_m}\right), np_s = 1 \end{cases} \tag{3.108}$$

And

$$P_{an} = \frac{m^2 \mu_o^2 J_n^2}{\alpha_m \rho_m n^4 p_s^4}(np_s \pm p_r) 2\omega_r^2 *$$

$$\left[\begin{array}{c} \left(\frac{R_s}{R_m}\right)^{2np_s} R_s^2 R_m^2 G_n + \\ \\ \left(\frac{R_s}{R_r}\right)^{2np_s} \frac{R_s^2 R_s^2}{(2np_s+2)} * \left(1 - \left(\frac{R_m}{R_r}\right)^{2np_s+2}\right) \end{array} \right]^2 *$$

$$\left[\frac{\sin^2\left(np_s \frac{\alpha_m}{2}\right)}{(R_r^2 - R_m^2)\left(1 - \left(\frac{R_s}{R_r}\right)^{2np_s}\right)^2} \right] \tag{3.109}$$

$$G_n = \begin{cases} \dfrac{\left(\frac{R_r}{R_m}\right)^{-np_s+2} - 1}{(-np_s+2)}, np_s \neq 2 \\ \\ \ln\left(\frac{R_r}{R_m}\right), np_s = 2 \end{cases} \tag{3.110}$$

Analytical results for the two machine candidates SPP=1/2 and SPP=2/7 are presented in Chapter 4. It is worth noting that no detailed analysis has been carried out to determine accurate expressions for friction and windage losses but instead formulas provided by Gieras are used

$$P_{fr} = k_{fb} m_r n_r 10^{-3} \tag{3.111}$$

where k_{fb} is an empirical coefficient ranging from 1 to 3, m_r is the mass of the rotor and n_r is the rotor speed in RPM. The windage losses for the speeds below 6000 RPM can be approximated using

$$P_w = 2l_a D_{ro}^3 n_r^3 10^{-6} \tag{3.112}$$

where D_{ro} is the outer diameter of the rotor l_a is the core length.

CHAPTER 4

Finite Element Analysis

This Chapter presents evaluation of the PMAC machines for the ISG application. Interior and Surface PM machines are examined with the concentrated and distributed winding configurations. In [13] El–Refaie proposed a fractional slot PMAC machine with 2/7 slot/pole/phase (SPP) configuration as the best candidate for this application, however the comparison has not been carried out with respect to 1/2 SPP configuration.

In this work the 2/7 SPP SPM Machine designed by El–Refaie in [13] is used as a starting point and the comparison is carried out with a 1/2 SPP machine for the given application. Finite Element Analysis of the machines under consideration and comparison with analytical results is included. Summary of losses, efficiencies and torque-speed curves for machines under consideration are also presented. Finally maximum torque performance is evaluated of various Slot/Pole/Phase configurations for SPM machines. Experimental testing of a prototype scaled to 6kW is also included.

4.1 Comparison of Machine Candidates

In this section we present the results of FE simulation for the two machine candidates. The finite element analysis program used in the computations is Cedrat's Flux2D version 10.1. It computes for plane sections (problems in the plane or problems with rotational symmetry) the magnetic, electric or thermal states of devices. These states allow computation of several quantities: fields, potential, flux, energy, force etc. The quantities obtained would be difficult to define by other methods (analytical computations, prototypes, tests, measurements). In the case of a fractional slot machine the flux in the air-gap is difficult to estimate by any analytical method, but may be easily solved with finite element analysis, FEA. The accuracy of the FEA depends on the geometry, the quality of the FE-mesh and also on the time-step values.

4.1.1 Rotor Topology Selection

The first step is to compare the Surface Permanent Magnet and Interior Permanent Magnet Machines. Towards that end we examined two different rotor topologies, shown in Figure (4.1), to determine the machine best suited to meet our requirements. In [4] similar comparison was carried out on five types of rotor magnet topologies to compare the performance of IPM vs. SPM. The study was performed by determining the characteristics of motors with the different rotor topologies and a stator that was the same for all of the variants. The rotor outer diameter, length, type of the magnet and the magnet thickness were kept the same for all possibilities. It was also determined that buried magnet topologies have an output power less than the surface magnet topologies, as well as higher THD. In particular SPM had 5% advantage in maximum power output over the IPM for the two machines of the same ratings as well as 2% THD advantage. In addition in [2] Cross *et al.* concluded that compared to the embedded magnet design, one important advantage of the surface mounted magnets is the smaller amount of magnet material needed in the design (in integer-slot machines). If the same power is needed from the same machine size, the surface mounted magnet machine needs less magnet material than the corresponding machine with embedded magnets. This is due to the following two facts: in the embedded-magnets-case there is always a considerable amount of leakage flux in the end regions of the permanent magnets. Results will show that up to 18% less magnetic material is used in SPM versus IPM for the machines of the same power rating.

The remaining part of this section will compare the two topologies, IPM and SPM for the given application. For the purpose of this work in all further comparison smaller, scaled version of the motor-generator design will be considered. Both machines were designed for rated condition of 6kW 6000 RPM and 220V$_{L-L}$. The active size of the machines, number of poles and flux per pole are kept the same for both machines as well as the size of the frame. It was established through Flux 2D FEM simulation that magnet width had an effect on maximum torque and torque ripple of the machine. The relative width of the magnets for each machine were optimized for maximum torque to 0.8 for IPM and SPM with SPP=1/2 and 0.86 for SPP=2/7.The details of the SPM machine are presented in Table 4.3.

The IPM machine considered here is the one with distributed windings 18 poles and the rotor topology shown in Figure 4.2.

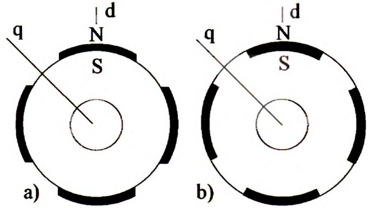

Figure 4.1: SPM and IPM rotor configuration considered in the comparison

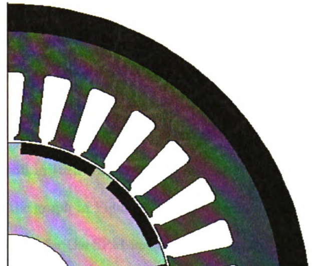

Figure 4.2: 18-pole, 6kW IPM Machine

Slot opening width	2.5 [mm]
Slot top width	**5.4 [mm]**
Slot height	**24.9 [mm]**
Tooth width	**7.4 [mm]**
Slot bottom width	7.6 [mm]
Slot opening height	3.0 [mm]
Back iron depth	5.4 [mm]
Phase resistance	0.72 [Ω]
Magnet depth	6.3 [mm]

Table 4.1: Specification of the IPM machine

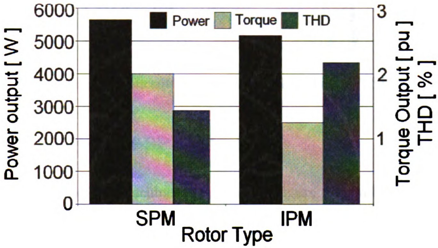

Figure 4.3: Torque, Power and THD of 6kW SPM and IPM Machines

It is clear that the SPM will provide higher output power and torque as well as lower THD, which will in turn reduce iron and magnet losses as it will be shown in later section. From the graph in Figure 4.3. it can be seen that the efficiency of IPM is 88% compared to 92% for the SPM machine. The maximum torque output for the SPM is 2.1 pu, while the maximum torque of IPM is less than 1.5 pu.

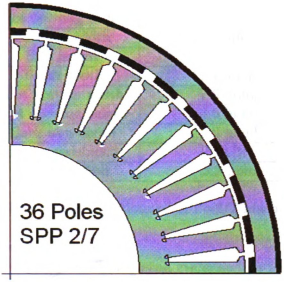

Figure 4.4: Concentrated Winding SPM with 2/7 SPP

4.1.2 Comparison of SPM Machines

The geometries of the two machines are shown in Figure 4.4. and Figure 4.5 respectively. The detailed specifications of the SPP =2/7 and the SPP=1/2 machines are provided in the Tables 4.2 and 4.3 respectively. The analysis is performed on 6kW machines at 6000 RPM. In order to compare the candidates we calculate the losses of the machines to obtain the operating point efficiency as well as the maximum torque capabilities.

4.1.3 Torque Capability

A set of computations were performed to examine the machines with different slot/p/p so that the maximum torque available could be calculated. The torque calculations obtained from the analysis are summarized in Table 4.5. A common stator with 36

Slot opening width	2.5 [mm]
Slot top width	11.4 [mm]
Slot height	18.9 [mm]
Tooth width	11.4 [mm]
Slot bottom width	7.6 [mm]
Slot opening height	3.0 [mm]
Back iron depth	5.0 [mm]
Phase resistance	0.32 [Ω]
Magnet depth	3.2 [mm]

Table 4.2: Specifications of SPP=2/7 Machine

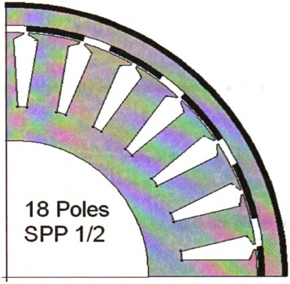

Figure 4.5: Concentrated Winding SPM with 1/2 SPP

Slot opening width	2.5 [mm]
Slot top width	15.8 [mm]
Slot height	18.9 [mm]
Tooth width	13.5 [mm]
Slot bottom width	9.6 [mm]
Slot opening height	3.0 [mm]
Back iron depth	5.0 [mm]
Phase resistance	0.52 [Ω]
Magnet depth	2.9 [mm]

Table 4.3: Specifications of SPP=1/2 Machine

slots was used, while the number of poles was varied to account for the machines between 2/7 SPP to 1/2 SPP. We repeated this analysis for the common stator of 24 slots as well. The relative width of the magnets was also kept constant in all cases at 0.86. For the comparison, the following parameters were kept constant:

- Rated Power
- Speed
- Current density $10A/mm^2$

Calculating torque analytically is based on the back EMF waveform.

$$T_{em} = \frac{1}{\omega_r}\left[e_a i_a + e_b i_b + e_c i_c\right] \tag{4.1}$$

e_a, e_b, e_c are back EMF waveforms while i_a, i_b, i_c are phase current waveforms. ω_r is the rotor mechanical speed.

It is clear from the Table 4.4 that the 1/2 SPP machine provides the best performance in terms of maximum torque capability of about 1.8pu, while the 2/7 slot/pole/phase configuration is only capable of achieving about 60% of that performance.

We will now look at the two particular machines we have designed (1/2 SPP) and (2/7 SPP) with the parameters provided in the Tables 4.2 and 4.3 respectively. From equation we can also find maximum power. Fig. 4.6 shows calculated maximum power vs. speed comparison for SPP = 1/2 and SPP = 2/7 machines.

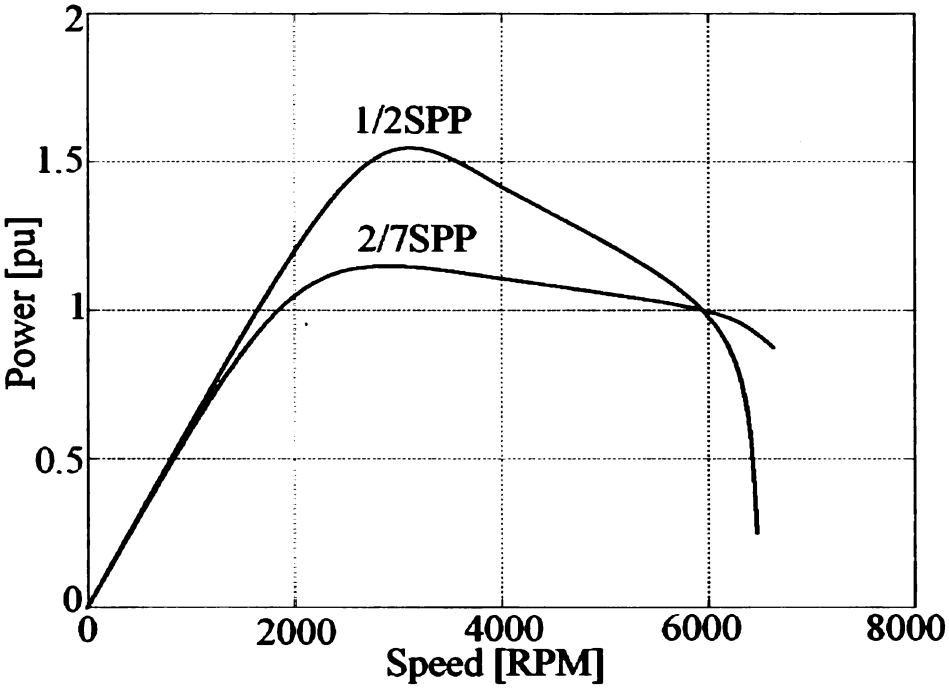

Figure 4.6: Power-Speed Curve

Although the 2/7 SPP machine has an advantage in terms of extended speed range, the 1/2 SPP machine has better performance in terms of maximum power, which is more significant here, considering that for the given application the machine will be operated at a fixed speed. The torque curves as a functions of the load angle for the 24-slot surface magnet machines with different pole numbers are shown in figure below.From the Figure 4.7 it can be observed that the machine with half a slot per pole per phase (p=16) provides the best performance in terms of maximum torque capability of about 2pu, while the 2/7 slot/pole/phase configuration (p=28) is only able of achieving about 60% of that. Table 4.4 summarizes the maximum torque capability of various SPP combinations. We now turn our focus on comparing the efficiencies of those machines.

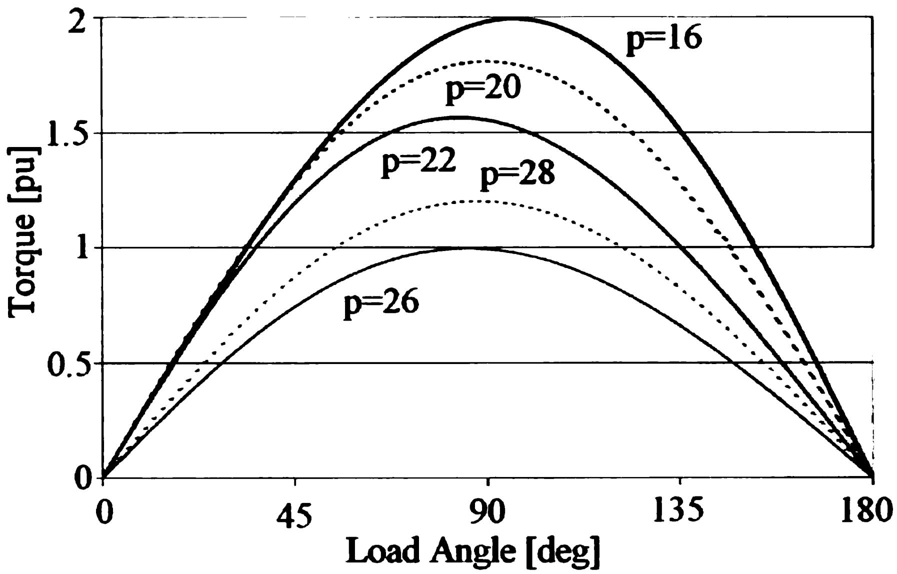

Figure 4.7: Torque Vs. load angle for SPM with 24 slots

Slots/Poles	Winding Factor	Max. Torque [pu]
24/28	0.933	1.26 @ 2200 RPM
24/20	0.933	1.64 @ 2700 RPM
24/16	0.866	2.01 @ 3400 RPM
36/42	0.933	1.16 @ 2500 RPM
36/30	0.933	1.42 @ 2900 RPM
36/24	0.866	1.81 @ 3400 RPM

Table 4.4: Maximum Torque of SPM with Various SPP

Parameter	Analytical	Simulated
SPP = 1/2		
Speed [RPM]	6000	6000
Power factor	0.97	0.97
T_{max} [pu]	2.2	2.0
P_{fe}	168	211
P_{cu}	131	156
P_{mag}	95	130
P_{tot}	394	471
Efficiency [%]	93	92
SPP = 2/7		
Speed [RPM]	6000	6000
Power factor	0.97	0.97
T_{max} [pu]	1.4	1.3
P_{fe} [W]	182	230
P_{cu} [W]	107	139
P_{mag} [W]	132	142
P_{tot} [W]	391	511
Efficiency [%]	94	91

Table 4.5: Summary of losses for the two machines

4.1.4 Losses and Efficiency

The losses and the efficiency are calculated as described in Chapter 3. The Table 4.5 presents a summary of the results. Although the efficiency of the half slot per pole per phase machine is slightly higher, the difference is so insignificant when compared to the accuracy of the methods used in calculating the losses of the machines. However looking at the maximum torque capability it is clear that the SPP $= 1/2$ provides much better performance and it would therefore be more suitable candidate for integrated starter/generator application, considering that high starting torque would be required from the chosen machine.

4.1.5 Size and Weight Comparison

Considering the machine design for integrated starter-generator in automotive application one of the major considerations besides performance is the size of the machine. Table 4.6 summarizes the size and weight comparison of the two machine candidates considered here. It can be seen from the Table 4.6 that the SPP=2/7 design will require somewhat less magnet material which indicates more cost-effective design. However the half slot-per-pole-per-phase machine will have an advantage in terms of overall weight and length which are reduced by 7% and 10% respectively compared to SPP=2/7 design.

	SPP = 2/7	SPP = 1/2
Active length [mm]	162.9	151.8
Copper Mass [kg]	2.64	2.22
Magnet Mass [kg]	1.44	1.51
Iron Mass [kg]	6.81	6.16
Total Mass [kg]	10.9	9.89

Table 4.6: Summary of size comparison

CHAPTER 5

Control of PMAC

Rotor position information is necessary for Field Oriented Control (FOC) of Permanent Magnet Synchronous Machines (PMSM). It is particularly attractive to obtain the rotor position information without shaft sensors, since they increase the cost of the overall system and degrade the reliability.

This chapter provides an overview of previously developed control methods for PMAC machine without rotor position sensors, as well as the advantages and challenges involved with using each particular method. Survey of available high -frequency injection methods for low speed operation as well as the back EMF methods is presented. Specifically, the issue of control without rotor position sensors, in the context of saturation is discussed in both back EMF and high-frequency injection methods, and the errors due to saturation.

The methods presented here will be discussed again in chapters 6 and 7 in the context of the new high-gain observer. Existing methods are improved to account for entire operating range of the machine and enhance the accuracy of shaft-sensorless position estimation under saturation.

5.1 Back EMF Methods

The back EMF technique is based on the fact that the spinning rotor magnets will induce a voltage (the back EMF) at the windings of the machine. This voltage can be integrated to find the stator flux [40]. From the stator flux vector, and the torque angle, the rotor speed and in turns the rotor flux position can be estimated. However since the voltages induced are dependant on the speed, this technique falls short in estimating a rotor position at low or zero speeds. This challenge of control at low and zero speeds has led to increased exploitation of machine phenomena not represented in the basic models, i.e. anisotropic properties, for position-sensorless control.

5.2 High Frequency Injection Control

Injecting the signals of different, higher frequency than fundamental and observing the response of the machine, serves for detecting spatial orientations of existing anisotropic properties which can further be used to extract the field and rotor angles. A number of different methods for this purpose have been introduced over the past ten years [34] - [33], and while they differ in a number of ways i.e. with respect to the frequency of injected signal, type of the signal injected (voltage [31] or current [32]) and so on, they can all be classified into two groups: injection of a rotating space vector [34] - [38] or injection of a stationary oscillating space vector [32] - [33]. While both groups utilize the same phenomena, and relay on magnetic saliency and/or saturation as it relates to the rotor position, the major difference comes from the feedback information. The injected oscillating, stationary space vector contains the estimated $d - axis$ position and the feedback signal provides the information about position error. For the rotating space vector the rotor position is tracked using the saliency, which includes the rotor position i.e. the feedback signal contains the actual rotor position information. In this work our focus will remain on oscillating space vector injection, since this method is more applicable to SPM machines.

5.3 High Frequency Model

Since this work focuses on high frequency injection methods, it is useful to develop first a high frequency model of the machine. If the high-frequency components in (2.7) are only considered by assuming that a high-frequency signal is injected into the machine, the back-EMF voltage (the second term on the right hand side of (2.7) can be neglected because it does not have any high-frequency component. It should be noted that diagonal terms in the impedance matrix in (2.7) include terms proportional to the time derivative of currents, but cross-coupling terms (off-diagonal terms) do not have these terms. This means that the cross-coupling (off-diagonal) terms in the voltage equations can be neglected in steady state if the frequency of the injected signal is sufficiently high compared to the rotor speed, because the time-derivative terms of currents are proportional to the high frequency. Based on the simplification, the high-frequency components of the voltage equations of an SMPM machine can be expressed as (5.1):

$$\begin{bmatrix} v^r_{dshf} \\ v^r_{qshf} \end{bmatrix} = \begin{bmatrix} R_{dhf} + L_{dhf}p & 0 \\ 0 & R_{qhf} + L_{qhf}p \end{bmatrix} \begin{bmatrix} i^r_{dshf} \\ i^r_{qshf} \end{bmatrix} \tag{5.1}$$

For the injected signal of frequency ω_h we can rewrite the equation as:

$$\begin{bmatrix} v^r_{dshf} \\ v^r_{qshf} \end{bmatrix} = \begin{bmatrix} R_{dhf} + j\omega_h L_{dhf} & 0 \\ 0 & R_{qhf} + j\omega_h L_{qhf} \end{bmatrix} \begin{bmatrix} i^r_{dshf} \\ i^r_{qshf} \end{bmatrix} \tag{5.2}$$

In addition we define the following high-frequency impedances:

$$Z_{dhf} = R_{dhf} + j\omega_h L_{dhf} \tag{5.3}$$

$$Z_{qhf} = R_{qhf} + j\omega_h L_{qhf} \tag{5.4}$$

Then (5.2) becomes:

$$\begin{bmatrix} v^r_{dshf} \\ v^r_{qshf} \end{bmatrix} = \begin{bmatrix} Z_{dhf} & 0 \\ 0 & Z_{qhf} \end{bmatrix} \begin{bmatrix} i^r_{dshf} \\ i^r_{qshf} \end{bmatrix} \tag{5.5}$$

The equivalent circuit of the machine for d and q axes is shown in the Figure 5.1.Since the inductances are functions of rotor position, the impedances Z_{dhf} and Z_{qhf} also contain rotor position information. If we assume that the voltage is the injected signal and the current is the observed feedback, calculating the impedance matrix becomes a matter of simple algebra. The calculated impedance matrix will contain either the rotor position or the error between the actual rotor position and the estimated rotor

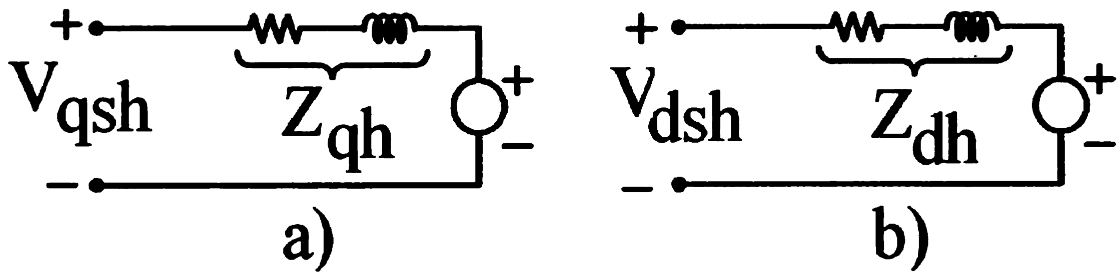

Figure 5.1: d,q -axis equivalent circuits, Ji-Hoon [41]

position, depending on whether the rotating space vector or stationary oscillating space vector is injected.

5.4 General Concept of High-Frequency Injection

From equation (5.2) it can be seen that the inductance component is dominant in the high-frequency impedance, because this impedance is proportional to the frequency of the injected signal. The variation of the $d - axis$ high-frequency impedance is much larger than the variation of the $q - axis$ high frequency impedance when the magnitude of the injected high frequency signal is varied. These can be explained using the high-frequency flux path and the physical location of windings as in Figure 5.2.This figure shows the physical locations of windings and flux paths in a two-pole SMPM machine. Actual $d - axis$ windings are located in the $q - axis$, and $q - axis$ windings are located in the $d - axis$ in the rotor reference frame. Because the high-frequency flux passes through the stator leakage path, resultant flux from high-frequency voltage injected on the axis passes as flux B in the figure, and resultant flux from high-frequency voltage injected on the axis passes as flux A in the figure.

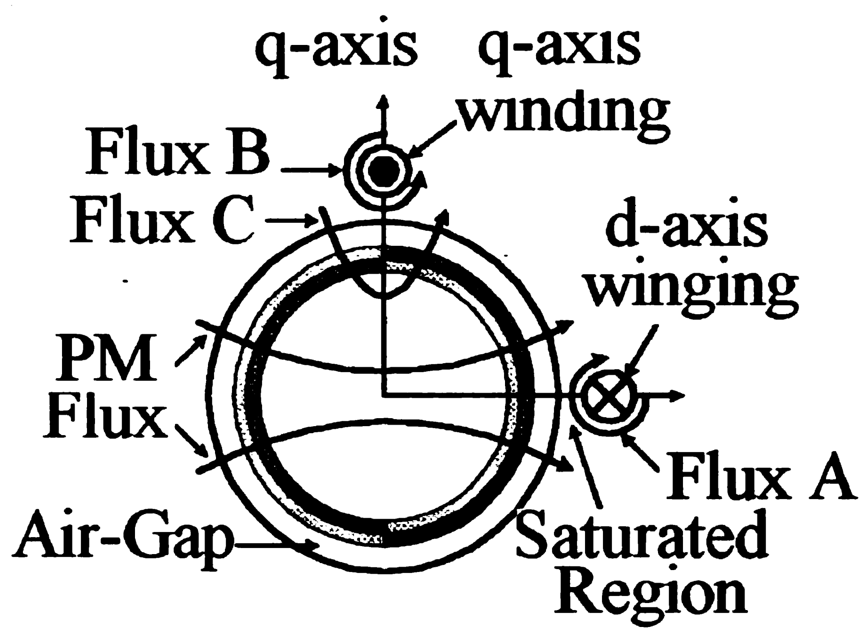

Figure 5.2: Windings and flux paths in two-pole SMPM machine. Ji-Hoon [41]

Therefore, $d-axis$ inductance is larger than $q-axis$ inductance because flux A passes through the highly saturated part of the stator. This is the difference between the inductance characteristics in the fundamental component and in the high-frequency component. When the magnitude of the high-frequency voltage signal injected on the $d-axis$ becomes large, some fluxes will pass through the air gap and rotor because the density of the main flux is not so high where the $d-axis$ winding is located. Therefore, some of the resultant flux from $d-axis$ injection can pass as flux C in the figure. However, the resultant flux from $q-axis$ injection cannot pass as this is due to high flux density around the winding. Therefore, the $d-axis$ inductance is smaller than the $q-axis$ inductance. It is assumed that the high frequency flux will not penetrate the rotor surface because of eddy currents in the rotor magnets.

5.5 Injection of Oscillating Current Space Vector

In this section the estimation of the rotor position employing alternating voltage space vector injection is described. Consider the previously derived equation (5.2) for the high frequency model of PMSM, which is rewritten here as a reminder:

$$\begin{bmatrix} v^r_{dshf} \\ v^r_{qshf} \end{bmatrix} = \begin{bmatrix} R_{dhf} + L_{dhf}p & 0 \\ 0 & R_{qhf} + L_{qhf}p \end{bmatrix} \begin{bmatrix} i^r_{dshf} \\ i^r_{qshf} \end{bmatrix}. \tag{5.6}$$

This equation is in the actual rotor frame of reference. The high frequency pulsating voltage space vector is injected in the estimated (denoted by $\hat{r}$) $d - axis$ direction, and the induced current is measured

$$\begin{bmatrix} v^{\hat{r}}_{dhf} \\ v^{\hat{r}}_{qhf} \end{bmatrix} = V_c \begin{bmatrix} \cos(\omega_c t) \\ 0 \end{bmatrix}. \tag{5.7}$$

We can rewrite the equation (5.2) as:

$$\begin{bmatrix} v^{\hat{r}}_{dshf} \\ v^{\hat{r}}_{qs}hf \end{bmatrix} = \begin{bmatrix} Z^{\hat{r}}_{dhf} & 0 \\ 0 & Z^{\hat{r}}_{qhf} \end{bmatrix} \begin{bmatrix} i^{\hat{r}}_{dshf} \\ i^{\hat{r}}_{qshf} \end{bmatrix}. \tag{5.8}$$

In control without rotor position sensors, the estimated rotor reference frame should be used instead of the actual one because the actual rotor position is not known. The high-frequency voltage equations in the estimated rotor reference frame can be expressed as (5.10) by transforming (5.6) with the definition of rotor position estimation error as in (5.9)

$$\tilde{\theta}_r \equiv \theta_r - \hat{\theta}_r \tag{5.9}$$

$$\begin{bmatrix} v^{\hat{r}}_{dshf} \\ v^{\hat{r}}_{qs}hf \end{bmatrix} = R(\tilde{\theta}_r)^{-1} \begin{bmatrix} Z^{\hat{r}}_{dhf} & 0 \\ 0 & Z^{\hat{r}}_{qhf} \end{bmatrix} R(\tilde{\theta}_r) \begin{bmatrix} i^{\hat{r}}_{dshf} \\ i^{\hat{r}}_{qshf} \end{bmatrix} \tag{5.10}$$

where

$$R(\theta_r) = \begin{bmatrix} \cos\theta & \sin\theta \\ -\sin\theta & \cos\theta \end{bmatrix}. \tag{5.11}$$

Combining the two we get:

$$\begin{bmatrix} v^{\hat{r}}_{dshf} \\ v^{\hat{r}}_{qshf} \end{bmatrix} = \begin{bmatrix} Z_{avg} + \frac{1}{2}Z_{diff}\cos 2\tilde{\theta}_r & \frac{1}{2}Z_{diff}\sin 2\tilde{\theta}_r \\ \frac{1}{2}Z_{diff}\sin 2\tilde{\theta}_r & Z_{avg} - \frac{1}{2}Z_{diff}\cos 2\tilde{\theta}_r \end{bmatrix} \begin{bmatrix} i^{\hat{r}}_{dshf} \\ i^{\hat{r}}_{qshf} \end{bmatrix}, \tag{5.12}$$

where Z_{dhf} and Z_{qhf} are d and q axis impedances in the estimated rotor frame of reference while the Z_{chf} is the cross coupling high frequency impedance. We define those values as:

$$Z^{r}_{dhf} = Z_{avg} + \frac{1}{2}Z_{diff}\cos 2\tilde{\theta}_r \tag{5.13}$$

$$Z^{r}_{qhf} = Z_{avg} - \frac{1}{2}Z_{diff}\cos 2\tilde{\theta}_r \tag{5.14}$$

$$Z^{r}_{chf} = \frac{1}{2}Z_{diff}\sin 2\tilde{\theta}_r \tag{5.15}$$

and Z_{avg} and Z_{diff} are the average and difference of d and q axes impedances defined as:

$$Z_{avg} \equiv \frac{Z^r_{dhf} + Z^r_{qhf}}{2} \tag{5.16}$$

$$Z^r_{chf} \equiv Z^r_{dhf} - Z^r_{qhf} \tag{5.17}$$

After the high-frequency voltage equations in the estimated rotor reference frame are obtained, a high-frequency model of the SMPM machine in the estimated rotor reference frame can be constructed as (5.18). It should be noted that the impedance matrix in the estimated rotor reference frame has cross-coupling terms, even though there are no such terms in the impedance matrix in the actual rotor reference frame [compare (5.10) with (5.6)]

$$\begin{bmatrix} v^{\hat{r}}_{dshf} \\ v^{\hat{r}}_{qshf} \end{bmatrix} = \begin{bmatrix} Z^{\tilde{r}}_{dhf} & Z^{\tilde{r}}_{chf} \\ Z^{\tilde{r}}_{chf} & Z^{\tilde{r}}_{qhf} \end{bmatrix} \begin{bmatrix} i^{\hat{r}}_{dshf} \\ i^{\hat{r}}_{qshf} \end{bmatrix} \tag{5.18}$$

Moreover it can be observed that the high-frequency impedances in the estimated rotor reference frame are functions of the rotor position estimation error. Particularly, the cross-coupling high-frequency impedance in the estimated rotor reference frame ($Z^{\tilde{r}}_{chf}$) is proportional to the sine of the rotor position estimation error ($\tilde{\theta}_r$) if the high-frequency impedance difference is not zero. This means that the actual rotor position can be estimated by forcing the cross-coupling high-frequency impedance to zero. Figure 5.1 shows the d and q axes equivalent circuits of an SMPM machine at high frequency in the estimated rotor reference frame. The current controller can be designed to force the q axis current to zero by controlling the estimated rotor position angle. Therefore the estimated $d - axis$ angle of the injected space vector becomes the true angle. The reason for this is that if the voltage space vector is injected in the $d-$ axis only the $q-$ axis current will be zero. Number of different controller schemes are proposed for this purpose.

5.6 Implementation of a Controller without Rotor Position Sensors

In Section 5.5, it was shown that the cross-coupling high-frequency impedance can be used for rotor position estimation provided that the high-frequency impedance difference is not zero. However, in order to use the cross-coupling high-frequency impedance directly, it is required to know both the high-frequency voltage information and the high-frequency current information very accurately. If the high-frequency voltage information is obtained from the controller, the information is inevitably subject to the error due to the nonlinear characteristics of the pulse-width-modulation (PWM) inverter, such as dead time and zero-current-clamping phenomena. However, the high-frequency current information can be easily obtained using current sensors which are already part of the drive system [41]. Therefore, an alternative method based only on the high-frequency current information is described in this subsection. The high-frequency voltage equations in (5.18) can be expressed as in (5.19) with regard to the high-frequency currents by using the relationships between high-frequency impedances in (5.6) and (5.8)

$$\begin{bmatrix} i^r_{dshf} \\ i^r_{qshf} \end{bmatrix} = \frac{1}{Z^r_{dhf}Z^r_{qhf} - Z^{r2}_{chf}} \begin{bmatrix} Z^r_{dhf} & -Z^r_{chf} \\ -Z^r_{chf} & Z^r_{qhf} \end{bmatrix} \begin{bmatrix} v^r_{dshf} \\ v^r_{qs}hf \end{bmatrix} \tag{5.19}$$

$$= \frac{1}{Z^r_{dhf}Z^r_{qhf}} \begin{bmatrix} Z^r_{dhf} & -Z^r_{chf} \\ -Z^r_{chf} & Z^r_{qhf} \end{bmatrix} \begin{bmatrix} v^r_{dshf} \\ v^r_{qs}hf \end{bmatrix}$$

In order to use the voltage and current relationships through the cross-coupling high-frequency impedance, there are two possible injection and estimation schemes using the high-frequency current information as follows.

- The fluctuating high-frequency voltage signal is injected only on the $d-axis$ in the estimated rotor reference frame as in [33] and high-frequency current on the axis in the estimated rotor reference frame is used (5.20)

$$\begin{bmatrix} v^{\hat{r}}_{dhf} \\ v^{\hat{r}}_{qhf} \end{bmatrix} = V_c \begin{bmatrix} \cos(\omega_c t) \\ 0 \end{bmatrix} \tag{5.20}$$

- The fluctuating high-frequency voltage signal is injected only on the $q - axis$ in the estimated rotor reference frame as in (5.21) and high-frequency current on the $q - axis$ in the estimated rotor reference frame is used

$$\begin{bmatrix} v^{\hat{r}}_{dhf} \\ v^{\hat{r}}_{qhf} \end{bmatrix} = V_c \begin{bmatrix} 0 \\ \cos(\omega_c t) \end{bmatrix} \tag{5.21}$$

In (5.20) and (5.21), V_c and ω_c are magnitude and frequency of the injected high-frequency voltage signal, respectively. Between the two injection algorithms, injection of the fluctuating high-frequency voltage signal only on the $d-axis$ is better than injection of the signal only on the $q-axis$ in regard to torque ripples and additional losses from the high-frequency currents. High-frequency voltage generates high-frequency current on the same axis. Therefore, if the high-frequency voltage is injected on the estimated $q-axis$, it generates substantial ripple torque when the rotor position estimation error is small. Furthermore if the SMPM machine has larger $d-axis$ high-frequency impedance than $q-axis$ high-frequency impedance the magnitude of high-frequency current is larger when high-frequency voltage is injected only on the estimated $q-axis$ than when high-frequency voltage is injected only on the estimated $d-axis$, provided that the estimated rotor position is small. Based on these facts, the high-frequency voltage signal is injected only on the $d-axis$ in the estimated rotor reference frame and the $q-axis$ high-frequency current in the estimated rotor reference frame is used in the rotor position and speed estimation scheme described in this study. Note that when the error between the estimated and actual $d-axis$ becomes zero so does the i_q, since the $d-axis$ voltage will only produce the $d-axis$ current. From (5.6)–(5.20), the $q-axis$ high-frequency current in the estimated rotor reference frame can be expressed as:

$$
\begin{aligned}
i^{\tilde{r}}_{qshf} &= \frac{-Z^{\tilde{r}}_{chf}}{Z^{\tilde{r}}_{qhf}Z^{\tilde{r}}_{chf}} V_{inj}\cos(\omega_{hf}t) && (5.22)\\
&= -\frac{1}{2}\frac{(r_{diff}+j\omega_h L_{diff})V_{inj}\sin(2\tilde{\theta}_r)}{(r^r_{dhf}+j\omega_h L^r_{dhf})(r^r_{qhf}+j\omega_h L^r_{qhf})}\cos(\omega_{hf}t) && (5.23)
\end{aligned}
$$

If the high-frequency impedances from the high-frequency inductances are sufficiently larger than the high frequency impedances from the high-frequency resistances we can write the following:

$$
\begin{aligned}
Z^r_{dhf} &= r_{dhf} + j\omega L_{dhf} \doteq j\omega_{hf} L_{dhf}, \\
Z^r_{qhf} &= r_{qhf} + j\omega L_{qhf} \doteq j\omega_{hf} L_{qhf},
\end{aligned}
\tag{5.24}
$$

now the current becomes:

$$
i^r_{qshf} = \frac{v_{inj}}{2}\left[\frac{r_{diff}\cos(\omega_{hf}t)}{\omega^2_{hf}L^r_{dhf}L^r_{qhf}} - \frac{\omega_{hf}L_{diff}\sin(\omega_{hf}t)}{\omega^2_{hf}L^r_{dhf}L^r_{qhf}}\right]\sin 2\tilde{\theta}_r \tag{5.25}
$$

The position-sensorless control scheme uses only the second term on the right-hand side of (3.20). This utilization has mainly two characteristics: The saturation effect due to the PM flux is more effective on the inductance than the resistance. Therefore, the difference of inductances is more significant than the resistance difference. This makes the utilization of the second term in (5.25) more effective than the utilization of first term or utilization of both terms.

• The magnitude of the cross-coupling term is very small compared to the diagonal term. The effect of the neglected term is increased as the rotor speed increases and can deteriorate the rotor position estimation. However, the main constraint of this sensorless control scheme is not from the rotor speed effect itself but from the insufficient voltage due to increasing back-EMF voltage. In order to obtain the rotor position estimation error from (5.25), a signal processing method using a band-pass

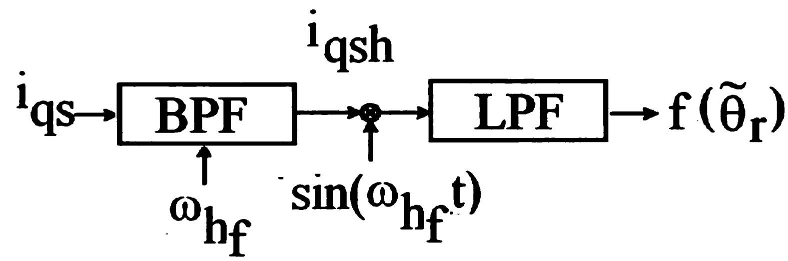

Figure 5.3: Block diagram of the Signal Processing [41]

filter (BPF) , a multiplication, and a low-pass filter (LPF) is used as follows.

- A BPF is used in order to extract the injected frequency component from the $q-axis$ current in the estimated rotor reference frame.

- A multiplication is used in order to extract the orthogonal term to the injected high-frequency voltage from the high frequency current.

- An LPF is used to eliminate the second-order harmonic term in the obtained signal.

The high-frequency component of $q-axis$ current in the estimated rotor reference frame in (5.25) is obtained through a BPF. If a signal is multiplied by this high-frequency component of $q-axis$ current as in (5.26), a signal consisting of two components can be obtained [41].

These components are a dc component and a second-order harmonic one. Therefore, a signal containing the rotor position estimation error can be obtained if the signal in (5.26) is passed through an LPF with appropriate corner frequency:

$$-i^{r}_{qshf}\sin(\omega_{hf}t) = \frac{V_{inj}\sin 2\tilde{\theta}_r}{2\omega^2_{hf}L_{dhf}L_{qhf}}\left[\frac{\omega_{hf}L_{diff}}{2} - |z_{diff}|\sin(\omega_{hf}t-\phi)\right] \quad (5.26)$$

where

$$\left|z_{diff}\right| = \sqrt{r_{diff}^{2} + (\omega_{hf} L_{diff})^{2}} \tag{5.27}$$

and

$$\tan\phi = \frac{\omega_{hf} L_{diff}}{r_{diff}} \tag{5.28}$$

$$f(\tilde{\theta}_r) = LPF\left[-i_{qshf}^{r}\sin(\omega_{hf}t)\right] = \frac{V_{inj}L_{diff}}{4\omega_{hf}L_{dhf}^{r}L_{qhf}^{r}}\sin 2\tilde{\theta}_r \tag{5.29}$$

If the position estimation error is sufficiently small, the input signal can be approximated as:

$$f(\tilde{\theta}_r) = \frac{V_{inj}L_{diff}}{2\omega_{hf}L_{dhf}^{r}L_{qhf}^{r}}\tilde{\theta}_r = K_{err}\tilde{\theta}_r \tag{5.30}$$

Figure 5.3. shows the block diagram of a signal processing procedure to obtain the rotor position estimation error information. It can be noted that the signal processing procedure does not use any additional information. The $q-axis$ current in the estimated rotor reference frame is already obtained because it should be used in the synchronous reference frame current controller. In order to estimate the rotor position and speed from rotor position estimation error information in (5.30), a rotor position and speed estimator should be used. Various speed and rotor position observers are available for this purpose and since this is not a focus of the study presented here, a simple PI controller is used to demonstrate the complete control system. Figure 5.4 shows the block diagram of the rotor position and speed estimator when a PI controller and an integrator are used to estimate the rotor position [41].

If a PI controller and an integrator are used as the rotor position estimator, the transfer function from the actual rotor position to the estimated one can be expressed

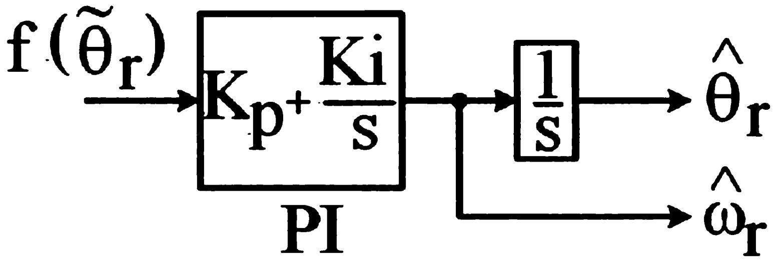

Figure 5.4: Controller for Rotor Position and Speed Estimation [41]

as:

$$\frac{\hat{\theta}_r}{\theta_r} = \frac{K_{P\hat{\omega}} K_{err} S + K_{I\omega} K_{err}}{S^2 + K_{P\hat{\omega}} K_{err} S + K_{I\omega} K_{err}} \tag{5.31}$$

The transfer function in (5.31) has a unity gain in steady state, which means that the rotor position can be estimated without error in steady state. In this case, the rotor speed can be obtained from the output of the PI controller without an LPF because the output of the PI controller does not have much ripple.

CHAPTER 6

Saturation

It is well documented in the literature that the error in the estimate of rotor position increases with the load current [14]. Guglielmi *et al.* showed in [15] that an error exists in rotor position estimation due to cross-magnetic saturation between d- and q-axes. Stumberger *et al.* in [16] evaluated the effect of saturation and cross-magnetization for IPM, but offered no solution for compensating for the error.

Chapter 5, provided an overview of the control strategies used for PMAC machines, but none of them account for the saturation effects. In order to develop a controller which accounts for saturation, a model of saturated machine is developed first. In particular a non linear model of SPM machine is required.

This chapter presents the theory of the saturation of PMAC machine and necessary model adjustments to account for this phenomena. A non-linear model of the machine under saturation is derived. FEA characterization of SPM machine under saturation is also presented.

The model developed here is used in chapter 7 to design a new high-gain non-linear observer and controller for control of PMAC machines without position sensors, which accounts for the entire operating range of the machine, including the saturation.

6.1 Theory

Cross-magnetization complicates the sensorless control of non-salient AC machines, like the surface magnet synchronous motors. The motor currents influence position estimation for low speed based on "saturation induced" saliencies. This chapter considers cross-saturation effects to explain the magnetic-axis shift under loaded conditions and discusses the influence of the operating point on the saliency. Because this saliency is very small, the stator currents strongly affect it. Accordingly, the quality of saliency-based position estimation depends much on the machine operating point. The most pronounced effect is the shift of the magnetic-axis under load, i.e. an estimation error produced by the quadrate-axis current. Even though saturation causes the saliency, many authors do not pay much attention to the implications of the non-linear behavior. Several factors may change from an unloaded to a loaded machine: flux and saturation levels, flux and saturation orientation and saturation regions. To demonstrate the basic idea we use machine control where $i_d = 0$ and $i_q = i_s$. The stator flux increases when the machine is loaded (Figure 6.1). The resulting flux vector is shifted by a term $\delta\theta$ due to the loading of the machine [40].The shift in the stator flux results in a shift of the stator yoke and teeth saturation regions.

$$\delta\theta = a\sin\left[\frac{i_q L_q}{\sqrt{\psi_M^2 + \left(i_q L_q\right)^2}}\right] \tag{6.1}$$

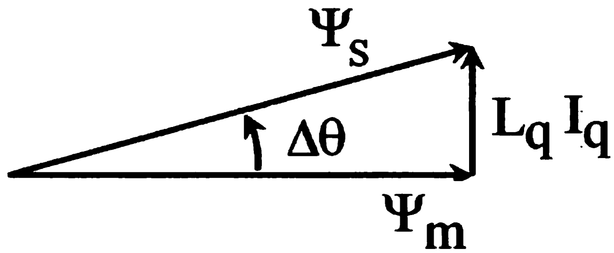

Figure 6.1: Phasor Diagram of Flux Under Load

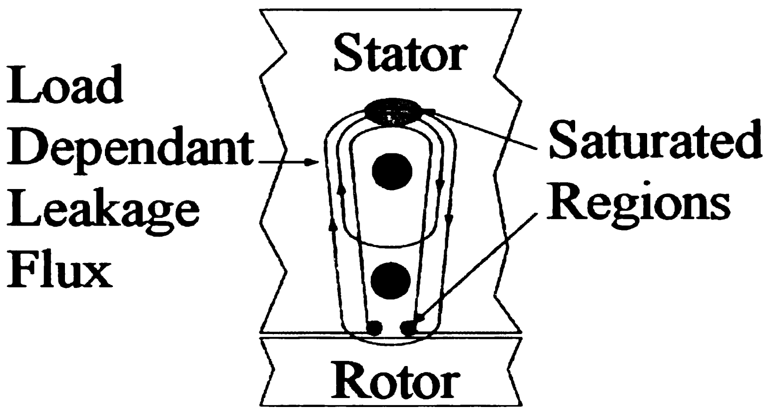

Figure 6.2: Leakage Flux

In addition to the main flux effects the leakage effects must also be included. Figure 6.2 illustrates typical saturation regions due to the leakage flux from the load current. This type of saturation will result in a load dependent term in the $q-axis$ leakage inductance.

With increasing $q-axis$ current the detected angle diverges more and more from the real rotor position as will be shown in the following analysis and simulation results. If the q-component of the armature current is positive, the identified axis is shifted tendentiously to the $q-axis$ [40]. This shift of the magnetic axis is particularly distinct in the case of non-salient-pole machines. An explanation is that the stator current causes changes of the local iron saturation level. Loading of the machine increases the main and leakage flux levels and displaces the most saturated regions.

6.2 Nonlinear model approach

To describe and analyze the impacts of the armature current for the flux linkages the simple approach is used

$$\psi_d = \psi_d(i_d, i_q) \tag{6.2}$$

$$\psi_q = \psi_q(i_d, i_q) \tag{6.3}$$

it is chosen

$$\psi_m = \psi|_{(i_d=0, i_q=0)} \tag{6.4}$$

This approach has the advantage that it includes saturation and cross-saturation effects and needs no assumptions regarding the regions of saturation. Saturation in the main and leakage flux paths can produce this saliency. The approximation by smooth functions, as power series, is useful for the practical implementation of (6.2) and (6.4). With the general nonlinear approach, the flux derivatives have to be expressed by:

$$\frac{d\psi_d}{dt} = \frac{\partial\psi_d}{\partial i_d}\frac{di_d}{dt} + \frac{\partial\psi_d}{\partial i_q}\frac{di_q}{dt} \tag{6.5}$$

$$\frac{d\psi_q}{dt} = \frac{\partial\psi_q}{\partial i_d}\frac{di_d}{dt} + \frac{\partial\psi_q}{\partial i_q}\frac{di_q}{dt} \tag{6.6}$$

Considering the PMSM voltage equation in the stator frame of reference

$$\begin{bmatrix} v_x^s \\ v_y^s \end{bmatrix} = \begin{bmatrix} L_{11} & L_{12} \\ L_{21} & L_{22} \end{bmatrix} p \begin{bmatrix} i_x^s \\ i_y^s \end{bmatrix} + \begin{bmatrix} e_x^s \\ e_y^s \end{bmatrix} \tag{6.7}$$

where

$$L_{11} = L_0 + L_1 \cos(2\theta) \tag{6.8}$$

$$L_{12} = L_{21} = L_1 \sin(2\theta) \tag{6.9}$$

$$L_{22} = L_0 - L_1 \cos(2\theta) \tag{6.10}$$

and

$$e_x^s = -\omega\lambda_{PM} \sin(\theta), e_x^s = \omega\lambda_{PM} \cos(\theta) \tag{6.11}$$

$$L_0 = \frac{L_d + L_q}{2} \tag{6.12}$$

$$L_1 = \frac{L_d - L_q}{2} \tag{6.13}$$

The partial derivatives represent self and mutual incremental inductances

$$\frac{\partial\psi_d}{\partial i_d} = L_{22}(i_d, i_q) \tag{6.14}$$

$$\frac{\partial\psi_q}{\partial i_q} = L_{11}(i_d, i_q) \tag{6.15}$$

$$\frac{\partial\psi_d}{\partial i_q} = L_{12}(i_d, i_q) = \frac{\partial\psi_q}{\partial i_d} = L_{21}(i_d, i_q) \tag{6.16}$$

respectively. In contrast to the linear case, the incremental self inductances in (6.5) can differ from the absolute inductances and vary with the current operating point (i_d, i_q) The mutual inductances appear only if cross-saturation coupling exists. The equality $L_{12} = L_{21}$ holds due to the reciprocal theorem, which is strictly valid only for small signals in the loss-less case [39].

$$\begin{bmatrix} v_q^r \\ v_d^r \end{bmatrix} = \begin{bmatrix} R_s + L_{11} & L_{12} \\ L_{21} & R_s + L_{22} \end{bmatrix} p \begin{bmatrix} i_q^r \\ i_d^r \end{bmatrix} \tag{6.17}$$

we again define the error between estimated rotor position and actual rotor position as

$$\tilde{\theta}_r \equiv \theta_r - \hat{\theta}_r \tag{6.18}$$

and representing the model in the rotor position error frame of reference we get the same equation however the inductances in new frame of reference will change

$$\begin{bmatrix} v_{ds}^{\hat{r}} \\ v_{qs}^{\hat{r}} \end{bmatrix} = R(\tilde{\theta}_r)^{-1} \begin{bmatrix} R_s + L_{11} & L_{12} \\ L_{21} & R_s + L_{22} \end{bmatrix} R(\tilde{\theta}_r) \begin{bmatrix} i_{ds}^{\hat{r}} \\ i_{qs}^{\hat{r}} \end{bmatrix} \tag{6.19}$$

where

$$R(\theta_r) = \begin{bmatrix} \cos\theta & \sin\theta \\ -\sin\theta & \cos\theta \end{bmatrix} \tag{6.20}$$

$$\begin{aligned} L_{11}^{\hat{r}} &= L_{avg}^r - (L_{diff}^r \cos 2\tilde{\theta}_r - L_{21}^r \sin 2\tilde{\theta}_r) \\ &= L_{avg}^r - L_p \cos(2(\tilde{\theta}_r - \theta_o) \end{aligned} \tag{6.21}$$

$$
\begin{aligned}
L_{22}^{\hat{r}} &= L_{avg}^{r} + (L_{diff}^{r} \cos 2\tilde{\theta}_r - L_{12}^{r} \sin 2\tilde{\theta}_r) \\
&= L_{avg}^{r} + L_{p}^{r} \cos(2(\tilde{\theta}_r - \theta_o) \qquad (6.22)
\end{aligned}
$$

$$
\begin{aligned}
L_{12}^{\hat{r}} &= L_{21}^{\hat{r}} = \frac{1}{2} L_{diff}^{r} \sin 2\tilde{\theta}_r - L_{12}^{r} \cos 2\tilde{\theta}_r \\
&= L_{p}^{r} \sin(2(\tilde{\theta}_r - \theta_o) \qquad (6.23)
\end{aligned}
$$

and Z_{avg} and Z_{diff} are the average and difference of d and q axes impedances defined as:

$$
L_{avg}^{r} \equiv \frac{L_d^r + L_q^r}{2} \qquad (6.24)
$$

$$
L_{diff}^{r} \equiv \frac{L_d^r - L_q^r}{2} \qquad (6.25)
$$

$$
L_p^r \equiv \sqrt{L_{diff}^{r2} + L_{12}^{r2}} \qquad (6.26)
$$

$$
\theta_o \equiv -\frac{1}{2} \tan^{-1} \left(\frac{L_{12}^r}{L_{diff}^r} \right) \qquad (6.27)
$$

6.3 Error Signal with Saturation Offset

We can see that the inductance is a function of θ_0, which means that the orientation of the saliency was moved away from the direct axis by an angle θ_o. Even in the case of correct model alignment with the rotor ($\tilde{\theta}_r = 0$) the cross-coupling L_{12} is not zero which is according to [42] an obviously misinterpretation as a position error

$$\theta_r = -\theta_o \neq 0 \tag{6.28}$$

Any position-sensorless control, following the concept of tracking the decoupled axes of the machine, will adjust the estimation until the cross-coupling vanishes, i.e. $L_{12}^{\hat{r}} = 0$, and so produce a real position error θ_o dependent on the $q - axis$ current. That means the error in angle estimation can be written as:

$$\hat{\theta} = \frac{1}{2}\tan^{-1}\left[\frac{L_{12}^{\hat{r}} + L_{21}^{\hat{r}}}{L_{11}^{\hat{r}} - L_{22}^{\hat{r}}}\right] + \theta_o(i_d, i_q) \tag{6.29}$$

From equation (6.27) can be seen that the estimation error, θ_o, becomes zero only if the cross coupling is negligible. This is the case either at no-load or if a sufficient geometric saliency masks the effect of a saturation based saliency and prevents the magnetic-axis from moving away from the rotor direct-axis. The new error in the angle θ should be rewritten as:

$$\tilde{\theta}_r \equiv \theta_r - \hat{\theta}_r + \theta_o \tag{6.30}$$

The next step is to derive a control algorithm based on this new angle error.

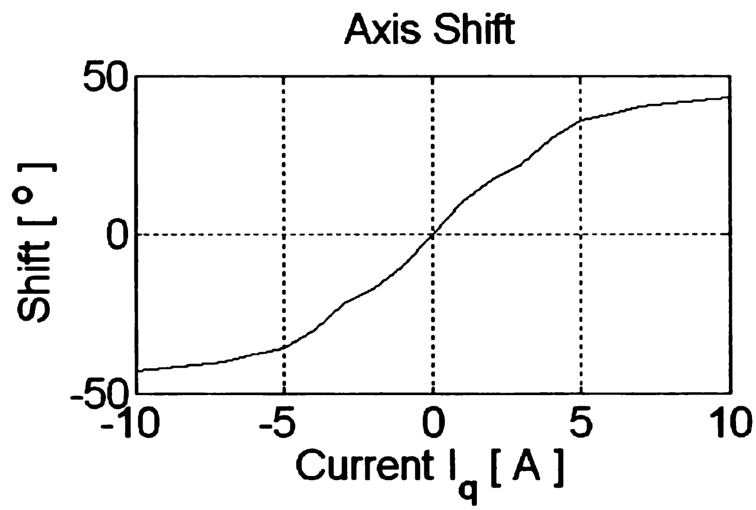

Figure 6.3: Magnetic Axis Shift Vs. Current i_q

6.4 FEA Characterization of the Machine

Finite Elements analysis, using Cedrat Flux2D V.10.1 software, was performed to verify the model derived in the previous section. Variation of d- and q-axes inductances with the stator current will be demonstrated as well as the presence of the cross-saturation induced inductance as the current is increased. A Surface Permanent Magnet Machine 260V, 8-pole, 6KVA, 2000 RPM will be considered. From the relevant figures we can approximate the cross-saturation inductance L_{dq}, L_d and L_q as following functions:

$$L_{dq} = -0.04 \cdot I_q \tag{6.31}$$

$$L_q = \begin{cases} 1.35, & 0 \leq i_q \leq 2 \\ 1.45 - 0.04375 \cdot i_q, & i_q > 2 \end{cases} \tag{6.32}$$

$$L_d = \begin{cases} 1.31, & 0 \le I_q \le 2 \\ 1.35 - 0.03751 \cdot i_q, & i_q > 2 \end{cases} \tag{6.33}$$

Figure 6.4a shows the variation of $q - axis$ inductance as a function of i_q. Figure 6.4b shows the variation of $d - axis$ inductance, $i_d = 0$ for both cases since we are examining SPM machine. Figures 6.4c and 6.3 show the variation of the mutual inductance L_{dq} and magnetic axis shift as functions of i_q. Figures 6.5 and 6.6 show the flux paths of the SPM machine, under no-load and 50% of full-load. The change in the flux path due to saturation is clear from the Figure 6.6.

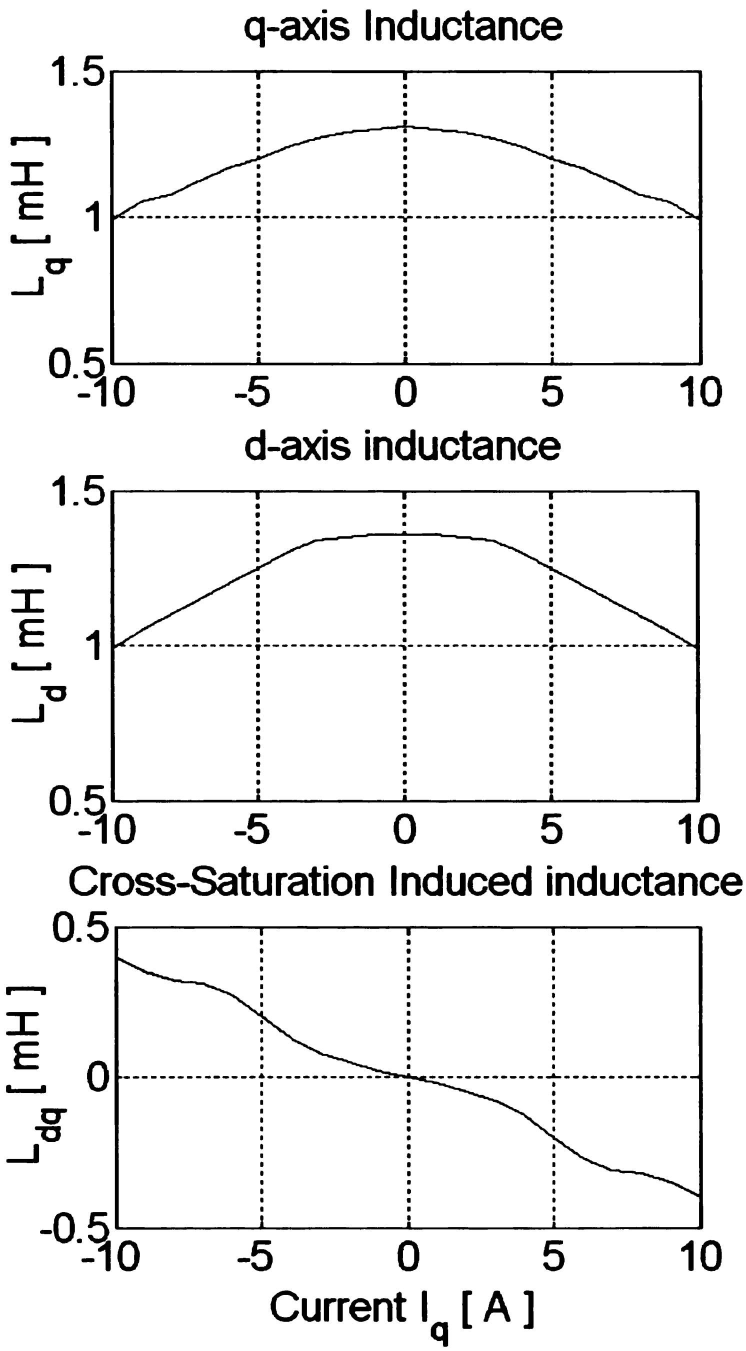

Figure 6.4: FEM Characterization of the Machine

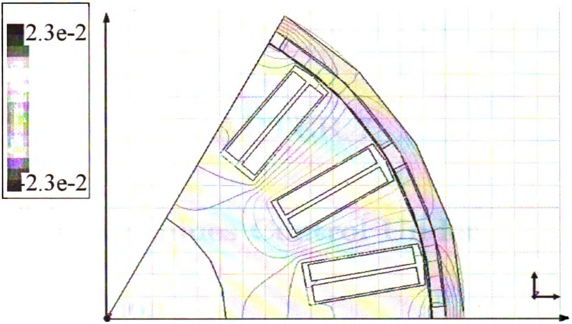

Figure 6.5: Flux Distribution of the SPM Machine under No-Load

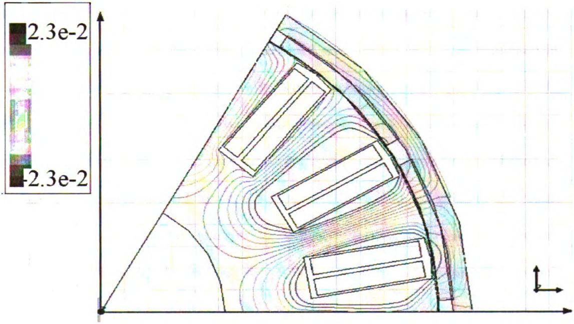

Figure 6.6: Flux Distribution of the SPM Machine under 50% of Full-Load

CHAPTER 7

SPM Machines Control Under Saturation

The non-linear model of SPM under saturation derived in Chapter 6 will be used here to design a new high-gain non-linear observer for position-sensorless control of PMAC machines. The new observer is then combined with control strategies presented in chapter 5 to implement a new controller which accounts for the operation of SPM machine under saturation. As it was shown in chapter 6 and in [14] the rotor position error increases as a function of the load current, however little has been published on techniques to correct for this error. Li *et al.* in [17] studied modeling of the cross-coupling magnetic saturation in a specific position-sensorless control scheme based on the high-frequency signal injection. Zhu *et al* in [18] proposed a practical approach for mitigating the rotor position error due to saturation in high-frequency injection method. However operation and flux position detection in SPM machines is affected by magnetic saturation regardless of the control strategy. Harnefors *et al.* in [19] studied a general algorithm for control of AC motors and noted the existence of the error in rotor position estimation due to saturation, but the analysis focused only on unsaturated case. Moreover error signal was linearized making their conclusions local only. It will be shown here that although this error may be relatively small, it has detrimental effect on the machine performance. In this work we will focus on operation of SPM machines under magnetic saturation. The major contributions of this part are nonlinear model and characterization of SPM machine and design, analysis and verification of a general algorithm for control of SPMAC machines under saturation. This chapter is divided into two major parts: in-depth analysis of the non-linear observer structure adjusted for presence of saturation without linearizing the error signal and experimental results validating the derived non-linear model of the machine, impact of saturation induced error on machine performance and validation of performance of the proposed observer combined with high frequency injection position-sensorless controller presented by Jang *et al.* in [22]. It is important to note that although the work presented here is focusing on the observer implementation in conjunction with high frequency injection method, it can be used in combination with any control strategy including back EMF methods or methods utilizing position encoder feedback.

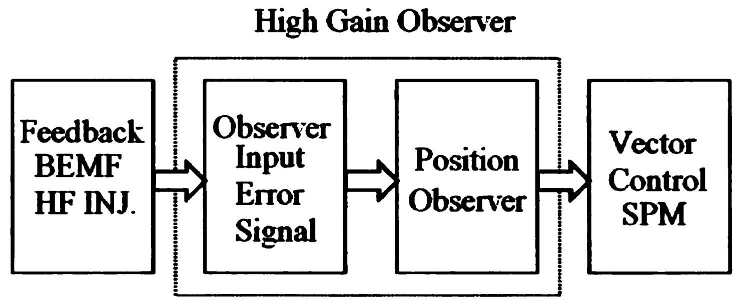

Figure 7.1: Block Diagram of the SPM Machine Controller

7.1 High-Gain Observer for Control of SPM Machines Under Saturation without Position Sensors

A general algorithm for speed and position estimation of AC drives was presented by Harnefors *et al.* [19], and although they noted the existence of position estimation error as a result of saturation, no details were given on mitigating techniques. The error signal was linearized making their conclusions local only. In this work we will examine the non-linear observer structure adjusted for presence of saturation presented in the previous section. We showed through analysis that the cross-saturation inductance is function of the offset angle θ_o so it is expected that the error signal will also be a function of the same variable, since the existence of the error is caused by the cross-saturation terms. We can see that the cross-saturation induced term will become 0 when $\tilde{\theta} = \theta_o$ at this point we know $\hat{\theta}$ and as $\hat{\theta}_o \to \theta_o$ we can determine both rotor position θ_r and rotor flux position θ.

With $\theta = \theta_r - \theta_o$ we can write the following error signal for non-salient PMAC machine:

$$\varepsilon = K\sin(m(\theta - \hat{\theta})) \tag{7.1}$$

where $\hat{\theta}$ is the estimated position of the rotor flux $(\hat{\theta}_r + \hat{\theta}_o)$ and K is the gain which will be defined later. $\varepsilon \to 0$ as $\hat{\theta}_o \to \theta_o$ and $\hat{\theta} \to$;. m is 1 for non-salient PM machine and 2 otherwise. This error signal can be used to drive speed and position estimates to their actual values by using the same non-linear high-gain observer topology as:

$$\dot{\hat{\omega}}_r = \gamma_2 \cdot \varepsilon \tag{7.2}$$

$$\dot{\hat{\theta}} = \hat{\omega}_r + \gamma_1 \cdot \varepsilon \tag{7.3}$$

where γ_1 and γ_2 are gains of the observer. We also define $\tilde{\omega}_r = \omega_r - \hat{\omega}_r$ and similarly $\tilde{\theta} = \theta - \hat{\theta}$, so we can write that the estimation errors satisfy the following conditions:

$$\dot{\tilde{\omega}}_r = -\gamma_2 \cdot K\sin(\theta - \hat{\theta}) \tag{7.4}$$

$$\dot{\tilde{\theta}} = \hat{\omega}_r - \gamma_1 \cdot K\sin(\theta - \hat{\theta}) \tag{7.5}$$

Note that $\gamma_1 > 0$, $\gamma_2 > 0$ and $k > 0$. As it was shown in chapter 6 with the non-linear model, the value of K may be uncertain and also may vary with the current i_q, so it is necessary to examine the stability of this topology as a function of K. Towards that end we make the following assumptions: since the speed change of the rotating machines has relatively slow dynamics we can assume that $\dot{\omega}_r = 0$. We will use Lyapunov function found under Popov criterion as described by Engel and Khalil

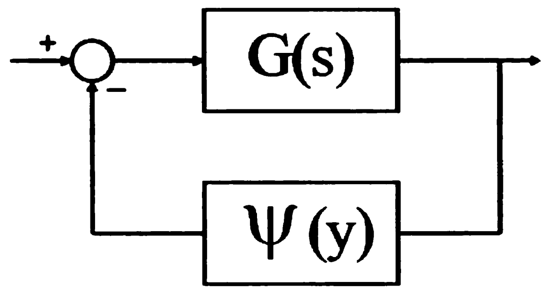

Figure 7.2: Popov Criterion Loop

in [21] to show the stability of the system.

The Popov criterion assumes that the system is divided into two parts in the feedback loop: the linear part $G(s)$ and the nonlinear one, $\psi(y)$ as shown in Figure 7.2. So we rewrite the system equations as:

$$\begin{bmatrix} \dot{\tilde{\theta}} \\ \dot{\tilde{\omega}}_r \end{bmatrix} = \begin{bmatrix} 0 & 1 \\ 0 & 0 \end{bmatrix} \begin{bmatrix} \tilde{\theta} \\ \tilde{\omega}_r \end{bmatrix} - \begin{bmatrix} \gamma_1 K \\ \gamma_2 K \end{bmatrix} u \tag{7.6}$$

where

$$u = \sin(y) \tag{7.7}$$

and for SPM we define:

$$y = \begin{bmatrix} 1 & 0 \end{bmatrix} \begin{bmatrix} \tilde{\theta} \\ \tilde{\omega}_r \end{bmatrix} \tag{7.8}$$

Obviously the system matrix $\begin{bmatrix} 0 & 1 \\ 0 & 0 \end{bmatrix}$ is not Hurwitz. We perform the loop transformation $u = -\alpha y + \psi(y)$ and obtain

$$\begin{bmatrix} \dot{\tilde{\theta}} \\ \dot{\tilde{\omega}}_r \end{bmatrix} = \begin{bmatrix} -\alpha\gamma_1 K & 1 \\ -\alpha\gamma_2 K & 0 \end{bmatrix} \begin{bmatrix} \tilde{\theta} \\ \tilde{\omega}_r \end{bmatrix} - \begin{bmatrix} \gamma_1 K \\ \gamma_2 K \end{bmatrix} \psi(y) \tag{7.9}$$

where

$$\psi(y) = \sin(y) - \alpha y. \tag{7.10}$$

The nonlinearity $\psi(y)$ is memoryless and the system matrix is Hurwitz for all $\alpha > 0$.

We define the observer gains for $0 < \rho << 1$ as

$$\gamma_1 = \frac{\alpha_1}{\rho K} \quad \gamma_2 = \frac{\alpha_2}{\rho^2 K} \tag{7.11}$$

noting that $0 < \alpha < 1$, so that $1 - \alpha > 0$. The scaled estimation errors are $\eta_1 = \tilde{\theta}$ and $\eta_2 = \rho\tilde{\omega}_r$, so the system becomes:

$$\rho\dot{\eta} = A\eta - B\psi(y) \tag{7.12}$$

where $\eta = \begin{bmatrix} \eta_1 & \eta_2 \end{bmatrix}^T$

$$y = C\eta \tag{7.13}$$

$$\psi(y) = \sin(y) - \alpha y. \tag{7.14}$$

$$A = \begin{bmatrix} -\alpha\alpha_1 K & 1 \\ -\alpha\alpha_2 K & 0 \end{bmatrix}, B = \begin{bmatrix} \alpha_1 \\ \alpha_2 \end{bmatrix}, C = \begin{bmatrix} 1 & 0 \end{bmatrix} \tag{7.15}$$

By Popov criterion the system (7.12) will be globally asymptotically stable for any nonlinearity $\psi(y)$ in the sector $[0, 1-\alpha]$ if the following condition is satisfied:

$$\frac{1}{1-\alpha} + Re[G(j\omega)] - \gamma\omega Im[G(j\omega)] > 0, \forall\omega \in [-\infty, \infty] \tag{7.16}$$

with the transfer function defined as

$$G(s) = C(sI - A)^{-1}B \tag{7.17}$$

or

$$G(s) = \frac{\alpha_1 s + \alpha_2}{s^2 + \alpha\alpha_1 s + \alpha\alpha_2} \tag{7.18}$$

Rewriting equation (7.16)

$$\frac{1}{1-\alpha} + \frac{\alpha\alpha_2^2 + \omega^2(\alpha\alpha_1^2 - \alpha_2) + \gamma\omega^4\alpha_1}{(\omega\alpha\alpha_1)^2 + (\alpha\alpha_2 - \omega^2)^2} > 0 \tag{7.19}$$

The condition will be satisfied if Kalman-Yakubovich-Popov lemma is satisfied as shown by Khalil (Lemma 6.3) in [20] and Engel [21], or for this particular case for $(\alpha\alpha_1)^2 > (\alpha\alpha_2)^2$ and $\gamma > 0$. The Lyapunov function for the system is given by:

$$V(\tilde{\omega}_r, \tilde{\theta}) = \frac{1}{2}\eta^T P\eta + \gamma\int_0^y \psi(\sigma)d\sigma \tag{7.20}$$

obviously positive definite making the derivative:

$$\begin{aligned} \dot{V}(\tilde{\omega}_r, \tilde{\theta}) &= \frac{1}{2\rho}\left[\zeta\eta^T P\eta - (L\eta + wu)^T(L\eta + wu)\right] \\ & -\frac{1}{\rho}\psi(y)^T\left[y - \frac{1}{1-\alpha}\psi(y)\right] \end{aligned} \tag{7.21}$$

Hence,

$$\dot{V}(\tilde{\omega}_r, \tilde{\theta}) \leq -\frac{1}{2\rho}\zeta\eta^T P\eta \tag{7.22}$$

negative definite for $\dot{\omega} = 0$.

7.2 Observer Gains and Tracking

Over a short period of time the rotor position change can be reasonably approximated with a ramp function so $\dot{\omega}_r$ is constant or $\dot{\omega}_r = \kappa$, so that κ will be added to the right side of (7.4). Setting $\dot{\tilde{\omega}}_r = \dot{\tilde{\theta}} = 0$, we can solve for asymptotic ramp tracking errors with γ_1 and γ_2 defined in (7.11) we re-write (7.4) as:

$$\tilde{\omega}_r = \kappa - \gamma_2 \cdot K\sin(\tilde{\theta}) \tag{7.23}$$

Hence errors are:

$$\theta^{error} = \sin^{-1}\left(\frac{\kappa\rho}{\alpha_2}\right) \tag{7.24}$$

$$\omega_r^{error} = \kappa\frac{\alpha_1}{\alpha_2} \tag{7.25}$$

These expressions are useful because they allow us to the analyze tracking error of the observers in terms of observer gains and known drive parameters i.e. speed loop bandwidth and maximum acceleration.

7.3 Eliminating 180^o Ambiguity at Startup [24]

The rotor position angle, θ_r, is defined as the angle between the stationary frame q-axis and the rotor frame q-axis. The estimation methods described above determine θ_r based on the inductance difference between the d and q-axes. The methods do not inherently differentiate between the positive q-axis and the negative q-axis. This is apparent from the current and inductance equations which are proportional to the twice the rotor angle. This means that a rotor position angle of 0 electrical degrees will result in the same negative sequence current as a rotor position angle of 180^o. If the rotor position is at 0 degrees and the self-sensing estimate locks onto 180^o, the result will be that the machine will spin in the negative direction for a positive speed command. So an initiation test must be performed at start up to determine whether the self-sensing estimate has locked onto the correct angle [24].

The influence of the stator current on the flux-parallel saturation level in the machine is utilized. For this purpose, after having detected the flux axis (but not knowing the sign of the flux yet) as described above, a flux-parallel stator current component (produces no torque) is applied. Now, a measurement is carried out. This procedure is repeated with the opposite sign of the stator current. Again, a measurement is performed. Comparing the magnitudes of the current changes during the measurements shows which case was the flux-increasing (larger current change per time in flux direction) or flux-decreasing (smaller current change per time since saturation is reduced). Hence, the flux is fully detected now [24].

The initiation test is done as follows. First the rotor is moved to a known position. This is done by commanding a small dc voltage onto the stator winding which effectively sets up a dc magnetic field in the air gap. The rotor magnets will align with this field and thus the rotor will move to a known position. By commanding a small additional duty cycle to the positive rail switch on phase A of the machine, a dc field is established in the direction of the stator +q-axis. The rotor magnets align with this field which results in a 90^o angle between the stator q-axis and the rotor q-axis (ie. $\theta_r = 90^o$). The self-sensing algorithm will estimate either θ_r=90^oor θ_r=-90^o for the rotor in this position. If the estimate is equal to -90^o , then 180^o is added to the self-sensing estimate and that result is used in the control algorithm for θ_r. If the estimate is equal to 90^o, then there is no offset angle added to the estimate before being used in the control algorithm [24].

7.4 Controller for SPM Machine

7.4.1 High-Frequency Injection Methods

In this section we will revisit the control strategies described in chapter 5 and use the theory presented in chapter 6 and previous section of this chapter to derive a particular controller for SPM Machine. High-frequency Injection scheme will be considered to derive the error signal. Estimation of the rotor position employing alternating voltage space vector injection is described. Consider the previously derived equation (5.6), from chapter 5, in the actual rotor frame of reference. The high frequency pulsating voltage space vector is injected in the estimated (denoted by $\hat{r}$) d-axis direction.

$$\begin{bmatrix} v^{\hat{r}}_{dhf} \\ v^{\hat{r}}_{qhf} \end{bmatrix} = V_{inj} \begin{bmatrix} \cos(\omega_c t) \\ 0 \end{bmatrix}. \tag{7.26}$$

Performing the same transformation to the estimated frame of reference as described chapter 5I and governed by equation(5.10)- (5.18) and error definition as in (6.30) and then measuring the induced current in $q-axis$. The current in (5.25) can be written as follows:

$$i^r_{qshf} = -\frac{1}{2}\frac{(r_{diff} + j\omega_h L_{diff})V_{inj}\sin(\tilde{\theta}_r - \theta_o)}{(r^r_{dhf} + j\omega_h L^r_{dhf})(r^r_{qhf} + j\omega_h L^r_{qhf})}\cos(\omega_{hf} t) \tag{7.27}$$

In the high-frequency impedances the inductances are dominant and sufficiently larger than the resistances, so we can neglect the resistances. Hence the current becomes:

$$i^r_{qshf} = \frac{v_{inj}}{2}\left[-\frac{\omega_{hf} L_{diff}\sin(\omega_{hf} t)}{\omega^2_{hf} L^r_{dhf} L^r_{qhf}}\right]\sin(\tilde{\theta}_r - \theta_o) \tag{7.28}$$

The rotor position estimation error can be obtained if this signal is passed through an LPF with appropriate corner frequency:

$$f(\tilde{\theta}_r) = LPF\left[-i^r_{qshf}\sin(\omega_{hf} t)\right] \tag{7.29}$$

Finally q-axis current containing rotor position error is derived:

$$i_{qshf}^{r} = -\frac{V_{inj} L_{diff}}{4\omega_{hf} L_{dhf}^{r} L_{qhf}^{r}} \sin(\tilde{\theta}_r - \theta_o) \tag{7.30}$$

Now that we have an error signal similar to that defined by (7.1) we can write our observer for this machine. Hence,

$$K = -\frac{V_{inj} L_{diff}}{4\omega_{hf} L_{dhf}^{r} L_{qhf}^{r}} \tag{7.31}$$

so we define

$$\gamma_1 = \frac{-8\omega_{hf} L_{dhf}^{r} L_{qhf}^{r}}{\rho V_{inj} L_{diff}}, \gamma_2 = \frac{-4\omega_{hf} L_{dhf}^{r} L_{qhf}^{r}}{\rho^2 V_{inj} L_{diff}} \tag{7.32}$$

substituting into equations (7.2) and (7.3) the observer will take the following format:

$$\begin{bmatrix} \dot{\hat{\theta}} \\ \dot{\hat{\omega}}_r \end{bmatrix} = \begin{bmatrix} 0 & 1 \\ 0 & 0 \end{bmatrix} \begin{bmatrix} \hat{\theta} \\ \hat{\omega}_r \end{bmatrix} - \begin{bmatrix} 2/\rho \\ 1/\rho^2 \end{bmatrix} \frac{\varepsilon}{K} \tag{7.33}$$

In next section we will show the implementation of the same observer in the controller based on back EMF measurement.

7.4.2 Control Based on Back EMF Measurement

In this section we will use the theory presented to derive a particular controller for SPM Machine. Back EMF position-sensorless scheme will be considered to derive the error signal. Consider the previously derived equation (5.18) in the actual rotor frame of reference ignoring the current derivatives in steady state:

$$\begin{bmatrix} v_q^r \\ v_d^r \end{bmatrix} = \begin{bmatrix} R_s + \omega_r L_{12} & \omega_r L_{22} \\ -\omega_r L_{11} & R_s - \omega_r L_{21} \end{bmatrix} \begin{bmatrix} i_q^r \\ i_d^r \end{bmatrix} + \begin{bmatrix} \omega_r \psi_q^r \\ 0 \end{bmatrix} \tag{7.34}$$

Transferring the same equation in estimated frame of reference d-axis back EMF term will take the following for:

$$E_d = \omega_r \psi_m \sin(\tilde{\theta}_r - \theta_o) \tag{7.35}$$

where E_d for practical implementation will obtained as follows:

$$\hat{E}_d = v_d^{\hat{r}} - R_s i_d^{\hat{r}} + \omega_r (L_{11} i_q^{\hat{r}} + L_{12} i_d^{\hat{r}}) \tag{7.36}$$

Now that we have an error signal similar to that defined by (7.1) we can write our observer for this machine. Hence,

$$K = -\hat{\omega}_r \psi_m \tag{7.37}$$

so we define

$$\gamma_1 = \frac{2}{\rho} \frac{-1}{\hat{\omega}_r \psi_m}, \gamma_2 = \frac{1}{\rho^2} \frac{-1}{\hat{\omega}_r \psi_m} \tag{7.38}$$

substituting into equations (7.2) and (7.3) the observer will take the following format:

$$\begin{bmatrix} \dot{\hat{\theta}} \\ \dot{\hat{\omega}}_r \end{bmatrix} = \begin{bmatrix} 0 & 1 \\ 0 & 0 \end{bmatrix} \begin{bmatrix} \hat{\theta} \\ \hat{\omega}_r \end{bmatrix} - \begin{bmatrix} 2/\rho \\ 1/\rho^2 \end{bmatrix} \frac{\varepsilon}{K} \tag{7.39}$$

It is worth noting that this is only one possible way of generating the error signal. A similar error signal could be generated by employing high-frequency injection method for sensorless control or even utilizing position encoder.

7.5 Experimental Results

In this section we present simulation and experimental results of the proposed control algorithm. First experimental characterization of the machine is carried out to obtain the inductances under saturated conditions. Figure. 7.3 shows measured SPM machine inductances. The measured inductances are somewhat higher than the values obtained via FE analysis, however this should not have any effect on the control algorithm since the ratio of d- and q- axes inductances remains unchanged.With the machine model in place we now turn to experimental validation of the control algorithm. The block diagram of the control system is shown in Figure. 7.4.

The first set of experimental results shows decreased performance of the system if the magnetic axis shift is not taken into account by comparing the transient performance of the systems with and without compensation for the saturation induced error. In the compensated system setup angle shift is simply added to the rotor position measurement from the encoder. A step speed command is applied to both setups with q-axis current limit set at 10A, while constant torque is provided on the shaft by the coupled Induction Machine acting as a load, we measured the actual speed and observed the time needed to accelerate to the reference speed, which in turns provides the information about developed torque in the machine. Figure. 7.5 shows the difference in performance at rated current, while the Table 7.1 shows performance

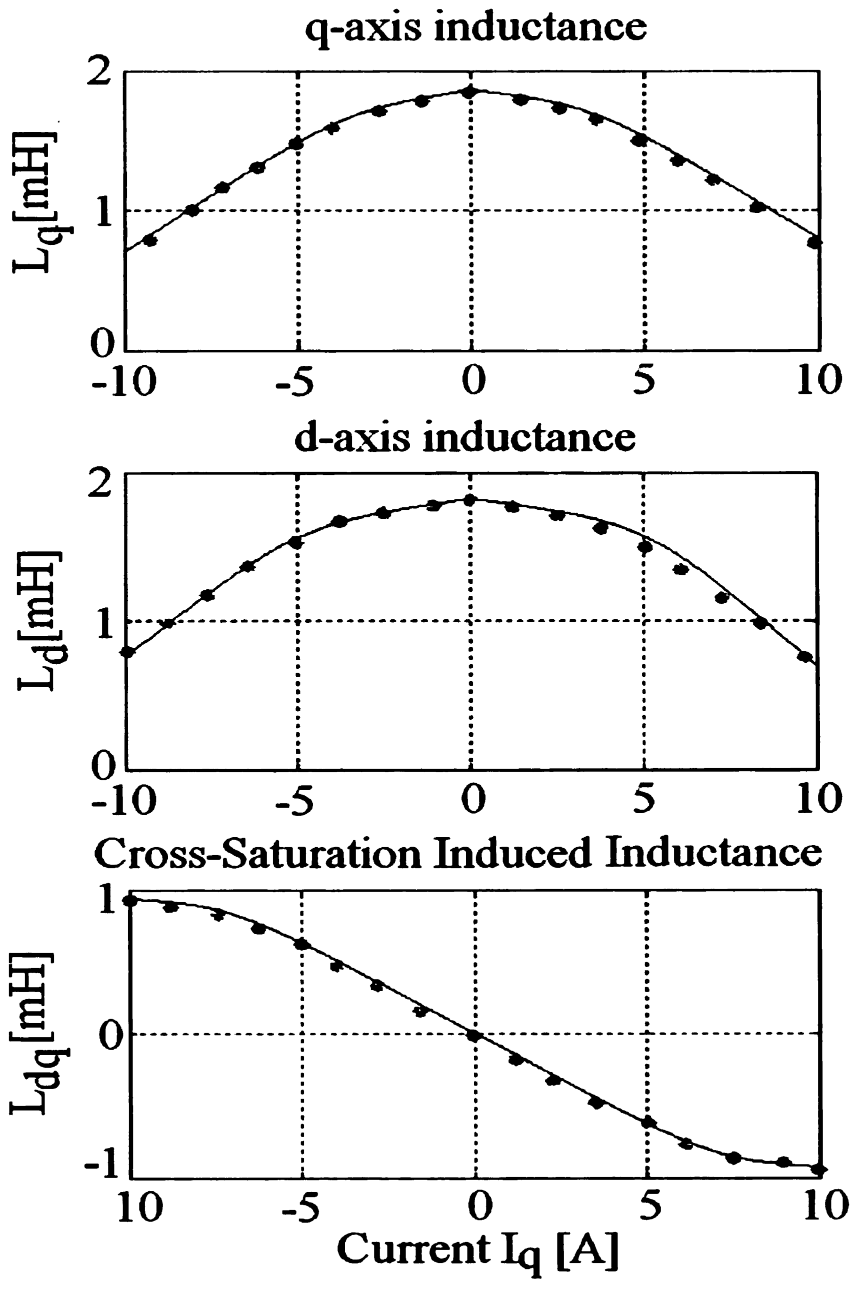

Figure 7.3: Experimental Measurement of Inducatances

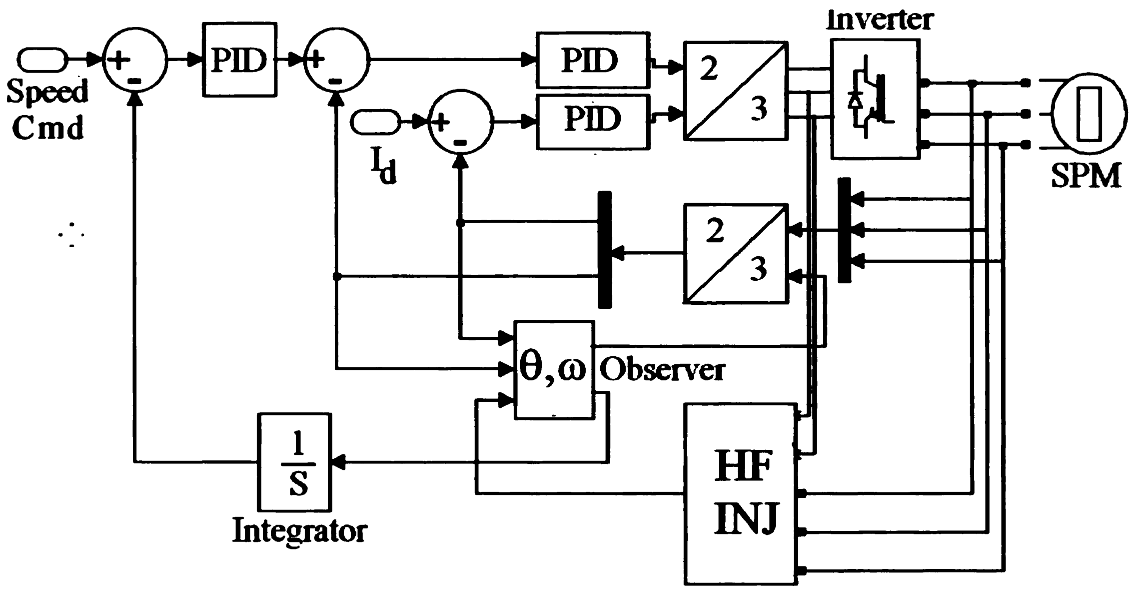

Figure 7.4: Block Diagram of the High-Frequency Injection Control Algorithm

q-axis Axis Current	% Torque Increase
2 A	1.4 %
4 A	4.8 %
6 A	6.7 %
8 A	11.8 %
10 A	11.9 %

Table 7.1: Experimental Results

comparison for the range q-axis current.

The second set of experimental results shows the comparison between rotor position obtained from the encoder feedback corrected by the saturation induced error, and rotor position obtained from our observer for a given speed reference profile and fixed shaft torque. Figure. 7.6 shows that very good agreement is achieved with minimal error.

Finally Fig. 7.7 shows the comparison of the performance of the systems with

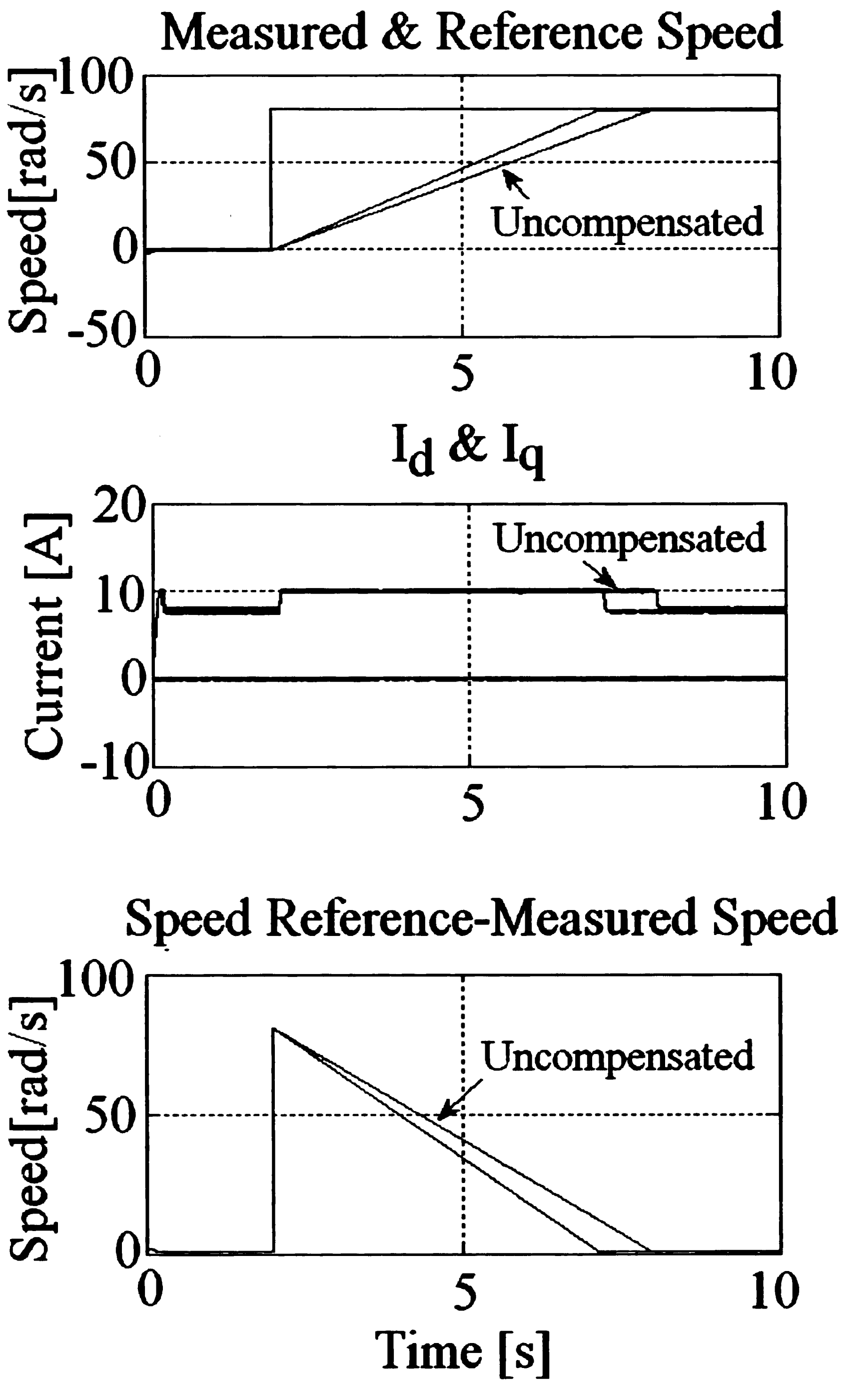

Figure 7.5: Performance Comparison at Rated Current $I_q = 8A$

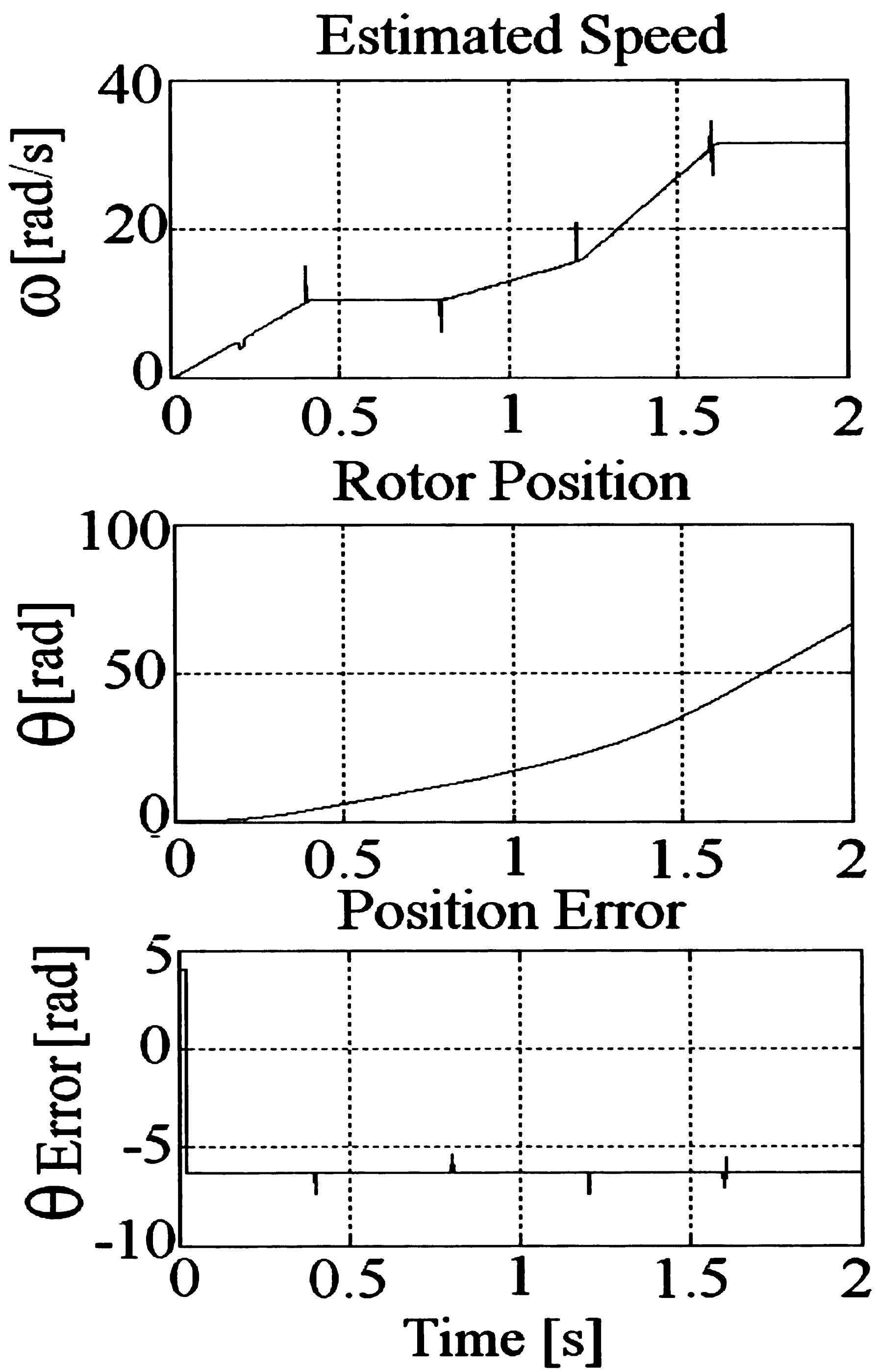

Figure 7.6: Observer Performance Comparison at No-Load Current

rotor position feedback from the encoder and the one with the feedback from the observer for a given speed command profile and constant shaft torque. It is clear that higher q-axis current (around 10% in this case) is required to achieve the same speed and torque if the magnetic axis shift error is not taken into consideration. In other words, by accounting for the magnetic axis shift a performance of the machine can be improved. This translates into higher efficiency for the given torque requirement and higher maximum torque capability.

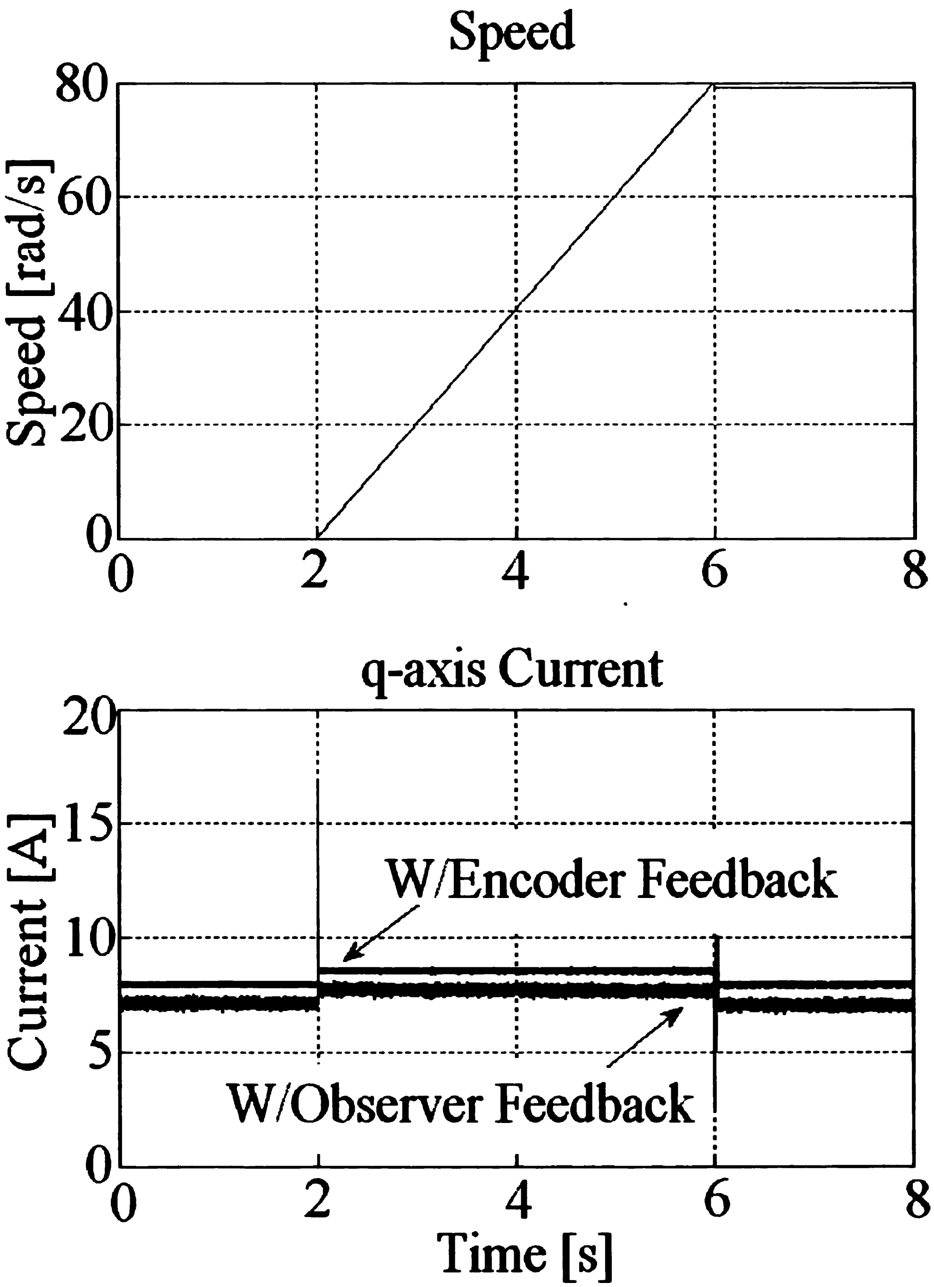

Figure 7.7: Observer Performance Comparison at Rated Current $I_q = 8A$

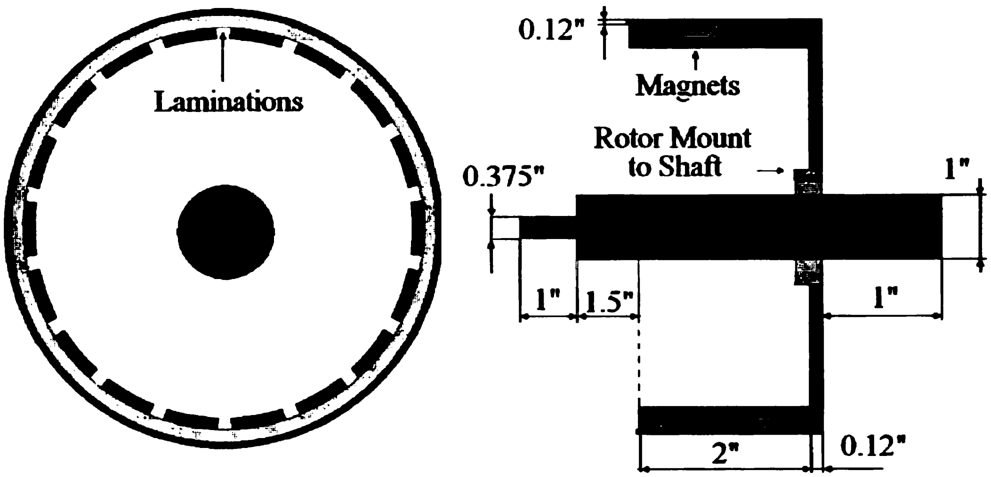

Figure 7.8: Outer Rotor PMAC Machine

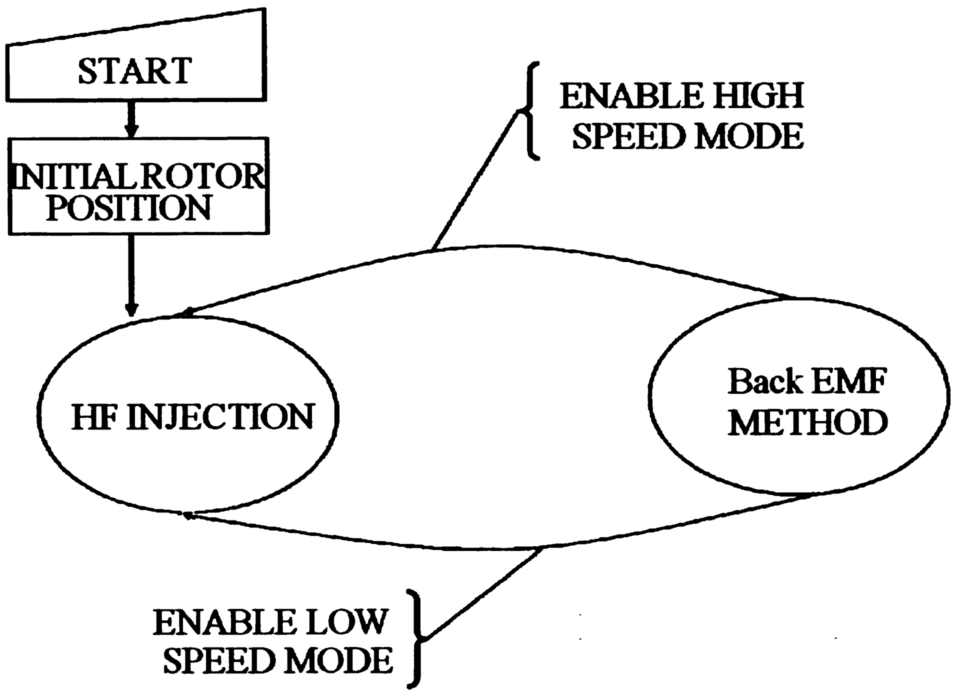

Figure 7.9: State Diagram of the Controller for Entire Speed Range

CHAPTER 8

Conclusion

The first part of this work presented design, analysis and comparison of the best PMAC machine candidate for integrated starter-generator application in Series HE bus. Performance capabilities such as maximum torque, power density, size and weight of IPM and SPM machines were addressed and evaluated. Finite element simulation results are provided to support the analytical work. The best machine candidate (SPM with 1/2 slot/pole/phase) was proposed and the prototype built for experimental validation of the results presented here.

The second part of the work deals with operation and control of SPM machines. Both control strategies utilizing position resolvers and position-sensorless are considered with the effect of saturation on both of them. A non-linear model of the PMAC machine was presented to show the influence of saturation. It was shown both analytically and in FEM simulation that the SPMSM machine under saturation will exhibit magnetic axis shift which causes an error in flux position detection and can have further ramifications such as: demagnetization of permanent magnet, poor performance of the machine etc. Finally, a new high-gain observer is designed in combination with high-frequency injection methods to account for the entire operating range of the machine, including the saturation. To verify the performance and effectiveness of the designed observer, an existing position-sensorless control strategies utilizing high-freaqency injection (for startup and low speeds) and Back EMF method (for high speed operation) are implemented in combination with the designed observer. Finally simulation and experimental results of the machine performance with the proposed observer are presented. The contributions of this work can be summarized as follows:

1. Comprehensive analysis and comparison of Interior Permanent Magnet Machines vs. Surface Permanent Magnet Machines for ISG Application.

2. Analysis and comparison of distributed vs. concentrated windings, as well as the analysis of various Slot/Pole/Phase combinations (including 1/2 SPP topology) with respect to machine size, minimal losses and highest torque capability.

3. Tools for analytical design and performance assessment of SPM Machines with concentrated windings are derived and discussed. In particular improved models for core and magnet losses of fractional slot SPM machines are derived.

4. Nonlinear model and characterization of SPM Machine under saturation.

5. Design, analysis and verification of a general algorithm for control of SPM machines under saturation.

BIBLIOGRAPHY

[1] J. M. Miller, "Propulsion Systems for hybrid Vehicles" *IEE London*, UK 2004.

[2] Cai, W. "Comparison and review of electric machines for integrated starter alternator applications" : *IEEE Industry Applications Conference, Annual Meeting,* Oct. 2004 Vol. 1, pp. 393.

[3] L. Friedrich, L. Chedot. G. Biedinger, J.-M. Macret, P. " Integrated Starter Generator: The Need for an Optimal Design and Control Approach. Application to a Permanent Magnet Machine" *IEEE Transactions on Industry Applications,* March 2007, Vol. 43, Issue: 2 pp. 551-559.

[4] Nagorny, A.S.; Dravid, N.V.; Jansen, R.H.; Kenny, B.H "Design aspects of a high speed permanent magnet synchronous motor / generator for flywheel applications" *IEEE International Conference on Electric Machines and Drives,* 15-18 May 2005, pp. 635 - 641.

[5] Salminen, P., Pyrhönen, J., Niemelä, M., 2003. A comparison between surface magnets and embedded magnets in fractional slot wound PM motors. *International Symposium on Electromagnetic Fields in Electrical Engineering*, September 2003. Maribor, Slovenia, Vol. 1, pp. 131.

[6] J. Cross and P. Viarouge, "Synthesis of High Performance PM Motors With Concentrated Windings," *IEEE Transaction on Energy Conversion*, June 2002. Vol. 17, pp. 248-253.

[7] J. Cross and P. Viarouge, "Synthesis of High Performance PM Motors With Concentrated Windings," *IEEE Transaction on Energy Conversion*, June 2002. Vol. 17, pp. 248-253.

[8] D. Ishak, Z. Q. Zhu, and D. Howe, "Comparative Study of Permanent Magnet Brushless Motors with All Teeth and Alternative Teeth Windings," *IEE International Conference on Power Electronics, Machines and Drives,* April 2004, Vol. 2, pp. 834-839.

[9] D. Ishak, Z. Q. Zhu, and D. Howe, "Analytical Prediction of Rotor Eddy Current Losses in Permanent Magnet Brushless Machines with All Teeth and Alternate Teeth Windings Part I: Polar Co-ordinate Model," *IEEE International Conference on Electrical Machines and Systems*, November 2004, Korea.

[10] D. Ishak, Z. Q. Zhu, and D. Howe, "Analytical Prediction of Rotor Eddy Current Losses in Permanent Magnet Brushless Machines with All Teeth and Alternate Teeth Windings Part II: Rectangular Co-ordinate Model," *IEEE International Conference on Electrical Machines and Systems*, November 2004, Korea.

[11] J. Wang, Z. P. Xia, and D. Howe, "Analysis of Three-Phase Surface-Mounted Magnet Modular Permanent Magnet Machines," *IEE International Conference on Power Electronics, Machines and Drives,* April 2004, Vol. 3.

[12] F. Libert and J. Soulard, "Investigation on Pole-Slot Combinations for Permanent-Magnet Machines with Concentrated Windings," *IEEE International Conference on Electrical Machines*, September 2004, Poland.

[13] A.M. El-Refaie, "High Speed Operation of Permanent Magnet Machines" *Ph.D Dissertation*, University of Winsconsin Madison, 2005

[14] M. J. Corley and R. D. Lorenz, "Rotor position and velocity estimation for a salient-pole permanent magnet synchronous machine at standstill and high speed," *IEEE Transaction on Industry. Applications*, Jul.–Aug. 1998, Vol. 34, pp. 784–789.

[15] P. Guglielmi, M. Pastorelli, and A. Vagati, "Cross saturation effects in IPM motors and related impact on zero-speed sensorless control", *IEEE Industry Applications Society Annual Meeting*, October 2005, Vol. 4, pp. 2546–2552.

[16] B. Stumberger, G. Stumberger, D. Dolinar, A. Hamler, and M. Trlep, "Envaluation of saturation and cross-magnetization effects in interior permanent-magnet synchronous motor,", *IEEE Transaction on Industry Application*, October 2003, Vol.39, pp. 1264–1271.

[17] Y. Li, Z.Q. Zhu, D. Howe, C.M. Bingham, "Modeling of Cross-Coupling Magnetic Saturation in Signal-Injection-Based Sensorless Control of Permanent-Magnet Brushless AC Motors," *IEEE Transactions on Magnetics*, June 2007 Vol.43, pp.2552-2554.

[18] Z.Q. Zhu, Y. Li, D. Howe, C.M. Bingham, "Compensation for Rotor Position Estimation Error due to Cross-Coupling Magnetic Saturation in Signal-Injection-Based Sensorless Control of Permanent-Magnet Brushless AC Motors," *IEEE International Conference on Electric Machines and Drives*, May 2007, pp. 635 - 641.

[19] L. Harnefors, H.N. Nee, "A General Algorithm for Speed and Position Estimation of AC Motors," *IEEE Transactions on Industrial Electronics*, February 2000, Vol.47, pp.77-79.

[20] H. K. Khalil, "Nonlinear Systems" , *Prentice Hall*, 2002 Upper Saddle River, New Jersey, 3rd edition.

[21] J. Engel, "Speed and Position estimation in AC Motors Using High-Gain Observers", *Status Report*, 2006, Michigan State University, East Lansing,

[22] J. H. Jang, S. K. Sul, J. I. Ha, K. Ide, and M. Sawamura, "Sensorless drive of surface-mounted permanent-magnet motor by high-frequency signal injection based on magnetic saliency," *IEEE Transaction on Industry Applications*, August 2003, Vol. 39, pp. 1031-1039.

[23] C. Wang and L. Xu, "A novel approach of rotor position detection for machines based on conventional PWM algorithms", *IEEE National Aerospace Electronics Conference*, October 2000, Dayton, OH.

[24] ,M. Schrodl, "Sensorless Control of AC Machines", *Habilitationsschrift*, 1992 Dusseldorf: VDI-Verlog, VDI-Fortschrittsberichte Nr. 117, Reihe 21.

[25] Z. Q. Zhu, D. Howe, E. Bolte, and B. Ackermann, "Instantaneous Magnetic Field Distribution in Brushless Permanent Magnet dc Motors, Part I: Open-Circuit Field," *IEEE Transaction on. Magnetics*, January 1993, Vol. 29, pp.124-135.

[26] Chuanyang Wang, Longya Xu, "A Novel Approach for Sensorless Control of PM Machines Down to Zero Speed Without Signal Injection or Special PWM Technique" *IEEE Transaction on Power Electronics*, November 2004. Vol. 19 No 6.

[27] J. Cros, P. Viarouge, and A. Halila, "Brush DC Motors with Concentrated Windings and Soft Magnetic Composites," *IEEE Industry Applications Society Annual Meeting,* October 2001, Vol. 4, pp. 2549-2556.

[28] C. Wang and L. Xu, "A novel approach of rotor position detection for machines based on conventional PWM algorithms," in Proc. IEEE Nat. Aerospace Electronics Conf., Dayton, OH, 10–12, 2000, pp. 547–553.

[29] K. Atallah, D. Howe, P. H. Mellor, and D. A. Stone, "Rotor Loss in Permanent-Magnet Brushless AC Machines," *IEEE Transaction on Industry Applications*, December 2000, Vol. 36, pp. 1612-1618.

[30] C. Mi, G. R. Slemon, and R. Bonert, "Modeling of Iron Losses of Permanent-Magnet Synchronous Motors," *IEEE Transaction on Industry Applications*, June 2003, Vol. 39, pp. 734-742.

[31] M. J. Corley and R. D. Lorenz, "Rotor position and velocity estimation for a salient-pole permanent magnet synchronous machine at standstill and high speeds," *IEEE Transaction on Industry Applications*, August 1998, Vol. 34, pp. 784–789.

[32] L. A. S. Ribeiro et al., "Comparision of carrier signal voltage and current injection for the estimation of flux angle and rotor position," I*EEE Industry Applications Society Annual Meeting,* St. Louis, MO, October 1999, pp. 452–459.

[33] S. Ogasawara and H. Akagi, "Implementation and position control performance of a position-sensorless IPM motor drive system based on magnetic saliency," *IEEE Transaction on Industry Applications*, Sugust 1998, Vol. 34, pp. 806–812.

[34] P.L. Jansen, and R.D. Lorenz, "Transducerless position and velocity estimation in induction and salient AC machines", *IEEE Transaction on Industry Electronics*, April 1995, Vol. 31, pp. 240-247.

[35] S. Kondo, A. Takahashi, and T. Nishida, "Armature Current Locusbased Estimation Method of Rotor Position of Permanent Magnet Synchronous Motor without Mechanical Sensor", *IEEE Proceedings of Industry Applications Society Annual Meeting,* 1995, pp. 55-60.

[36] Jahns, T. M., Kliman, G. B., and Neumann, T. W. "Interior permanent-magnet synchronous motors for adjustable-speed drives" *IEEE Transaction on Industry Applications,* 1986, pp. 738–747.

[37] S. Ogasawara and H. Akagi, "An approach to position sensorless drive for brushless dc motors," *IEEE Transaction on Industry Applications,* Septeber 1991, Vol. 27, pp. 928–933.

[38] N. Ertugrul and P. Acarnley, "A new algorithm for sensorless operation of permanent magnet motors," *EEE Transaction on Industry Applications*, February 1994, Vol. 39, pp. 126–133.

[39] J.-I. Ha, K. Ide, T. Sawa, S. Sul, "Sensorless position control and initial position estimation of an interior permanent magnet motor",*IEEE Proceedings of Industry Applications Society Annual Meeting*, September 2001, Chicago, IL, pp. 2607-2613.

[40] Thorsten Frezke, "Impacts of Cross-Saturation on Sensorless Control of Surface Permanent Magnet Synchronous Motors" *European Conference on Power Electronics and Applications*, Sept. 2005.

[41] Ji-Hoon Jang et al., " Analysis of Permanent Magnet Machine for Sensorless Control based on High Freuqency Signal Injection" *IEEE Transaction on Industry Applications,* September 2004, Vol. 6, pp. 1595-1604.

[42] Gieras J. F. " Permanent Magnet Motor Technology" *Dekker Publishing*, New York, 2002.

[43] D. Ishak, Z. Q. Zhu, and D. Howe, "Permanent Magnet Brushless Machines with Unequal Tooth Widths and Similar Slot and Pole Numbers," I*EEE Industry Applications Society Annual Meeting,* October 2004, Vol. 2, pp. 1055-1061.

[44] Aldo Boglietti, "Predicting Iron Losses in Soft Magnetic Materials With Arbitrary Voltage Supply: An Engineering Approach, IEEE Transaction On Magnetics, March 2003, Vol. 39, pp. 981-989.

[45] T. A. Lipo, " Anaysis of Synchronous Machines - ECE 511 Course Notes" *ECE 511 Course Notes, WEMPEC,* Madison, Wisconsin 2003

[46] J. R. Hendershot and T. J. Miller, "Design of Brushless Permanent-Magnet Motors" *Magna Physics Publishing and Calderon Press Oxford,* 1994.

[47] R. Krishnan, "Electric Motor Drives: Modeling, Analysis, and Control", *Prentice Hall,* 2001.

[48] D. Zarko,"A Systematic Approach to Optimized Design of Permanent Magnet Motors with Reduced Torque Pulsations" PhD. Dissertation - University of Wisconsin, Madison, 2004

[49] A. Boglietti, A. Cavagnino, T. L. Mthombeni, and P. Pillay, Comparison of lamination iron losses supplied by PWM voltage:US and European experiences IEEE International Conference on Electrical Machines and Drives, May 2005.